Chemical Investigations of Nanomaterials

A Thesis

submitted in partial fulfillment of the

requirements of the degree of

Master of Science [Engg.]

by

Leela Srinivas Panchakarla

Chemistry and Physics of Materials Unit
Jawaharlal Nehru Centre for Advanced Scientific Research
(A Deemed University)
Bangalore – 560 064
December 2007

Chemical Investigations of Nanomaterials

A Thesis
submitted in partial fulfillment of the
requirements of the degree of
Master of Science [Engg.]
by
Leela Srinivas Panchakarla

Chemistry and Physics of Materials Unit
Jawaharlal Nehru Centre for Advanced Scientific Research
(A Deemed University)
Bangalore – 560 064
December 2007

Dedicated

To

My Parents

DECLARATION

I hereby declare that the matter embodied in this thesis entitled **"Chemical Investigations of Nanomaterials"** is the result of investigations carried out by me under the supervision of Prof. C. N. R. Rao, FRS at the Chemistry and Physics of Materials Unit, Jawaharlal Nehru Centre for Advanced Scientific Research, Bangalore, India and that it has not been submitted elsewhere for the award of any degree or diploma.

In keeping with the general practice in reporting scientific observations, due acknowledgement has been made whenever the work described is based on the findings of other investigators.

P. Leela Srini

Leela Srinivas Panchakarla

CERTIFICATE

I hereby certify that the matter embodied in this thesis entitled "**Chemical Investigations of Nanomaterials**" has been carried out by Mr. Leela Srinivas Panchakarla, at the Chemistry and Physics of Materials Unit, Jawaharlal Nehru Centre for Advanced Scientific Research, Bangalore, India under my supervision and that it has not been submitted elsewhere for the award of any degree or diploma.

Prof. C. N. R. Rao, FRS

(Research Supervisor)

Acknowledgements

I am extremely grateful to Prof. C. N. R. Rao, FRS for suggesting me research problems and guiding me throughout. He has been a constant source of inspiration for me. I greatly admire his enthusiasm towards science. I express my hearty gratitude to him for giving me an opportunity to work under his guidance.

I would like to express my sincere thanks to Dr. A. Govindaraj who has helped me a great deal in carrying out the various experiments. It has been a good learning experience working with him in the lab.

I am thankful to Basavaraj, Usha Madam, Anil, Vasu and Selvi, amit (IISC) for their help with the various characterization techniques.

I am thankful to Dr. A. Sundaresan for magnetic measurement facility and Prof. G. U. Kulkarni for XPS and STM facilities.

I am thankful to INI center and Convenor of the center Prof. K. Chattopadhyay, IISC for TEM facility.

I thank Bhat, Gomathi and Neenu for their help with the Raman measurements, Neena for her help with the STM measurements, Bhuvana for her help with the XPS measurements, Vengadesh, Pranab and Madhu for their help with the magnetic measurements and Srinivasraju for his help in FORTRAN calculations.

I would like to thank my lab members Vivek, Chandu, Kalyani, Bhat, Gomathi, Rakesh, subrahmanyam, Neenu, Kanishka, Sandeep and Basanth for their help and co-operation.

I am thankful to the faculty members of JNC and IISc for their courses. In particular, I would like to thank Prof. G. U. Kulkarni, Prof. Swapan Pati, Prof. Umesh V Waghmare, Prof. Chandrabhas Narayana, Prof. K. S. Narayan, Dr. M. Eswaramoorthy, and Dr. A. Sundaresan from JNC and Prof. S. Ranganathan from IISc.

I am thankful to Ravi, Nishaj, Dharma, Shithal, Satish, and Vikas of computer lab for their help.

I would like to thank Mrs. Rao for her encouraging words and hospitality.

I am thankful to all academic staff members (Mrs. Sukanya, Dr. Princy).

I am thankful to office members (Mrs. Sashi, Gowda, Victor and Mrs. Sudha).

I am thankful to all work shop members (Arogyanathan, moorthy and sunil).

I would like to thank Mr. M. M. V. Y. Swamy, lecturer, who has been giving constant encouragement and suggestions in my life.

I would like to thank KKR, Kalyani, Rakesh, Neenu, Gomathi, Sandeep and Dr. A. Govindaraj for their help in writing thesis.

I would like to thank all HCU faculty, classmates and friends.

Special thanks to my friends Anji, Uday, Phani, Rakesh, Lakshmi, Mouli, Kiran, Pavan, majhi, ramesh, KKR, manu, Vivek, Chandu, Kalyani, Bhat, Gomathi, subrahmanyam, Neenu, Kanishka, Sandeep, Basanth, Pearl, Reji, Dinesh, Saiki, kalyan, Vijay, Claudy, Minaxie, Thiru, Sahu, Raju, Guru, Shipra, Madhu, Venky, Pranab, Srinivasraj, Anil, Malik, and all sports members of JNC and my home town.

Heartfelt thanks to my parents, brother and sister for being there for me always.

Preface

"Nano"-science and technology boom, *the fourth industrial revolution*, has aroused new excitement in scientists all over the world. Nanomaterials are thought to play an important role in everyday life of human beings because of their potential applications in diverse fields. A great deal of research is being focused on synthesis and properties of nanomaterials in order to understand them better.

Chapter 1 gives a brief overview of the nanomaterials.

Chapter 2 deals with the synthesis of ZnO nanoparticles and pure and nitrogen-doped ZnO nanorods by solvothermal route and their characterization.

In chapter 3, ZnO and $Al(OH)_3$ nanorods were synthesized in a simple way by the reaction of the metals with liquid water has been discussed. The nanorods so obtained were characterized by various microscopic and spectroscopic methods.

In chapter 4, synthesis of carbon nanostructures and graphite-coated metal nanostructures by the pyrolysis of ruthenocene and ruthenocene-ferrocene mixtures have been discussed.

Chapter 5 deals with the synthesis and characterization of nitrogen- and boron-doped double-walled carbon nanotubes.

Contents

Chapter 1

A Brief Overview of Nanomaterials

1. 1 Introduction

Since the development of the two-cylinder steam engine by James Watt in the 1760s, human-kind has experienced three industrial revolutions [1]. The first industrial revolution, as represented by the appearance of Watt's steam engine, employed various machines to replace human labor. The second industrial revolution began at the end of the 19th century and was earmarked by the discovery of the internal combustion engine and electric generator [2], which led to the increased usage of electrical appliances, automobiles, and petroleum products. The construction of the first computer in the 1940s led to the third industrial revolution, which was followed by the rapid development of information technology [2].

Although many of these inventions and developments provide innumerable benefits, they also pose new and sometimes unforeseeable risks. For example, the emergence of internal combustion engineering led to the wide-spread availability of electric power for lighting, home appliances, industrial machines, automobiles, and aero crafts. However, it also has contributed to the levels of air pollution and accelerated global warming. With the rapid increase in population, consumption of natural resources, environmental pollution, and information overflow, the turn of the last century witnessed the birth of nanotechnology. The demand for miniaturized and multifunctional systems has been a driving force for the development of nanotechnology, *the fourth industrial revolution.*

Owing to the intriguing size-dependent properties of nanophase materials [3], the recent development of nanoscience and nanotechnology has opened up novel fundamental and applied frontiers in materials science and engineering. The concept of nanotechnolgy was first introduced by *Nobel laureate Richard Feynman* [4] in 1959 at the annual meeting of the American Physical Society at the California Institute of Technology (Caltech). In his classic lecture entitled: *"There is plenty of room at the bottom"*, Feynman stated, "The principles of physics, as far as I can see, do not speak against the possibility of maneuvering things atom by atom". Later, Notio Taniguchi from the Tokyo Science University first defined the nanotechnology as: (1) the creation of useful materials, devices, and systems through the control matter at the nanometer (10^{-9} m) length scale and (2) the exploitation of novel properties and phenomena developed at that scale [5]. The first scientific paper on nanotechnology was published in 1981 by Eric Drexler [6], a former student of Dr. Feynman at Caltech. Drexler's [7] idea of molecular manufacturing was followed by his book entitled: *Engines of Creation—The Coming Era of Nanotechnology* published in 1986. In this classic nanotechnology book, Drexler proposed the atom-stacking mechanism to produce machines smaller than a living cell and also presented some potential applications of nanotechnology. Although Drexler's publications have motivated researchers in the field of nanotechnology, the main breakthrough in nanotechnology occurred in 1981 when Binnig and Rohrer [8] at IBM Zurich invented the scanning tunneling microscope (STM), the first instrument to generate real space images of surfaces with atomic resolution. This discovery opened up the important new field of nanotechnology and was recognized by the 1986 Nobel Prize in Physics, along with the inventor of the electron microscope.

1.2 The size and surface effects

Changes in the size-dependent properties can be observed in nanomaterials as the wave-like properties of electrons inside matter and atomic interactions are influenced by the size of materials at the nanometer scale [3]. Confinement of the de Broglie wavelength of charge carriers inside nanomaterials could also lead to new phenomena, such as the quantization effect [3]. When a gold nugget is converted into nanoparticles, for example, the color of the gold particles is changed to black. As the size decreases, the ratio of the surface atoms increases. These high energy surface atoms are very reactive. Due to the high surface-to-volume ratio associated with nanometer-sized materials, a tremendous improvement in chemical properties is also achievable through a reduction in size [3]. This is why platinum nanoparticles can be used as efficient catalysts for many reactions whereas platinum bulk sheets are sufficiently inert as electrodes in electrochemistry. By creating nanostructures, therefore, new materials and advanced devices of desirable properties and functions can be developed for numerous applications

Nanostructures can be defined as systems in which; at least one dimension is less than 100 nm; that is, reducing 1, 2 or 3 dimensions (D) of a bulk material to the nanometer scale produces nanometer thick 2D layers, 1D nanowires, or 0D nanoclusters, respectively. A schematic illustration, showing the density of states versus energy for nanostructures of various dimensions, is given in Figure 1.1.

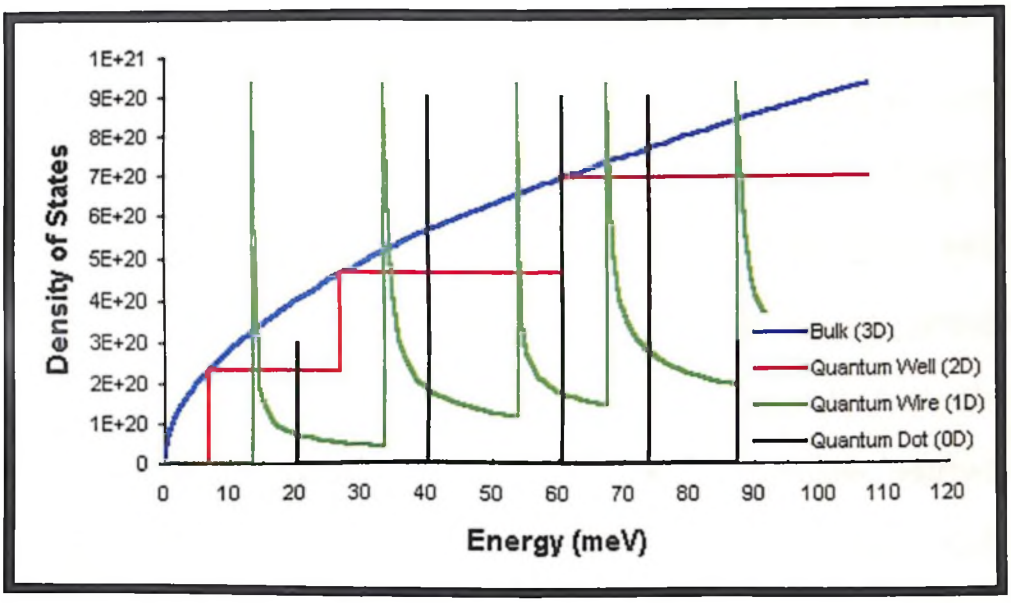

Figure 1.1. Density of states for bulk (blue), quantum well (red), quantum wire (green) and quantum dot (black)

The density of states changes remarkably with dimension. For 2D nanostructures it is a step function with steps occurring at the energy of each quantized level. In the case of 1D nanostructure, van Hove singularities are observed. For 0D nanostructures, the density of states shows quantization at particular energy levels. The quantum confinement of electrons by the potential walls of nanomaterials can provide one of the most powerful means to control the electrical, optical, magnetic, and thermoelectric properties of a solid-state functional material. Suitable control of these properties of nanomaterials can lead to new stream of science as well as new devices and technologies, the underlying theme of nanotechnology [9].

1. 3 Zero-dimensional (0D) nanostructure

Nanocrystals are aggregates of a few hundred or even tens of thousands of atoms that combine into a crystalline form of matter known as a "cluster". Typically a few nanometers in diameter, nanocrystals are larger than molecules but smaller than bulk solids and therefore frequently exhibit physical and chemical properties somewhere in between. Nanocrystals possess high surface area, with a large fraction of its atoms on the surface. Their properties can vary considerably with size. By precisely controlling a nanocrystal's size and surface, its electronic, magnetic, and optical properties can be changed. Due to the confinement of electron wave function to the physical dimensions of the particles in small nanocrystals, electron energy levels are discrete, unlike in the bulk where it is continuous. This phenomenon is called quantum confinement [10]. Therefore, nanocrystals are also known as quantum dots. The nanocrystals can be discretely charged with electrons having characteristic charging energies. The electronic absorption spectrum of metal nanocrystals in the visible region is dominated by the plasmon band and the surface plasmon excitations impart characteristic colors to the metal sols. In semiconductor nanocrystals, exciton peaks dominate the absorption [11,12] The absorption band can be systematically varied by changing the size of the semiconductor nanocrystals.

Semiconductor nanocrystals also exhibit interesting luminescent properties as well [13,14]. For e.g., the emission from monodisperse semiconductor nanocrystals such as CdSe is intense, narrow and can be brought about by excitation in a broad range of wavelengths [14]. The emission can be controlled by controlling the surface structure and the size of the nanocrystals.

1.3.1 Synthetic strategies

Modern materials science is characterized by a close interplay between physics and chemistry. This is especially true for nanomaterials. On the one hand, are the top-down methods which rely on continuous breakup of a piece of bulk matter while on the other are the bottom-up methods that build up nanomaterials from their constituent atoms. The top-down and bottom-up approaches can also be considered to be physical and chemical methods, respectively.

1.3.1.1 Physical methods

Most physical methods involve the evaporation of a solid material to form a supersaturated vapor from which homogenous nucleation of nanoparticles occurs. In these methods, the size of the particles is controlled by temporarily inactivating the source of evaporation, or by slowing the rate by temporarily inactivating the source of evaporation, or by slowing the rate by introducing gas molecules to collide with the particles. Some of the physical methods to prepare nanocrystals are arc dischare, ion sputtering, laser ablation, spray pyrolysis, etc [10].

1.3.1.2 Chemical methods

Chemical methods have emerged to be indispensable for synthesizing nanocrystals of various types of materials. These methods are generally carried out under mild conditions and are relatively straight forward. Any chemical reaction resulting in a sol consists of three steps: seeding, particle growth and growth termination by capping. An important process that occurs during the growth of a colloid is Ostwald ripening. Ostwald ripening is a growth mechanism whereby smaller particles dissolve releasing monomers or ions for consumption by larger particles, the driving force being the lower solubility of large particles. Ostwald ripening limits the ultimate size distribution obtainable to about 15% of the particle diameter when the growth occurs under equilibrium conditions [10].

(a) Metal nanocrystals by reduction

Metal nanocrystals can be obtained by reducing the corresponding soluble metal salts and by terminating the growth with appropriate surfactants or ions. A variety of reducing agents are used to reduce metals salts to get nanocrystals of metals. Some of them are (1) borohydride reduction [15], (2) citrate reduction

Figure 1.2 Michael Faraday's gold colloids

[16], (3) alcohol reduction [17] and (4) reduction using alkylaluminates (AlR_3, R=C_1-C_8) [18]. In 17th century Farady prepared gold nanoparticles in lab by reducing gold salt. He termed them as "divided metal", which giving rise to a brilliant rose colour, as shown in Figure 1.2.

(b) Solvothermal Synthesis

The Solvothermal method provides a means of using solvents at temperatures well above their boiling points, by carrying out the reaction in a sealed vessel. The pressure generated in the vessel due to the solvent vapors elevates the boiling point of the solvent. Typically, solvothermal methods make use of solvents such as ethanol, toluene and water. These are widely used to synthesize zeolites, inorganic open-framework structures and other solid materials. Due to the high pressures employed, one often obtains high-pressure phases of the materials. In the past few years, solvothermal synthesis has emerged to become the chosen method to synthesize nanocrystals [19-20]. Solvothermal methods are ideally suited for the synthesis of nanocrystals of metal chalcogenides and halides, rather than metal nanocrystals.

(c) Photochemical synthesis

Photochemical synthesis of nanoparticles can be carried out by the light induced decomposition of a metal complex or the reduction of metal salts by photogenerated reducing agents such as solvated electrons. The former is called photolysis and the latter radiolysis. The formation of photographic images on AgBr film is a familiar photolysis reaction. Metals such as Au, Cd and Tl, have been obtained by photolysis [21,22]

(d) Arrested precipitation

Nanocrystals can be obtained from solutions that precipitate the bulk matter under conditions unfavorable for the growth of particulates in the precipitate. For example, the precipitation of metals salts by chalcogens can be arrested by employing a high pH. To prepare nanocrystals of CdS, CdSe, CdTe, HgSe, HgTe and CdHgTe, typically, a solution containing the metal salt (perchlorate) and the capping agent is treated with NaOH to raise the pH, degassed by bubbling inert gas (to prevent the oxidation of chalcogen source) followed by the introduction of the chalcogen in the form of Na_2S, NaHSe, etc under inert conditions [10].

(e) The liquid-liquid interface

Nanocrystals and films of metals, semi-conductors and oxides can be produced by reactions taking place at the interface of two liquids such as toluene and water [10]. In this method, a suitable organic derivative of the metal taken in the organic layer reacts at the interface with the appropriate reagent present in the aqueous layer to yield the desired product. For example, by reacting $Au(PPh_3)Cl$ in toluene with THPC in water, nanocrystals of Au can be obtained at the interface of two liquids.

1.3.2 Properties of nanocrystals and their applications

Colloidal semiconductor nanocrystals [23,24] combine the physical and chemical properties of molecules with the optoelectronic properties of semiconductors. Their colour is highly controllable, a direct consequence of quantum confinement on the electronic states. Such nanocrystals find applications in optoelectronic systems such as light emitting diodes and photovoltaic cells, or as components of future nanoelectronic devices [25,26]. The ability to control the electron occupation (especially in n-type or p-type nanocrystals) is important for tailoring the electrical and optical properties.

Shim and Sionnest [27] have reported the fabrication of n-type nanocrystals using an electron transfer approach commonly employed in the field of conducting organic polymers. Pellets of monodisperse nanocrystals have been used for electrical transport measurements [28,29]. An insulator-metal transition has been reported for Au and Ag nanocrystals by Aslam et al. [29].

Studies on both electrical and optical properties of single semiconductor nanocrystals have been carried out [30-33]. All these studies have shown that a single excess charge on a nanocrystal can greatly influence its properties. Klein et al. [34] have reported the fabrication of a single-electron transistor from a colloidal nanocrystal of CdSe. In Figure 1.3 is given a diagram of their device. This device structure actually enables the number of

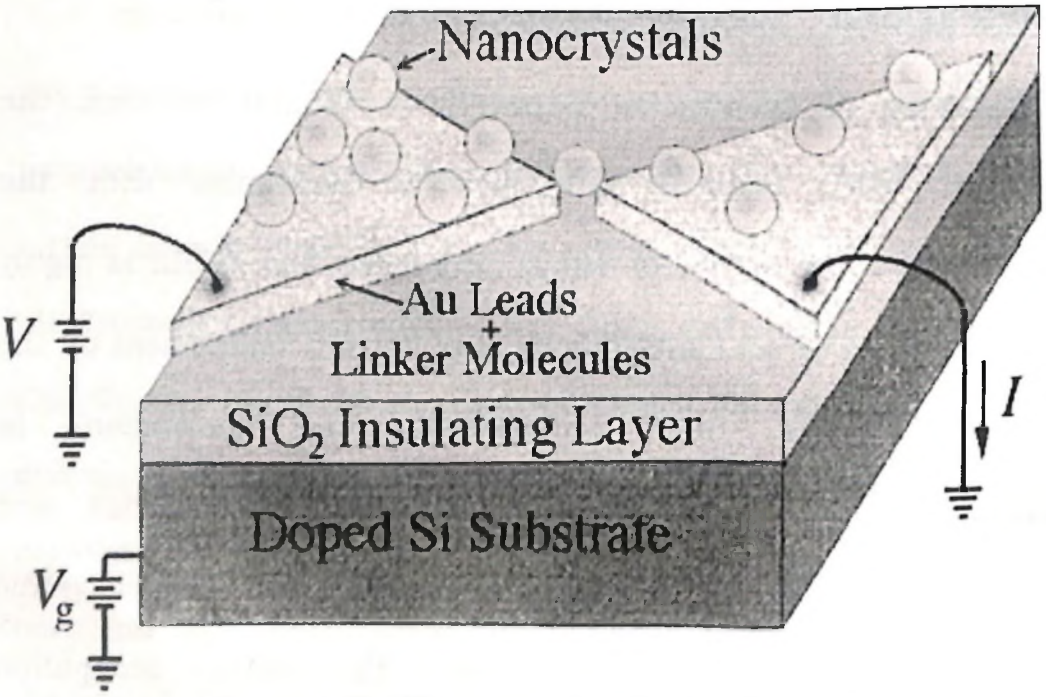

Figure 1.3. Diagram of a single-electron

charge carriers on the nanocrystal to be tuned directly, and in turn the measurement of energy required for the addition of successive charge carriers. Such measurements are invaluable in understanding the energy-level spectra of small electronic systems.

The optical properties of a super lattice of semiconductor nanocrystals are different from those of the individual nanocrystals due to their interparticle interactions [35]. The absorption spectra of nanocrystals get broadened and red-shifted when in a close-packed association, and have been attributed to the interparticle dipolar interactions [36]. Gaponenko and co-workers have shown that the optical properties of an ensemble of small CdSe nanocrystals are similar to those of bulk CdSe due to the complete delocalization of the electronic states of individual nanocrystals [37].

1.4 One-dimensional nanostructures

One-dimensional (1D) nanostructures have attracted much attention as well-defined building blocks to fabricate nanoscale electronic, and optoelectronic devices [38-42]. The formation of various 1D semiconductor nanostructures is believed to be of importance in tailoring the optical, electronic, electrical, magnetic, and chemical properties of 1D nanostructures. In comparison to the zero-dimensional nanostructures (0D), the one-dimensional nanostructures pose as better model systems for investigating the dependence of electronic transport, optical and mechanical properties on the size confinement and dimensionality [41]. They also represent critical components in various nanoscale devices. The synthesis of nanowires with controlled composition, size, purity and crystallinity is no easy task and requires a proper understanding of the nucleation and growth process at the nanometer regime [43]. Many nanolithographic techniques [44], such as proximal-probe patterning [45], electron-beam [46] or focused ion-beam writing [47], etc, have been employed for the synthesis of nanowires and other 1D nanostrctures. Since these physical methods are generally slow and costly, researchers have been investigating chemical routes towards the synthesis of 1D nanostructures [48,49]. The common chemical methods include solution and vapor based methods.

1.4.1 Synthesis of nanowires

Crystallization is the essence of one-dimensional nanostructure formation [50]. When the concentration of the building blocks (atoms, ions or molecules) of a solid becomes sufficiently high, homogenous nucleation takes place, leading to the formation of small nuclei or clusters. Subsequently, larger clusters are formed from these small clusters, which serve as seeds. The formation of a perfect crystal requires a reversible pathway between the building blocks on the solid surface and those in a fluid phase (vapor, solution or melt). These conditions allow the building blocks to easily adopt correct positions in developing the long-range ordered, crystalline lattice. Also, to attain homogeneous composition and uniform morphology, the building blocks have to be supplied at a well-controlled rate.

Vapor-phase growth of nanowires

Vapor-phase synthesis is the most extensively investigated approach to the formation of 1D nanostructures such as whiskers, nanowires and nanorods, due to its simplicity and accessibility. This vapor-phase growth was first observed in the formation of Hg nanofibers by Volmer and Estermann in 1921, when Hg vapor was condensed on a glass surface cooled below the melting point of mercury [51]. An important factor which determines the morphology of the product here is the level of supersaturation. A low supersaturation is required for whisker growth whereas a medium supersaturation leads to bulk growth. At high supersaturation, powders are formed by homogeneous nucleation in the vapor-phase. The two main mechanisms involved in the growth of nanowires in the vapor-phase are (a) vapor-solid and (b) vapor-liquid-solid mechanism.

Vapor-liquid-solid growth

The most extensively studied among the vapor-phase methods is the vapor-liquid-solid (VLS) method. This mechanism was proposed by Wagner in 1960's during his studies on the growth of single-crystalline whiskers of Si and of the metals Pt, Ag, Pd, Cu and Ni [52]. This process has been employed for the synthesis of nanowires of many semiconducting materials such as Si [53], Ge [54,55], ZnO [56], CdS [57], etc. According to this mechanism, a

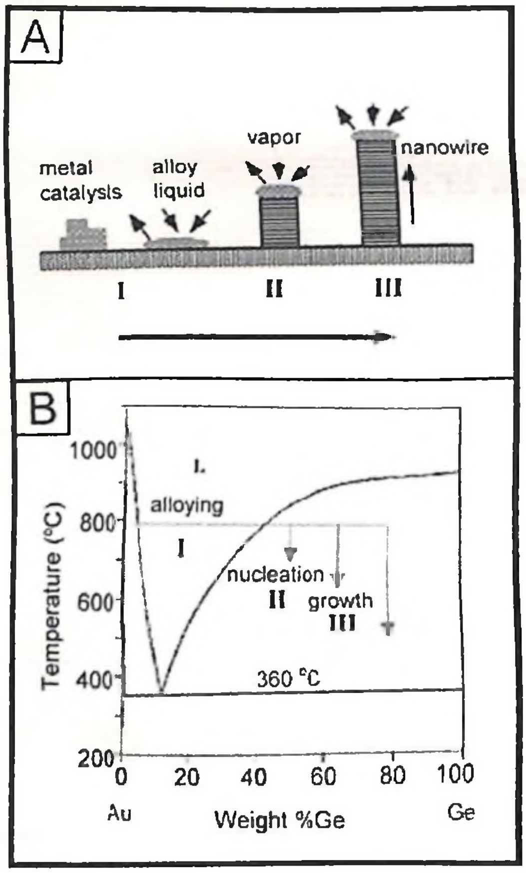

Figure 1.4: (a) Schematic illustration of VLS nanowire growth mechanism including three stages: (I) alloying (II) nucleation, and (III) axial growth. (b) Binary phase diagram of Au-Ge system.

liquid alloy acts as the nucleation site for the formation of the nanowires. First, the gaseous reactant undergoes dissolution into the nanosized liquid droplets of an impurity metal catalyst, and forms a liquid alloy at a temperature higher than the eutectic point. Since the liquid surface has a large accommodation coefficient, it becomes the preferred deposition site for the incoming vapors of the reactant material. After the liquid becomes supersaturated with vapor, the nanowire growth occurs by precipitation at the liquid-solid interface. The different steps involved in the VLS growth are illustrated schematically in Figure 1.4(a).

The selection of a proper metal impurity for the VLS growth is an important criterion. The equilibrium phase diagram helps in the prediction of the catalyst materials to be used, as well as the reaction conditions for the growth of the nanowires. As an example, the Figure 1.4(b) shows the binary phase diagram of the Au-Ge system. Diameter of the nanowires formed by the VLS method is determined by the size of the catalyst particles, which act as soft templates to limit the lateral growth of an individual nanowire. Thus, this method helps in the synthesis of uniform-sized nanowires; and also patterned nanowires through the patterned deposition of catalyst particles.

Vapor-solid growth

Apart from the VLS mechanism, 1D nanostructures have also been grown via the classcal vapor-solid (VS) mechanism [58]. In a typical vapor-solid process, the vapor-species is first generated by physical evaporation, chemical reduction, and other kinds of gaseous reactions. These species are subsequently transported and condensed onto the surface of a solid substrate placed in a cooler zone. A large number of single-crystalline metal oxide nanowires have been grown via this mechanism. Due to the presence of trace amounts of oxygen in reaction systems, majority of the products reported are oxides. Thus, nanowires of oxides of Zn, Mg, Ga, In, Si etc have been synthesized by this method [48]. Apart from nanowires, this process has been adopted for the growth of nanobelts also which are single-crystalline [59].

Carbothermal method

Another very useful and versatile chemical method employed for the synthesis of nanowires is the carbothermal method. Nanowires of a number of oxides such as MgO, ZnO, SnO_2, Ga_2O_3, nitrides such as Si_3N_4, AlN and carbides, such as SiC have been synthesized by this method [60-62]. In a typical carbothermal method a carbon source is heated with a metal oxide in a flowing gas. The carbon sources generally used are activated carbon or charcoal (which are easily oxidized on heating in air) and carbon nanotubes or graphite (which are more stable to oxidation on heating). First, carbon reduces the metal oxide to give a suboxide. The suboxide when heated in the presence of either O_2, N_2/NH_3 or C, gives rise to oxide, nitride or carbide nanowires respectively. In this method, the flow rate of the gas is an important factor, which determines the morphology of the final products.

$$\text{Metal oxide} + C \longrightarrow \text{Metal suboxide} + CO$$

$$\text{Metal suboxide} + O_2 \longrightarrow \text{Metal oxide nanowires}$$

$$\text{Metal suboxide} + NH_3 \longrightarrow \text{Metal nitride nanowires}$$

Solution-based growth of nanowires

The other set of chemical methods adopted for the synthesis of inorganic nanowires is solution-based. This synthetic strategy involves mainly reactions that are confined and directed by templates or by the use of appropriate capping agents. In the template-based technique, the template serves as a scaffold against which other kinds of materials, with morphologies complimentary to that of the template, are generated.

The channels of the templates are filled using a solution route, sol-gel technique or an electrochemical route to produce nanowires. After the reaction, the nanowires could be released from the templates by selectively removing the template from the host matrix. Nanowires of various inorganic materials such as SnO_2, ZnO, Ag, Pt, etc, electronically conducting polymers: polypyrrole and polyaniline, and carbon nanotubules, have been prepared using anodic aluminum oxide membranes (AAMs) [63]. Apart from AAMs and polymer membranes, mesoporous silica have also been used as templates for the synthesis of polymer and inorganic nanowires. Mesophase structures self-assembled from surfactants provide another class of versatile templates for the synthesis of nanowires in large amounts. Carbon nanotubes (CNTs) have been used as templates for the synthesis of inorganic nanowires. By coating CNTs with oxide gels and then burning off the carbon, nanowires of a variety of metal oxides including ZrO_2 [64], SiO_2 [65] and MoO_2 [66] have been prepared.

Apart from the template-based methods, non-template methods, making use of the anisotropic bonding in the crystallographic structures, have also been adopted for the synthesis of inorganic nanowires of Se, Te, molybdenum chalcogenides and polysulfur nitride (SN_x) [67-70].

1.4.2 Properties of nanowires and their applications

Nanowires show very distinct electric, optical, and thermal properties due to their large surface area and possible quantum confinement, when compared with their bulk counterparts. The thermal stability of nanowires is of critical importance for their implementation as building blocks in nanoscale electronic and photonic devices. It is well documented that the melting point of a solid material will be greatly reduced when it is processed as nanostructures [71]. In their investigations on the melting and recrystallization of Ge nanowires encapsulated by carbon-sheaths, Yang and co-workers [72,73] observed the melting point to be inversely proportional to the diameter of the nanowire.

Once the diameter of a nanowire has been reduced below a critical value, size-confinement plays an important role in determining its energy levels. Absorption edge of Si nanowires was found to be considerably blue-shifted when compared with the indirect band gap of bulk Si (~1.1 eV), observed by Korgel et al. [74]. They also observed sharp, discrete features in the absorption spectra and relatively strong band-edge photoluminescence, arising due to quantum confinement effects with additional contributions from the surface states. Lieber and co-workers have shown anisotropy in PL (photoluminescence) intensities in single InP nanowires in directions parallel and perpendicular to the axis of the nanowire [75].

Nanowires and nanotubes are ideal building blocks for nanoscale electronics and optoelectronics. Nanowires of semiconducting elements such as Si and Ge, as well as those of ZnO, InP, GaN, CdS, etc have been studied extensively, towards their applications in nanotechnology. These nanowires have been assembled into nanometric scale devices including FETs, LEDs, p-n junction diodes, logic gates and sensors.

1.4.3 Carbon nanotubes

With the revolutionary discoveries of the C_{60} molecule [76] and carbon nanotubes [77], carbon nanomaterials have become the building block of the entire field of nanotechnology. Exhibiting interesting electronic, mechanical and structural properties; Carbon nanotubes (CNTs) are extremely promising for applications in materials science, engineering and medicinal chemistry. CNTs consist of graphitic sheets, which have been rolled up into a cylindrical shape. The length of CNTs goes up to hundreds of micrometers and their diameters range from 1-50 nm.

Carbon has long been known to exist in three forms: amorphous carbon, graphite, and diamond [78]. Depending on how the carbon atoms are arranged, their properties vary. For example, the most common form of carbon, graphite, is soft, black, and stable. In graphite, the carbon atoms are located at the corners of regular and fused hexagons arranged in parallel layers and its density is 2.26 g/cm^3. However, diamond is hard and transparent due to its regular repetitive pattern, where each carbon atom is bound to four other carbon atoms and its density of 3.51 g/cm^3 is greater than that of graphite. The Noble-Prize-winning discovery of buckminsterfullerene created an entirely new branch of carbon chemistry. The subsequent discovery of carbon nanotubes by Iijima [77] opened up a new era in materials science and nanotechnology [79-81]. Nanodiamonds and nanographenes are the most recent additions to members of the carbon family.

Fullerenes were discovered by Kroto et al. [76] in 1985 while investigating the nature of carbon present in interstellar space. The coordination at every carbon atom in fullerenes is not planar, but slightly pyramidalized, with some sp^3 character present in the essentially sp^2 carbons. The key feature is the presence of five-membered rings, which provide the curvature necessary for forming a closed-cage structure. C_{60} having truncated icosahedral structure formed by 12 pentagonal rings and 20 hexagonal rings. Carbon nanotubes are concentric graphitic cylinders closed at either end due to the presence of five-membered rings. Nanotubes can be multi-walled with a central tubule of nanometric diameter surrounded by graphitic layers separated by ~3.4 Å. Unlike the multi-walled nanotubes (MWNTs), in single-walled nanotubes (SWNTs), there is only the tubule and no graphitic layers. Whereas, Double-walled carbon nanotubes (DWNTs) occupy a position between MWNTs and SWNTs, consist of two concentric cylinders of rolled graphemes, a smallest MWNT. A transmission electron microscope (TEM) image of a MWNT is shown in Figure 1.5(a). In this nanotube, graphite layers surround the central tubule. Figure 1.5(b) shows the structure of a double-walled nanotube formed by two concentric graphitic cylinders. A single-walled nanotube can be visualized by cutting C_{60} along the center and spacing apart the hemispherical corannulene end-caps by a cylinder of graphite of the same diameter. Figure 1.5c shows the bundles of SWNTs. Carbon nanotubes are the only form of carbon with extended bonding and yet with no dangling bonds. Since carbon nanotubes are derived from fullerenes, they are referred to as tubular fullerenes or bucky tubes.

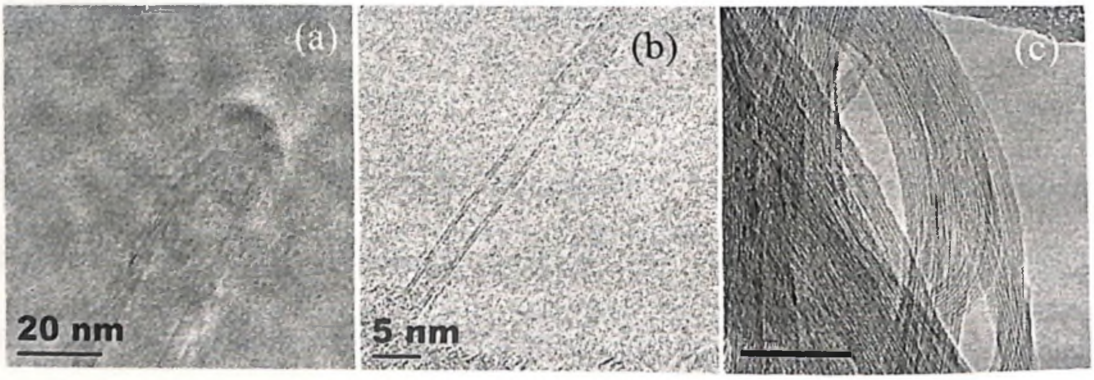

Figure 1.5 shows TEM images of (a) multi-walled, (b) double-walled and (c) single-walled carbon nanotubes

1.4.3.1 Synthesis of carbon nanotubes

Ever since the discovery of the carbon nanotubes [77], several ways of preparing them have been explored. CNTs have been prepared by various methods e.g. electric arc discharge, laser evaporation and chemical vapor deposition. These methods are described in following sections.

Electric-arc discharge

Carbon nanotubes (CNTs) are commonly prepared by striking an arc between graphite electrodes in an inert atmosphere (argon or helium), the process that also produces carbon soot containing fullerene molecules [76]. The carbon arc provides a convenient and traditional tool for generating the high temperatures needed to vaporize carbon atoms into a plasma (>3000 °C) [82-84]. The yield of CNTs depends on the stability of the plasma formed between the electrodes, the current density, inert gas pressure and cooling of electrodes and chamber [82,84]. For the MWNTs production, the conditions are optimized so that during the arc evaporation, the amount of soot production is minimized and 75% of the evaporated carbon from a pure graphite anode is made to deposit onto the facing graphite cathode surface. The optimized synthesis conditions 20-25 V, 50-100 Amp. d.c. (direct current) and the helium pressure maintained at 500 torr. Arc discharge is a simple process, and it is an excellent method to obtain structurally high quality CNTs.

In the arc discharge method, synthesis of MWNTs requires no catalyst, catalyst species are however, necessary for the growth of SWNTs. The first report on the production of SWNTs was by Ijima and Ichihashi [85]. These authors produced SWNTs material by arcing Fe-graphite electrode in a methane+argon atmosphere. A hole was made in the graphite anode, which was filled with a composite mixture of metal and graphite powders, while the cathode being pure graphite. The catalyst generally used to prepare isolated SWNTs include transition metals such as Fe, Co, Ni and rare earth metals such as Y and Gd [85-89], whereas composite catalyst such as Fe/Ni and Co/Ni have been used to synthesize ropes (bundles) of SWNTs [90]. In these experiments, the tubes exhibited an average diameter of 1.2 nm. Saito et al [91] compared SWNTs produced by using different catalysts and found that a Co or a Fe/Ni bimetallic catalyst gives rise to tubes forming a highway-junction pattern. Ni catalyst yield long and thin tubes radially growing from the metal particles. High yield of SWNTs has been synthesized by d.c. arc discharge under low pressure of helium gas (100 torr) with a small amount of a mixture of Ni, Fe and graphite powders [92]. In addition, they introduced sulfur promoter to improve the yield, which gave rise to again the highest yield at low gas pressure.

Laser vaporization

An efficient route for the synthesis of bundles of SWNTs with a narrow size distribution is the laser evaporation technique. In this method, a piece of graphite target is vaporized by laser irradiation under high temperature in an inert atmosphere. MWNTs were obtained when a pure graphite target was used [93]. The quality and yield of these products have been found to depend on the reaction temperature. The best quality is obtained at 1200 ^{o}C reaction temperature. At lower temperatures, the structure quality decreases and the CNTs start presenting many defects. As soon as small quantities (few percents or less) of transition metals (Ni, Co) playing the role of catalysts are incorporated into the graphite pellet, the yielded products undergo significant modifications and SWNTs are formed instead of MWNTs. The yield of SWNTs strongly depends on the type of the metal catalyst used and is seen to increase with furnace temperature, among other factors. A high yield with about 50% conversion of transition-metal/graphite composite rods to SWNTs was reported in the condensing vapor in a heated flow tube (operating at 1200 ^{o}C) [94]. Depending on the metal catalyst used, the yield on the mono or bimetal catalysts are ordered as follows: Ni>Co>Pt>Cu or Nb and Co/Ni, Co/Pt>Ni/Pt>Co/Cu, respectively. A remarkably high nanotube yield of 50% on a Co/Ni run might have resulted from some uncertainty in the process of catalyst preparation and pretreatment [95].

Unfortunately, the laser technique is not economically advantageous because the process involves high-purity graphite rods, the laser powers required are high (in some cases two laser beams are required), and the amount of CNTs that can be produced per day is not as high as arc discharge method.

Chemical vapor deposition

Chemical vapor deposition (CVD) is one of the most popular thin film deposition methods. CVD is very different from the other two common methods used for CNT production, namely electric arc discharge and laser vaporization [96,97]. Arc discharge and laser vaporization can be classified as high temperature (>3000 °C) and short time reaction (μs-ms) techniques, whereas catalytic CVD is a medium temperature (500-1100 °C) and long time reaction (typically minutes to hours) technique. The main technological drawbacks with arc discharge and laser vaporization are that the CNTs are produced as stand alone on their own [98,99]. The CNTs do not grow on a conventional or patterned substrate.

A major advantage of CVD is that the CNTs can be used directly without further purification unless the catalyst particle is required to be removed. In CVD method, CNTs are grown by decomposing an organic gas over a substrate covered with metal catalyst particles. Some CVD methods are reported, such as: thermal CVD, plasma enhanced CVD and catalytic pyrolysis of hydrocarbon.

A thermal CVD reactor is simple and inexpensive to construct and consists of a quartz tube enclosed in a furnace. The substrate material may be Si, mica, silica, quartz or alumina. The nature and yield of the deposit obtained in the reaction are controlled by varying different parameters such as the nature of the catalytic metals and their supports, the hydrocarbon sources, the gas flows, the reaction temperature, and the reaction time, etc. By selecting proper conditions, both the physical (e.g. length, shape, diameter) and chemical properties (e.g. defects, graphitization) of CNTs can be designed in advance. Most of the thermal CVD methods employed for the production of MWNTs use acetylene (C_2H_2) or ethylene (C_2H_4) gas as the carbon feedstock and Fe, Ni or Co nanoparticles as the catalyst. The growth temperature is typically in the range 500-900 ^{o}C. At these temperatures, the carbon atoms dissolve in the metal nanoparticles, which eventually become saturated. The carbon then precipitates to form CNTs, the diameters of which are determined by the sizes of the metal particles, which act as catalyst. When other elements (e.g. Cu, Cr, Mn) are used, only a negligible amount of CNTs is formed [100-102].

Plasma-enhanced chemical vapor deposition (PECVD) is a promising up-coming growth technique for the selective positioning and vertical alignment of CNTs. Vertical alignment is important in applications. This is very useful in field emitters, which are currently being considered for use in flat panel displays. The conventional wisdom in choosing plasma processing is that the precursor is dissociated by highly energetic electrons and as a result, the substrate temperature can be substantially lower than that in thermal CVD. The CNTs have been deposited from various plasma techniques such as hot filament PECVD, microwave PECVD, d.c. (glow discharge) PECVD, and inductively coupled PECVD and rf PECVD. It is clearly evident from these methods that PECVD is a high yield and controllable method of producing vertically aligned CNTs [103].

Catalytic Pyrolysis of Hydrocarbon is the commonly used technique for the bulk production of CNTs by CVD. The main advantage of using this technique is that purification is not required to recover CNTs from the substrate. The simplest method is to inject catalyst nanoparticles (e.g. in the form of a colloidal/particle suspension or organometallic precursors with a carbon feedstock) directly into the CVD chamber. Organometallic compounds (e.g. metallocenes, iron pentacarbonyl and iron (II) phthalocyanine) are often used as precursors for the catalyst [104-110]. These precursors on heating usually get sublimed and catalyst nanoparticles are formed *in situ* when the compound is decomposed/reduced by heat or hydrogen. A double stage furnace is typically needed because of the different temperatures needed for organometallic sublimation and nanotube growth. In general, the sublimation of metallocenes offers little control over the structural parameters of the nanotubes such as length and diameter. However, it has been shown that by varying the reactive concentration of the metallocene to carbon in the gas phase the average diameter of the structures may be changed [110-111].

1.4.3.2 Chemically modified nanotubes

Doping with boron and nitrogen

Since the discovery of the carbon nanotubes, there has been interest in substituting carbon with other elements. Accordingly, boron-carbon (B-C), boron-carbon-nitrogen (B-C-N) and carbon-nitrogen (C-N) nanotubes have been prepared and characterized. Boron-substitution in the carbon nanotubes gives rise to p-type doping and nitrogen-doped carbon nanotubes correspond to n-type doping. Novel electron transport properties are expected of such doped nanotubes [112]. Boron-doped carbon nanotubes have been synthesized by carrying out the pyrolysis of mixtures of acetylene and diborane and characterized by employing microscopic and spectroscopic techniques [113]. B-C-N nanotubes have been prepared by striking an arc between a graphite anode filled with B-N and a pure graphite cathode in a helium atmosphere [114]. B-C-N nanotubes have also been obtained by laser ablation of a composite target containing B-N, carbon, Ni and Co at 1000 °C under flowing nitrogen [115]. Terrones et al. [116] pyrolyzed the addition compound $CH_3CN:BCl_3$ over Co powder at 1000°C to obtain B-C-N nanotubes. B-C-N as well as C-N nanotubes were prepared by Sen et al. [117] by the pyrolysis of appropriate precursors. Pyrolysis of aza-aromatics such as pyridine over Co catalysts gives C-N nanotubes ($C_{33}N$ on average). Pyrolysis of the 1:1 addition compound of BH_3 with $(CH_3)_3N$ produces B-C-N nanotubes. Furthermore, considerable variability exists in the composition in any given batch of B-C, B-C-N or C-N nanotubes obtained by the pyrolysis of precursors.

Nath et al. [118a] have obtained aligned carbon-nitrogen nanotube bundles by the pyrolysis of pyridine over sol-gel-derived iron/silica or cobalt/silica substrates. Employing anodic alumina, Sung et al. [118b] synthesized the C-N nanotubes by electron cyclotron resonance CVD, using C_2H_2 and N_2. Suenaga et al. [119]

carried out CVD of Ni-phthalocyanine to obtain aligned C-N nanotubes.

1.4.3.3 Characterization and Properties of Carbon Nanotubes

MWNTs can be conceived as multi-layered concentric cylinders of single graphitic (graphene) sheets. The diameter of the inner tube is of the order of a few nanometers while the outermost tubes could be as large as 10-30 nm. Helicity is introduced during the curling of a graphene sheet which is well-established by the electron diffraction studies. This suggests that the growth of the nanotubes occurs as in the spiral growth of crystals. Concentric cylinders in MWNTs are separated by about 3.45 Å, which is close to the separation between the (002) planes of graphite. CNTs being capped by dome-shaped hemispherical fullerene-type units don't have dangling bonds at their tips as is generally expected of the graphitic cylinders. SWNTs can be visualized by cutting the C_{60} structure across the middle and adding a graphite cylinder of the same diameter. Two types of non-chiral nanotubes occur in nature: armchair and zigzag. If C_{60} is bisected normal to a five fold axis, an armchair tube is formed, and if it is bisected normal to a three-fold axis then a zigzag tube is formed. Apart from these, various chiral tubes can be formed with the screw axis along the axis of the tube. The models of the three types of nanotubes: zigzag, armchair and chiral nanotubes shown in Figure 1.6.

A chiral angle θ and a chiral vector **C** is used to define a nanotube. Equation 1.1 below gives the value of **C** in terms of $\mathbf{a_1}$ and $\mathbf{a_2}$ which are unit vectors in a 2D graphene lattice and n and m are integers.

$$\mathbf{C} = n\mathbf{a_1}+m\mathbf{a_2} \qquad \text{..........} (1.1)$$

Two crystallographically equivalent sites on a 2D graphene sheet are connected by the vector **C** and the chiral angle is the angle it makes with respect to the zigzag direction (Figure 1.7). A tube is formed by rolling up the graphene sheet in such a way that the two points connected by the chiral vector coincide. Many number of chiral vectors can be envisaged in terms of pairs of inetegers (n,m), the limiting cases being n = m ≠ 0 (armchair tube) and n ≠0, m=0 (zigzag tube). For a nanotube defined by the index

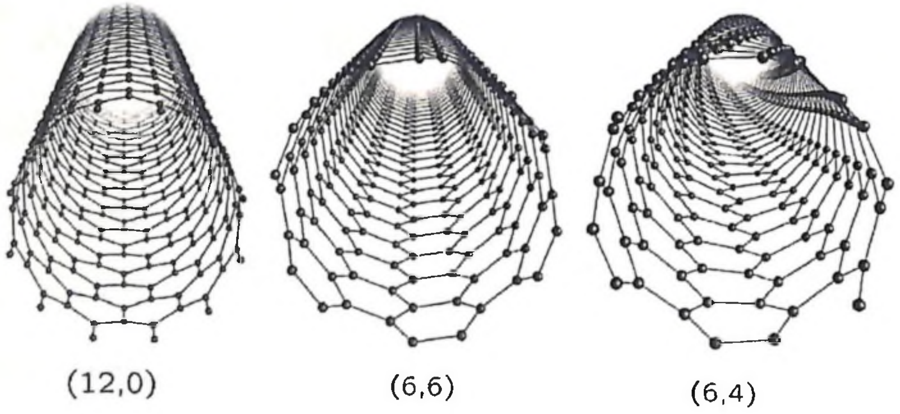
(12,0) (6,6) (6,4)

Figure 1.6 atomic structures of (12, 0) zigzag, (6, 6) armchair and (6, 4) chiral nanotubes

(n, m), the diameter, d, and the chiral angle, θ, are given in following equations 1.2 and 1.3, where a=1.42 $(3)^{1/2}$ and $0 \leq \theta \leq 30°$.

$$D = a\,(m^2 + mn + n^2)^{1/2}/\pi \qquad ....(1.2)$$

$$\theta = \arctan(-(3)1/2\,m)/2n + m) \qquad ....(1.3)$$

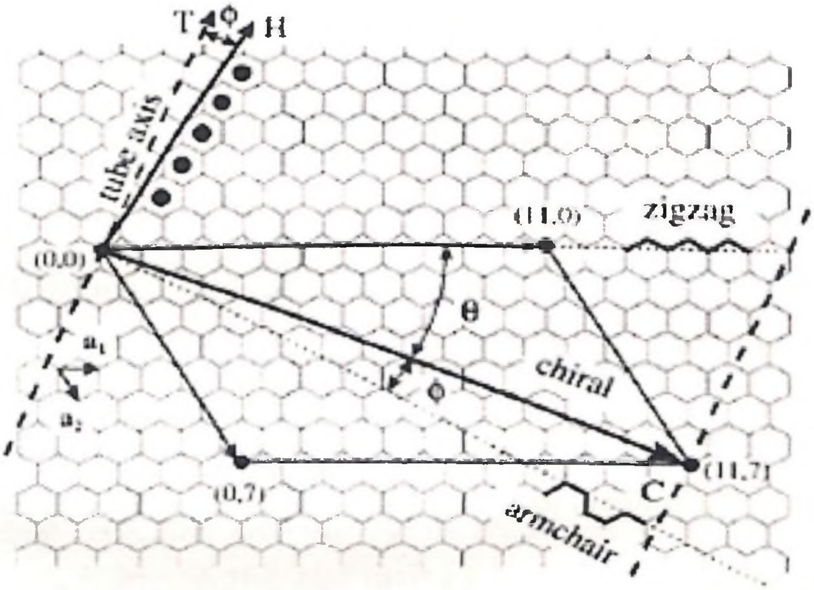

Figure 1.7 The construction of a CNT from a single graphene sheet. By rolling up the sheet along the wrapping vector C, that is, such that the origin (0,0) coincides with point C, a nanotube indicated by indices (11, 7) is formed. Wrapping vectors along the dotted lines lead to tubes that are zigzag or armchair

Among the various characterization techniques, Raman spectroscopy, electron microscopy, diffraction techniques, UV-Vis spectroscopy are the most extensively used. The XRD pattern of MWNTs show only the (hk0) and the (001) reflections but no (hkl) reflections [120]. Lot of information regarding the structure of the nanotubes can be (and has already been) acquired from Raman spectroscopy. Using a zone-folding model, Jishi et al. [121] have calculated the Raman active phonon modes in the nanotubes. The diameter and the chiral angle of the tube determine the frequency of the allowed modes. Rao et al. [122] observed the diameter selective resonance behavior of SWNTs. Resonant Raman spectroscopy on isolated nanotubes has been used to determine the index (n, m) of the nanotube [123].

Several growth mechanisms are proposed for the formation of CNTs by the pyrolysis of hydrocarbons on the metal surfaces. The one suggested by Baker and Harris [124] has four steps in it. First step involves the decomposition of hydrocarbon on the metal surface to release hydrogen and carbon, which dissolves in the particle. In the second step, carbon diffuses through the metal particle and precipitates on the rear face to form the body of the filament. In step three, carbon forms a skin around the main filament body due the surface diffusion which helps in removing the carbon from the front face and hence keeps the active surface unblocked. Fourth step witnesses the overcoating and deactivation of the catalyst and subsequent termination of the tube growth.

Oberlin et al. [125] proposed a mechanism in which bulk diffusion is insignificant and carbon is entirely transported around the particle by surface diffusion while Dai et al. [126] proposed a mechanism wherein carbon forms a hemispherical graphene cap on the catalyst particle and the nanotubes grow from such a yarmulke. An important feature of this model is that it avoids dangling bonds at all stages of growth.

Apart from the above models, a number of growth models have also been proposed for the growth of MWNTs in the arc discharge method. Endo and Kroto [127] suggested that the tube formation process is a consequence of formation of fullerenes. Smalley, however pointed out that only the growth of outer layers is possible through such a mechanism. Iijima [128], on the other hand suggested that the termination of incomplete layers of carbon seen on the surface may arise because of the extension and thickening of the nanotubes by the growth of graphite islands on the surfaces of existing tubes. The nucleation of pentagons and heptagons on the open tube ends results in a change in the direction of the growing tube and some novel morphologies, including one where the tube turns around 180° during the growth, have been observed.

1.4.3.4 Applications of carbon nanotubes

The wide range of fascinating properties of carbon nanotubes provides attractive opportunities for potential technological applications [129,130].

Carbon nanotubes can be used as electron sources for field-emission (FE) displays. Electrons can be easily emitted from CNT tips when a potential is applied between the CNT surface and an anode [131-138]. In particular, B-doped CNTs could exhibit enhanced field emission when compared to pristine CNTs. This phenomenon arises from the preferential presence of B atoms at the nanotube tips, which results in an increased DOS close to the Fermi level.

Because of the high electrochemically accessible surface area of porous nanotube arrays, combined with their high electronic conductivity and useful mechanical properties, these materials are attractive as electrodes for devices that use electrochemical double-layer charge injection. Examples include supercapacitors, which have giant capacitances in comparison with those of ordinary dielectric-based capacitors, and electromechanical actuators that may eventually be used in robots [139-142].

SWNTs have also been grown directly onto atomic force microscope tips [143] to offer significant improvements in lateral AFM resolution, as compared with commercial silicon AFM tips.

The resistance of SWNTs has also been found to be sensitive to various gases [144] implying sensor applications. It has been demonstrated by various groups [145,146] that pure carbon SWNTs and MWNTs can be used to detect toxic gases and other species, because small concentrations are capable of producing large changes in the nanotubes conductance, shifting the Fermi level to the valence band, and generating hole-enhanced conductance. However, N-doped MWNTs have proved to be more efficient in this context.

SWNTs have nano-sized channels which can facilitate adsorption of liquids or gases. The adsorption properties of SWNTs with respect to methane, benzene and nitrogen have been studied [147]. The studies indicate that SWNTs are good microporous materials with a total surface area above 400 m^2/g. The unique hexagonal packing of the SWNTs in the bundles offers ideal channels, thus allowing the realization of one-dimensional (1D) adsorbates.

Reference

1. J. Gribbin, The Scientists, Random House, New York, **2004**.
2. T. Philbin, The 100 Greatest Inventions of All Time, Kensington Publishing Corp., New York, **2003**.
3. A. N. Goldstein, Handbook of Nanophase Materials, Marcel Dekker, Inc., New York, **1997**.
4. R. P. Feynman, A lecture in engineering science, in California Institute of Technology, February, **1960**.
5. L. Dai, Carbon nanotechnology, Elsevier, **2006**.
6. E. K. Drexler, *Proc. Natl. Acad. Sci. USA* **1981**, *78*, 5275.
7. E. K. Drexler, Engines of Creation—The Coming Era of Nanotechnology, Anchor Press/Doubleday, Garden City, N.Y, **1986**.
8. G. Binnig and H. Rohrer, *Rev Mod. Phys.* **1987**, *59,* 615.
9. Y. Xia, P. Yang, Y. Sun, Y. Wu, B. Mayers, B. Gates, Y. Yin, F. Kim, and H. Yan *Adv. Mater.*, **2003**, 15, 353.
10. G. U. Kulkarni, P. J. Thomas, and C. N. R. Rao in The Chemistry of Nanomaterials, p. 51, Wiley-VCH, Weinheim, **2004**.
11. T. Vossmeyer, L. Katsikas, M. Giersig, I. G. Popovic, K. Diener, A. Chemseddine, A. Eychmuller, and H. Weller *J. Phys. Chem.*, **1994**, *98*, 7665.

12. O. I. Micic, Jones, K. M., A. Cahill, and A. J. Nozik *J. Phys. Chem. B.*, **1998**, *102*, 9791.
13. M. Bruchez, M. Moronne, P. Gin, S. Weiss, and A. P. Alivisatos *Science*, **1998**, *281*, 2013.
14. X. S. Peng, G. W.Meng, X. F. Wang, Y. W. Wang, J. Zhang, and L. D. Z. X. Liu *Chem. Mater.*, **2002**, *14*, 4490.
15. R. G. Nuzzo, D. L. Allara *J. Am. Chern. Soc.* **1983**, 1054481.
16. A. Harriman, G. R. Millward, P. Nata et al *J. Phys. Chem.* **1988**, *92*, 1286.
17. D. Mandler, 1. Vlilner *J. Phys. Chem.* **1987**, *91*, 3600.
18. K. L. Tsai, J. L. Dai *Chem. Mater.***1993**, *5*, 540.
19. S. H. Yu, J. Yang, Z. H. Han et al *J. Mater. Chem.* **1999**, *9* 1283.
20. X. Chen, R Fan *Chem. Mater.* **2001**,13802.
21. M. Y. Han, L. Zhow, C. H. Quek et al *Chern. Phys. Lett.* **1998**, *287*, 47.
22. M. Marandi, N. Taghavinia, A. 1. Zad et al *Nanotechnolgy* **2005**,*16*, 334.
23. M. Nirmal and L. E. Brus *Acc. Chem. Res.*, **1999**, *32*, 407.
24. A. P. Alivisatos *Science*, **1996**, *271*, 933.
25. V. L. Colvin, M. C. Schlamp, and A. P. Alivisatos *Nature*, **1994**, *370*, 354.

26. B. O'Regan and M. Gratzel *Nature*, **1991**, *353*, 737.

27. M. Shim and P. Guyot-Sionnest *Nature*, **2000**, *407*, 26.

28. M. Brust, D. J. Schiffrin, D. Bethell, and C. J. Kiely *Adv. Mater.*,**1995**, *7*, 795.

29. M. Aslam, I. S. Mulla, and K. Vijayamohanan *Appl. Phys. Lett.*, **2001**, *79*, 689.

30. B. Alperson, S. Cohen, I. Rubinstein, and G. Hodes *Phys. Rev. B*, **1995**, *53*, 17017.

31. D. L. Klein, P. L. McEuen, J. E. Bowen Katari, and A. P. Alivisatos *Appl. Phys. Lett.*, **1996**, *68*, 2574.

32. S. A. Blanton, A. Dehestani, P. C. Lin, and P. Guyotsionnest *Chem.Phys. Lett.*, **1994**, *229*, 1994.

33. S. A. Empedocles, D. J. Norris, and M. G. Bawendi *Phys. Rev. Lett.*, **1996**, *77*, 3873.

34. D. L. Klein, R. Roth, A. P. A. A. K. L. Lim, and P. L. McEuen *Nature*, **1997**, *389*, 699.

35. C. B. Murray, C. R. Kagan, and M. G. Bawendi *Ann. Rev. Mater. Sci.*, **2000**, *30*, 545.

36. M. V. Artemyev, U. Woggon, H. Jaschinski, L. I. Gurinovich, and S. V. Gaponenko *J. Phys. Chem. B*, **1999**, *104*, 11617.

37. M. V. Artemyev, A. I. Bibik, L. I. Gurinovich, S. V. Gaponenko, and U. Woggon *Phys. Rev. B.*, **1999**, *60*, 1504.

38. X. Duan, Y. Huang, Y. Cui, J. Wang and C.M. Lieber, *Nature*, **2001**, *409*, 66.

39. G.Y. Tseng and J.C. Ellenbogen, *Science*, **2001**, *294*, 1293.

40. N.A. Melosh, A. Boukai, F. Diana, B. Gerardot, A. Badolato, P.M. Petroff and J.R. Heath, *Science*, ***2002***, *300*, 112.

41. Y. Xia, P. Yang, Y. Sun, Y. Wu, B. Mayers, B. Gates, Y. Yin, F. Kim and H. Yan, *Adv.Mater.* **2003**, *15*, 353.

42. C.N.R. Rao, F. L. Deepak, G. Gundiah and A. Govindaraj, *Prog. Solid State Chem.* **2003**, *31*, 5.

43. A. Govindaraj and C. N. R. Rao in The Chemistry of Nanomaterials (C. N. R. Rao, A. Muller, and A. K. Cheetham, eds.), p. 208, Wiley-VCH, Weinheim, **2004**.

44. F. Cerrina and C. Marrian *MRS Bull.*, **1996**, *21*, 56.

45. S. Hong, J. Zhu, and C. A. Mirkin *Science*, **1999**, *286*, 523.

46. S. Matsui and Y. Ochiai *Nanotechnology*, **1996**, *7*, 247.

47. J. M. Gibson *Phys. Today*, **1997**, 56.

48. C. N. R. Rao, F. L. Deepak, G. Gundiah, and A. Govindaraj *Prog. Solid State Chem.*, **2003**, *31*, 5.

49. Y. Xia, J. A. Rogers, K. E. Paul, and G. M. Whitesides *Chem. Rev.*, **1999**, *99*, 1823.

50. E. I. Givargizov in Highly Anisotropic Crystals (M. Senechal and S. College, eds.), Reidel, Dordrecht, The Netherlands, **1987**.

51. M. Volmer and I. Estermann, *Z. Phys.* **1921,** *7*, 13.
52. R. S. Wagner and W. C. Ellis, *Appl. Phys. Lett.,* **1964**, *4*, 89.
53. A. M. Morales and C. M. Lieber, *Science*, **1998**, *279*, 208.
54. Y. Wu and P. Yang, *J. Am. Chem. Soc.*, **2001**, *123*, 3165.
55. Y. Wu and P. Yang, *Chem. Mater.*, **2000**, *12*, 605.
56. M. H. Huang, Y. Wu, H. Feick, N. Tran, E. Weber, and P. Yang, *Adv. Mater.*, **2001**, *13*, 113.
57. Y. Wang, G. Meng, L. Zhang, C. Liang, and J. Zhang, *Chem. Mater.*, **2002**, *14*, 1773.
58. R. S. Wagner in Whsiker Technology (A. P. Levitt, ed.), p. 47, Wliey-Interscience, New York, **1970**.
59. Z. W. Pan, Z. R. Dai, and Z. L. Wang *Science*, **2001**, *291*, 1947.
60. C. N. R. Rao, G. Gundiah, F. L. Deepak, A. Govindaraj, and A. K.Cheetham *J. Mater. Chem.,***2004**, *14*, 440.
61. P. Yang and C. M. Lieber *J. Mater. Res.*, **1997**, 12, 2981.
62. P. Yang and C. M. Lieber *Science*, **1996**, *273*, 1836.
63. Huczko *Appl. Phys. A: Mater. Sci. Process*, **2000**, *70*, 365.
64. B. C. Satishkumar, A. Govindaraj, E. M. Vogl, L. Basumallick, andC. N. R. Rao *J. Mater. Res.*, **1997**, *12*, 604.
65. B. C. Satishkumar, A. Govindaraj, M. Nath, and C. N. R. Rao *J. Mater. Chem.*, **2000**, *10*, 2115.

66. C. N. R. Rao, B. C. Satishkumar, and A. Govindaraj *Chem. Comm.*, **1997**, 1581.

67. J. Stejny, R. W. Trinder, and J. Dlugosz *J. Mater. Sci*, **1981**, *16*, 3161.68. B. Gates, B. Mayers, and B. Cattle *Adv. Funct. Mater.*, **2002**, 12, 219.

69. B. Mayers and Y. Xia *J. Mater. Chem.*, **2002,** *12*, 1875.

70. B. Messer, J. H. Song, and M. H. et al. *Adv. Mater.*, **2000**, *12*, 1526.

71. P. Buffat and J. P. Borel *Phys. Rev.*, **1976**, *13*, 2287.

72. Y. Wu and P. Yang *Adv. Mater.*, **2001**, *13*, 520.

73. Y. Y. Wu and P. Yang *Appl. Phys. Lett.*, **2000**, *77*, 43.

74. X. Lu, T. Hanrath, K. P. Johnston, and B. A. Korgel *Nano Lett.*, **2003**, *3*, 93.

75. J. F. Wang, M. S. Gudiksen, X. F. Duan, Y. Cui, and C. M. Lieber *Science*, **2001**, *293*, 1455.

76. H. W. Kroto, J. R. Heath, S. C. O^Brien, R. F Curl and R. E. Smalley *Nature*, **1985**, *318,* 162.

77. S. Iijima, *Nature*, **1991,** *354***,** 56.

78. H. Marsh, Introduction to Carbon Science, Butterworths, London, **1989**.

79. M. S. Dresselhaus, G. Dresselhaus and P. Eklund, Science of Fullerenes and Carbon Nanotubes, Academic, San Diego, **1996**.

80. M. Meyyappan, Carbon Nanotubes: Science and Applications, CRC Press, Boca Raton, **2005**.
81. P. J. F Harris, Carbon Nanotubes and Related Structures—New Materials for the Twenty-First Century, Cambridge University Press, Cambridge, **2001**.
82. T.W. Ebbesen and P.M. Ajayan, *Nature*, **1992**, *358*, 220.
83. T.W. Ebbesen, H. Hiura, J. Fujita, Y. Ochiai, S. Matsui and K. Tanigaki, *Chem. Phys. Lett.* **1993**, *209*, 83.
84. S. Seraphin, D. Zhou, J. Jiao, J.C. Withers and R. Loufty, *Carbon*, **1993**, *31*, 685.
85. S. Iijima and T. Ichihashi, *Nature*, **1993**, *363*, 603.
86. D.S. Bethune, C.H. Kiang, M.S. de Vries, G. Gorman, R. Savoy, J. Vazquez and R. Beyers, *Nature*, **1993**, *363*, 605.
87. Y. Satio, M. Okuda, N. Fujimoto, T. Yoshikawa, M. Tomita and T. Hayashi, Jpn. *J. Appl. Phys.* **1994**, *33*, L526.
88. D. Zhou, S. Seraphin and S. Wang, *Appl. Phys. Lett.* **1994**, *65*, 1593.
89. S. Subramoney, R.S. Ruoff, D.C. Lorents and R. Malhotra, *Nature*, **1993**, *366*, 637.
90. S. Seraphin and D. Zhou, *Appl. Phys. Lett.***1994**, *64*, 2087.
91. Y. Saito, M. Okuda and T. Koyama, *Surf. Rev. Lett.* **1996**, *3*, 63.

92. Y.S. Park, K.S. Kim, H. J. Jeong, W.S. Kim, J.M. Moon, K.H. An, D.J. Bae, Y.S. Lee, G.S. Park and Y.H. Lee, *Synt. Metals* **2002**, *126*, 245.
93. T. Guo, P. Nikolaev, A.G. Rinzler, D. Tomanek, D.T. Colbert and R.E. Smalley, *J. Phys. Chem.* **1995**, *99*, 10694.
94. T. Guo et al. *Chem. Phys. Lett.* **1995**, *243*, 49.
95. A. Thess, R. Lee, P. Nikolaev, H. J. Dai, P. Petit, J. Robert, C. H. Xu, Y.H. Lee, S.G. Kim, A.G. Rinzler, D.T. Colbert, G.E. Scuseria, D. Tomanek, J.E. Fischer, R.E. Smalley, *Science*, **1996**, *273*, 483.
96. C. Journet, W.K. Maser, P. Bernier, A. Loiseau, M. L. de la Chapelle, S. Lefrant, P. Deniard, R. Lee and J.E. Fischer, *Nature*, **1997**, *388*, 756.
97. A. Thess, R. Lee, P. Nikolaev, H. J. Dai, P. Petit, J. Robert, C. H. Xu, Y.H. Lee, S.G. Kim, A.G. Rinzler, D.T. Colbert, G.E. Scuseria, D. Tomanek, J.E. Fischer and R.E. Smalley, *Science*, **1996**, *273*, 483.
98. G.S. Duesberg, J. Muster, H.J. Byrne, S. Roth and M. Burghard, *Appl. Phys. A*, **1999**, *69*, 269.
99. A.G. Rinzler, J. Liu, H. Dai, P. Nikolaev, C.B. Huffman, F.J. Rodriguez-Macias, P.J. Boul, A.H. Lu, D.Heymann, D.T. Colbert, R.S. Lee, J.E. Fischer, A.M. Rao, P.C. Eklund and R.E. Smalley, *Appl. Phys. A,* **1998**, *67*, 29.

100. A. Fonseca, K. Hernadi, J.B. Nagy, D. Bernaerts and A.A. Lucas, *J. Mol. Catal. A*, **1996**, *107*, 159.

101. A. Fonseca, K. Hernadi, P. Piedigrosso, J.F. Colomer, K. Mukhopadhyay, R. Doome, S. Lazarescu, L.P. Biro, Ph. Lambin, P.A. Thiry, D. Bernaerts and J.B. Nagy, *Appl. Phys. A*, **1998**, *67*, 11.

102. I. Williems, Z. Konya, J.F. Colomer, G. Van Tendeloo, N. Nagaraju, A. Fonseca and J.B. Nagy, *Chem. Phys. Lett.* **2000**, *317*, 71.

103. C. N. R. Rao and A. Govindaraj (2005) *"Nanotubes and Nanowires", The RSC Nanoscience & Nanotechnology series*, (Eds. H. Kroto, P. O'Brien, H. Craighead) Royal Society of Chemistry (London).

104. T. W. Ebbesen, J. Tabuchi and K. Tanigaki, *Chem. Phys. Lett.*, **1992**, *191*, 336.

105. Y. Saito, T. Yoshikawa, M. Inagaki, M. Tomita and T. Hayashi, *Chem. Phys. Lett.*, **1994**, *204*, 277.

106. D. H. Robertson, D. W. Brenner and C. T. White, *J. Phys. Chem.*, **1992**, *96*, 6133.

107. (a) S. Amelinckx, X. B. Zhang, D. Bernaerts. X. F. Zhang, V. Ivanov and J. B. Negy, *Science*, **1994**, *265*, 635.

(b) S. Amelinckx, D. Bernaerts. X. B. Zhang, G. Van Tendeloo and J. Van Landuyt, *Science*, 1995, **267**, 1334.

108. A. Maiti, C. T. Brabec and J. Bernholc, *Phys. Rev. B.*, **1997**, *55*, R6097.

109. A. Moisala, A. G Nasibulin and E.I. Kaeuppinen, *J. Phys.: Condens. Matter.*, **2003**, *15*, S3011.

110. K.Tohji, T. Goto, H. Takahashi, Y. Shinoda, N. Shimizu, B. Jeyadevan, I. Matsuoka, Y. Saito, A. Kasuya, T. Ohsuna, K. Hiraga and Y. Nishina, *Nature*, **1996**, *383*, 679.

111. K. Tohji, T. Goto, H. Takahashi, Y. Shinoda, N. Shimizu, B. Jeyadevan, I. Matsuoka, Y. Saito, A. Kasuya, S. Ito and Y. Nishina, *J. Phys. Chem.*, **1997**, *B101*, 1974.

112. Y. Miyamoto, A. Rubio, M. L. Cohen and S. G. Louie, *Phys. Rev. B*, **1994**, *50*, 4976.

113. B. C. Satishkumar, A. Govindaraj, K. R. Harikumar, J. P. Zhang, A. K. Cheetham and C. N. R. Rao, *Chem. Phys. Lett.*, **1999**, *300*, 473.

114. O. Stephan, P. M. Ajayan, C. Colliex, Ph. Redlich, J. M. Lambert, P. Bernier and P. Lefin, *Science*, **1994**, *266*, 1683.

115. Y. Zhang, H. Gu, K. Suenaga and S. Iijima, *Chem. Phys. Lett.*, **1997**, *279*, 264.

116. M. Terrones, A. M. Benito, C. Mantega-Diego, W. K. Hsu, O. I. Osman, J. P. Hare, D. G. Reid, H. Terrones, A. K. Cheetham, K. Prassides, H. W. Kroto and D. R. M. Walton, *Chem. Phys. Lett.*, **1996**, *257*, 576.

117. (a) R. Sen, B. C. Satishkumar, A. Govindaraj, K. R. Harikumar, G. Raina, J. P. Zhang, A. K. Cheetham and C. N. R. Rao, *Chem. Phys. Lett.*, **1998**, *287*, 671; (b) R. Sen, B. C. Satishkumar, A. Govindaraj, K. R. Harikumar, M. K. Renganathan and C. N. R. Rao, *J. Mater. Chem.*, **1997**, *7*, 2335.

118. (a) M. Nath, B. C. Satishkumar, A. Govindaraj, C. P. Vinod and C. N. R. Rao, *Chem. Phys. Lett.*, **2000**, *322*, 333; (b) S. L. Sung, S. H. Tsai, C. H. Tseng, F. K. Chiang, X. W. Liu and H. C. Shih, *Appl. Phys. Lett.*, **1999**, *74*, 197.

119. (a) K. Suenaga, M. Yusadaka, C. Colliex and S. Iijima, *Chem. Phys. Lett.*, **2000**, *316*, 365; (b) K. Suenaga, M. P. Johansson, N. Hellgren, E. Broitman, L. R. Wallenberg, C. Colliex, J. -E. Sundgren and L. Hultman, *Chem. Phys. Lett.*, **1999**, *300*, 695.

120. R. Sheshadri, A. Govindaraj, H. N. Aiyer, R. Sen, G. N. Subbanna, A. R. Raju, C. N. R. Rao, *Current Science*, **1994**, *66*, 839.

121. R. A. Jishi, L. Venkataraman, M. S. Dresselhaus, G. Dresselhaus, *Chem. Phys. Lett.*, **1994**, *220*, 186.

122. A. M. Rao, E. Richter, S. Bandow, P.C. Eklund, K. A. Williams, S. Fang, K. R. Subbaswamy, M. Meno, A. Thess, R. E. Smalley, G. Dresselhaus, M. S. Dresselhaus, *Science*, **1997**, *275*, 187.

123. M. S. Dresselhaus, G. Dresselhaus, A. Jurio, A. G. Souza Filho, M. A. Pimenta, R. Saito, *Acc. Chem. Res.*, **2002**, *35*, 1070.

124. R. T. K. Baker and P. S. Harris, in *Chemistry and Physics of Carbon*, eds.P. L. Walker, P. A. Thrower, Marcel Dekker, New York, **1978**, *14*.

125. H. Dai, A. Z. Rinzler, P. Nikolaev et al., *Chem. Phys. Lett.*, **1996**, *260*, 471

126. A. Oberlin, M. Endo, T. Koyama, *J. Cryst. Growth.*, **1976**, *32*, 335.

127. M. Endo, H. W. Kroto, *J. Phys. Chem.*, **1992**, *96*, 6941.

128. S. Iijima, P. M. Ajayan, T. Ichihashi, *Phys. Rev. Lett.*, **1992**, *69*, 3100.

129. W. A. de Heer, *MRS Bulletin*, **2004**, *354*, 281.

130. J. Robertson, *Materials Today*, October **2004**, 46.

131. N. de Jonge and J. –M. Bonard, *Phil. Trans. R. Soc. Lond.* A, **2004**, *362*, 2239.

132. W. I. Milne, K.B.K. Teo, G.A.J. Amaratunga, P. Legagneux, L. Gangloff, J.-P. Schnell, V. Semet, V. Thien Binh and O. Groening, *J. Mater. Chem.*, **2004**, *14*, 933.

133. W. A. de Heer, A. Chaˆtelain and D. Ugarte, *Science*, **1995**, *270*, 1179.

134. A. G. Rinzler, J. H. Hafner, P. Nikolaev, L. Lou, S. G. Kim, D. Tomanek, P. Nordlander, D. T. Colbert and R. E. Smalley, *Science*, **1995**, *269*, 1550.

135. N. S. Lee, D. S. Chung, I. T. Han, J. H. Kang, Y. S. Choi, H. Y. Kim, S. H. Park, Y. W. Jin, W. K. Yi, M. J. Yun, J. E. Jung, C. J. Lee, J. H, You, S. H. Jo, C. G. Lee and J. M. Kim, *Diamond Relat. Mater.*, **2001**, *10*, 265.

136. Y. Saito and S. Uemura, *Carbon*, **2000**, *38*, 169.

137. R. Rosen, W. W. Simendinger, C. Debbault, H. Shimoda, L. Fleming, B. Stoner and O. Zhou, *Appl. Phys. Lett.*, **2000**, *76*, 1668.

138. H. Sugie, M. Tanemura, V. Filip, K. Iwata, K. Takahashi and F. Okuyama, *Appl. Phys. Lett.*, **2001**, *78*, 2578.

139. K. H. An, W. S. Kim, Y. S. Park, J.-M. Moon, D. J. Bae, S. C. Lim, Y. S. Lee and Y. H. Lee, *Adv. Funct. Mater.*, **2001**, *11*, 387.

140. C. Niu, E. K. Sickel, R. Hoch, D. Moy and H. Tennent, *Appl. Phys. Lett.*, **1997**, *70*, 1480.

141. C. Niu, J. Kupperschmidt and R. Hock, in *Proceedings of the 39th Power Sources Conference* (Maple Hill, NJ, **2000**), 314–317.

142. R. H. Baughman, C. Cui, A. A. Zakidov, Z. Iqbal, J. N. Berisci, G. M. Spinks, G. G. Wallace, A. Mazzoldi, D. De Rossi,

A. G. Rinzler, O. Jaschinski, S. Roth and M. Kertesz, *Science,* **1999**, *284*, 1340.

143. C. L. Cheung, J.H. Hafner, T.W. Odom, K. Kim, and C.M. Lieber, *Appl. Phys. Lett.* ***2000***, *76*, 3136.
144. J. Kong, N. Franklin, C. Zhou, M. Chapline, S. Peng, K. Cho, and H. Dai, *Science* 2000, *287,* 622.
145. Wong, S. S., et al., *Nature*, **1998,** *394*, 52.
146. Collins, P. G., *Science* **2000**, *287*, 1801.
147. M. Eswaramoorthy, R. Sen and C. N. R. Rao, *Chem. Phys. Lett.* **1999**, *304*, 207.

Chapter 2

Solvothermal Synthesis of ZnO Nanoparticles and Pure and Nitrogen-Doped ZnO Nanorods*

Summary

This chapter of the thesis deals with the synthesis of nanoparticles and nanorods of Zinc oxide (ZnO). Nanoparticles and nanorods of ZnO have been prepared by solvothermal route. It has been possible to obtain nitrogen-doped ZnO nanorods by this method.

The reaction of aliphatic alcohols such as methanol, ethanol and *t*-butanol with zinc powder at 330 °C under solvothermal conditions produces ZnO nanoparticles. The reaction involves the cleavage of the C-O bond of the alcohols, which occurs readily on the Zn metal surface. Addition of ethylenediamine to the reaction mixture yields nanorods, the amine acting as a shape-controlling agent. N-doped ZnO nanorods have been synthesized by adding liquid ammonia to a mixture of zinc acetate, ethylenediamine and ethanol under solvothermal conditions.

---

*Papers based on this study have been published in J. Clust. Sci. (dedicated to Professor Dieter Fenske), 2007, 18(3), 660-670. Mater. Res. Bull. 2007, 42, 2117-2124.

2.1 Introduction

Zinc oxide (ZnO) is a II^b–VI compound semiconductor. The lack of a centre of symmetry in wurtzite, combined with large electromechanical coupling, results in strong piezoelectric and pyroelectric properties and the consequent use of ZnO in mechanical actuators and piezoelectric sensors. In addition, ZnO is a wide band-gap (3.37 eV) compound semiconductor that is suitable for short wavelength optoelectronic applications. The high exciton binding energy (60 meV) in ZnO crystal can ensure efficient excitonic emission at room temperature and room temperature ultraviolet (UV) luminescence. ZnO crystallizes preferentially in the hexagonal wurtzite-type structure. It occurs in nature with the mineral name zincite. The mineral usually contains a certain amount of manganese and other elements and is of yellow to red colour. Due to its large band gap, pure ZnO is colourless and clear [1-3].

The possibility to grow epitaxial layers, quantum wells, nanorods and related objects or quantum dots and on, gave the hope to obtain:

(a) A material for blue/UV optoelectronics, including light-emitting or even laser diodes in addition to (or instead of) the GaN-based structures

(b) A radiation hard material for electronic devices in a corresponding environment

(c) A material for electronic circuits, which is transparent in the visible region

(d) A diluted or ferromagnetic material, when doped with Co, Mn, Fe, V or similar elements, for semiconductor spintronics

(e) A transparent, highly conducting oxide (TCO), when doped with Al, Ga, In or similar elements, as a cheaper alternative to indium tin oxide (ITO).

For several of the above-mentioned applications, a stable, high, and reproducible p-doping is obligatory. Progress has been made in this crucial field, which has been outlined below.

Crystal Structure and Chemical Binding of ZnO

Zinc oxide crystallises in the hexagonal wurtzite-type structure shown in Figure 2.1. It has a polar hexagonal axis, the c axis, chosen to be parallel to z. The point group is in the various notations 6 mm or C_{6v}, the space group $P6_3mc$ or C_{6v} [4]. One zinc ion is surrounded tetrahedrally by four oxygen ions and vice versa. The primitive unit cell contains two formula units of ZnO. The ratio c/a of the elementary translation vectors, with values around 1.60, deviates slightly from the ideal value c/a= 1.633. In contrast to other II^b–VI semiconductors, which exist both in the cubic zinc blende and the hexagonal wurtzite- type structures (like ZnS, which gave the name to both structures), ZnO crystallises with great preference in the wurtzite-type structure. The cubic zinc blende-type structure can, to some extent, be stabilized by epitaxial growth of ZnO on suitable cubic substrates, while the rock salt structure is stable only under pressure [3]. The tetrahedrally coordinated diamond, zinc blende, and wurtzite-type crystal structures are characteristic for covalent chemical bonding with sp^3 hybridisation. While the Group IV element semiconductors like diamond, silicon and germanium have completely covalent bonding, one has an increasing admixture of ionic binding when going from the Group IV over the III–V and II^b–VII to the I^b–VII semiconductors, ending with completely ionic binding for the II^a–VI and I^a–VII insulators like MgO or NaCl, which frequently crystallise in the rock salt structure[3].

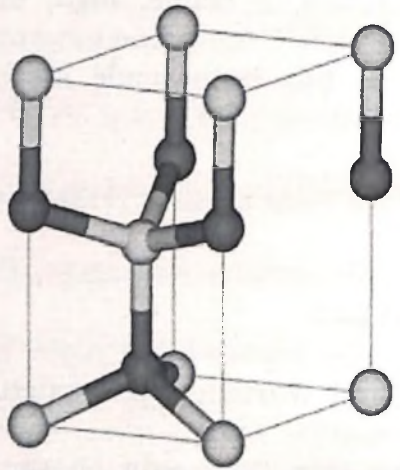
Figure 2.1 Unit cell of the crystal structure of ZnO . The light grey pheres corresponds to oxygen, the dark ones to zinc.

ZnO already has a substantial ionic bonding component, which shows ZnO in the "centre of solid state physics". Because of this fraction of ionic binding, the bottom of the conduction band, or the lowest unoccupied orbital (LUMO), is formed essentially from the 4s levels of Zn^{2+} and the top of the valence band, or highest occupied molecular orbital (HOMO), from the 2p levels of O^{2-}. The band gap between the conduction and valence bands is about 3.437 eV at low temperatures [3].

2.2 Scope of the present study

(a) Nanoparticles and Nanorods of Zinc oxide

Nanostructured ZnO materials have received broad attention due to their distinguished performance in electronics, optics and photonics. From the 1960's, synthesis of ZnO thin films has been an active field because of their applications as sensors, transducers and catalysts. In the last few decades, study of zero dimensional (0D) and one dimensional (1D) materials has become a leading edge in nanoscience and nanotechnology. With reduction in size, novel electrical, mechanical, chemical and optical properties are introduced, which are largely believed to be the result of surface and quantum confinement effects. Nanowire-like structures are the ideal system for studying the transport process in one-dimensionally (1D) confined objects, which are of benefit not only for understanding the fundamental phenomena in low dimensional systems, but also for developing new generation nanodevices with high performance [1,2].

Nanoparticles of ZnO have been prepared by both physical methods and soft chemical methods [3-9]. In example, ZnO nanoparticles have been prepared by the solvothermal route in the presence of various capping agents, using Zn^{2+}-cupferron complex as the precursor [5]. Precipitation of Zn^{2+} by OH^- ions in alcoholic solutions gives nanoparticles of ZnO [6], while precipitation through acid-catalyzed esterification of zinc acetate dihydrate with 1-pentanol at 130 °C also yields ZnO nanoparticles [7]. Decomposition of Zn(II)acetylacetonate in acetonitrile under solvothermal conditions at 100 °C gives ZnO nanoparticles [8]. Organic-capped ZnO nanocrystals have been prepared by injecting Zn/O precursors into trioctylphosphineoxide (TOPO) [9]. ZnO nanostructures are obtained by solvent evaporation from a reaction mixture containing an organozinc compound in tetrahydrofuran, the shape depending on the solvent, ligand and concentration [10]. Sol-gel process has also been employed by several workers to prepare ZnO nanoparticles [11-13]. This method involves the hydrolysis of zinc salts with strong bases in an alcoholic medium and the polycondensation of the metastable hydroxide into ZnO crystals.

A great deal of work has been carried out on 1-D ZnO nanostructures (nanorods and nanowires) due to their tunable electronic and optoelectronic properties [2, 14-18]. Some of the methods developed to produce ZnO nanorod arrays are chemical vapor deposition [19-20], physical vapor deposition [21-23], metal-organic vapor phase epitaxy [24], and use of anodic aluminum oxide templates [25-26]. Haidong et al. [27] developed a low-temperature chemical-liquid-deposition method to grow oriented ZnO nanorods by continuously supplying Zn ions from Zn foil to the ZnO-thin film coated substrate in aqueous formaldehyde solution. Reaction of a Zn^{2+} precursor with an organic base in alcohol/water solution gives 1-D nanostructures of ZnO [28]. Reaction of zinc acetate with NaOH in the presence of polyvinylpyrrolidone (PVP) at

80 °C in ethanol, under solvothermal conditions, gives ZnO nanorods [29]. Hydrothermal reactions have been used for the preparation of the ZnO nanorods as well. Thus, heating zinc nitrate hexahydrate and NaOH in a mixture of ethylenediamine and water at 180 °C for 20 h gives rise to thin (~50nm dia) ZnO nanorods [30]. In the presence of ethylenediamine, reaction of a Zn metal foil in water at 150-230 °C yields arrays of ZnO nanorods [31]

Generally, most of the above methods require relatively high temperatures or involve the use of expensive chemicals or apparatus. It is therefore of value to find simple methods to produce ZnO nanostructures employing inexpensive chemicals. A detailed study of the interaction of alcohols with Zn metal has shown that the C-O bond of the alcohol is readily cleaved on Zn metal surfaces giving hydrocarbons and the oxidic species on the metal surface [32, 33]. We therefore sought to examine the simple reaction of alcohols with Zn metal to find out whether we can obtain ZnO nanostructures by this means. Interestingly, we have found that ZnO nanoparticles are readily produced by the reaction of aliphatic alcohols at 330 °C in the absence of any surfactant. Addition of ethylenediamine to the alcohols gives rise to ZnO nanorods.

(b) Nitrogen-doped Zinc oxide nanorods

ZnO has a strong potential for various short-wavelength optoelectronic device applications. In order to attain the potential offered by ZnO, both high-quality *n*- and *p*-type ZnO are indispensable. ZnO with a wurtzite structure is naturally an *n*-type semiconductor because of a deviation from stoichiometry due to the presence of intrinsic defects such as oxygen vacancies (V*o*) and Zinc interstitials (Zn*i*). *n*-type doping of ZnO is relatively easy compared to *p*-type doping. Group-III elements Al, Ga, and In as substitutional elements for Zn and group-VII elements Cl and I as substitutional elements for O can be used as *n*-type dopants [34].

It is very difficult to obtain *p*-type doping in wide-band-gap semiconductors. The difficulties can arise from a variety of causes. Dopants may be compensated by low-energy native defects, such as Zn*i* or *Vo*, [35] or background impurities (H). Low solubility of the dopant in the host material is also another possibility [36]. Deep impurity level can also be a source of doping problem, causing significant resistance to the formation of shallow acceptor level.

Known acceptors in ZnO include group-I elements such as lithium [37-39], Na, and K, copper [40], silver [41], Zn vacancies, and group-V elements such as N, P, and As. However, many of these form deep acceptors and do not contribute significantly to *p*-type conduction. It has been believed that the most promising dopants for *p*-type ZnO are the group-V elements, although theory suggests some difficulty in achieving shallow acceptor level [42]. A number of theoretical studies have addressed the fundamental microscopic aspects of doping in wide band-gap semiconductors. The majority of these studies have dealt with the manner in which dopant solubility [43,44] or native defects [45,46] such as vacancies, interstitials, and antisites interfere with doping.

In ZnO, *p*-type doping may be possible by substituting either group-I elements (Li, Na, and K) for Zn sites or group-V elements (N, P, and As) for O sites. It was shown that group-I elements could be better *p*-type dopants than group-V elements in terms of shallowness of acceptor levels [42]. However, group-I elements tend to occupy the interstitial sites, in part mitigated by their small atomic radii, rather than substitutional sites, and therefore, act mainly as donors instead [47]. Moreover, significantly larger bond length for Na and K than ideal Zn–O bond length (1.93 Å) induces lattice strain, increasingly forming native defects such as vacancies which compensate the very dopants. These are among the many causes leading to difficulties in attaining *p*-type doping in ZnO. A similar behavior is observed for group-V elements except for N. Both P and As also have significantly larger bond lengths and, therefore, are more likely to form antisites to avoid the lattice strain. The antisites, A_{Zn}, are donorlike and provide yet another unwelcome possible mechanism for compensating acceptors. It then appears that perhaps the best candidate for *p*-type doping in ZnO is N because among the group-V impurities, N has the smallest ionization energy, it does not form the N_{Zn} antisite, and the *AX* center of N is only metastable [42].

In the literature, thin films of N-doped ZnO have been prepared by metal organic chemical vapor deposition (MOCVD) [48] or by the arc method [49]. In the MOCVD method, N-doped ZnO films were grown on a sapphire substrate in a horizontal MOCVD reactor by using dimethyl zinc, t-butanol and diallylamine as zinc, oxygen and nitrogen sources, respectively, with hydrogen as a carrier gas at a temperature between 420 and 480 °C. N-doped ZnO thin films have also been deposited on silicon or quartz substrates by the filtered cathodic vacuum arc method from a zinc target in an oxygen/nitrogen atmosphere at 350 °C at 10^{-4} Torr pressure. N-doped ZnO nanorods have been prepared recently by combining a wet-chemical process with post treatment by NH_3 plasma [50]. In this method, p-type Si (100) substrates are initially sputter-coated with a ZnO film and the film was placed in a glass bottle filled with 0.01 M aqueous solution of zinc(II)nitrate hexahydrate and hexamethylenetetramine (mole ratio, 1:1) at 75 °C for 10 h. The ZnO nanorods which formed perpendicular to the substrate were exposed to NH_3 plasma for different times to obtain N-doped ZnO nanorods. N-doped ZnO nanorods have also been prepared by the dc thermal plasma technique, wherein the Zn powder is fed into plasma flame generated by nitrogen and argon with air as the carrier gas [51].

We have found that nitrogen-doped ZnO nanorods can be conveniently prepared by the solvothermal reaction by adding liquid ammonia to a reaction mixture of zinc acetate with ethanol in the presence of ethylenediamine at 200 °C.

2.3 Experimental and related aspects

(a) Synthesis of ZnO nanoparticles

In a typical synthetic procedure for the nanoparticles, 10 mg of Zn metal powder (Ranbaxy; ~ 10 μm dia) was added to 10 ml of anhydrous alcohol (methanol, ethanol or *t*-butanol). The reaction mixture was sonicated for 10 minutes, transferred into a stainless steel autoclave (Swagelok) of 20 ml capacity and sealed under inert conditions inside a glove box. The reaction mixture was heated slowly (1 °C /min) to the 330 °C and maintained at this temperature for 18 hours. The resulting suspension was centrifuged to retrieve the product, washed with ethanol for three times and dried.

(b) Synthesis of ZnO nanorods

ZnO nanorods could be prepared by the addition of 1ml ethylenediamine to a mixture of 10 mg of Zn metal powder and 10 ml of the anhydrous alcohol (ethanol or *t*-butanol) and heating the mixture in a Swagelok autoclave (1 °C/min) to 330 °C. The reaction mixture was maintained at that temperature for 18 hours.

(c) Synthesis of nitrogen-doped ZnO nanorods

N-doped ZnO nanorods were prepared by the addition of 1ml of liquid ammonia to the reaction mixture of 300 mg zinc acetate, 6 ml ethylenediamine, 4 ml of ethanol taken in a teflon-lined autoclave, the autoclave was heated at 200 °C for 20 h. The resulting suspension were centrifuged to retrieve the product, washed with ethanol for three times and dried.

Techniques used for characterization

X-ray diffraction (XRD): X-ray diffraction (XRD) patterns of the samples were recorded in the θ-2θ Bragg-Bretano geometry with a Siemens D5005 diffractometer using Cu Kα (λ=0.151418 nm) radiation.

Scanning electron microscope (SEM): Scanning electron microscope images of the samples were recorded using a LEICA S440i scanning electron microscope.

Field emission scanning electron microscope (FESEM): FESEM images were recorded with a FEI NOVA NANOSEM 600.

UV-Vis absorption and Photoluminescence: UV-Vis absorption measurements were carried out at room temperature with a Perkin-Elmer model Lambda 900 UV/Vis/NIR spectrometer.

Photoluminescence (PL) measurements were carried out at room temperature with a Perkin-Elmer model LS50B luminescence spectrometer. The excitation wavelengths used depends on the samples studied. The samples were prepared by sonicating the product in CCl_4 to form dispersion.

Raman spectroscopy: Raman spectra were recorded with LabRAM HR high resolution Raman spectrometer (Horiba Jobin Yvon) using He-Ne Laser (λ=630 nm).

Transmission electron microscopy (TEM): Transmission electron microscope (TEM) images were obtained with a JEOL JEM 3010, operating with an accelerating voltage of 300 kV. The samples were prepared by dispersing the product in CCl_4. A drop of the suspension was then put on a holey carbon coated Cu grid and allowed to evaporate slowly.

2.4 Results and Discussion

(a) ZnO nanoparticles

In Figures 2.2 a and b, we show the low and high magnification FESEM images of the ZnO nanoparticles obtained by the reaction of Zn

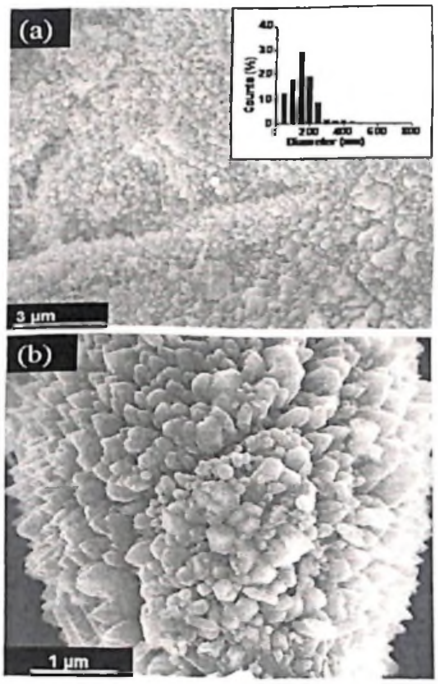

Fig. 2.2 Low (a) and high (b) magnification FESEM images of ZnO nanoparticles prepared at 330 °C by reaction with methanol. Inset in (a) shows the particle size distribution, histogram.

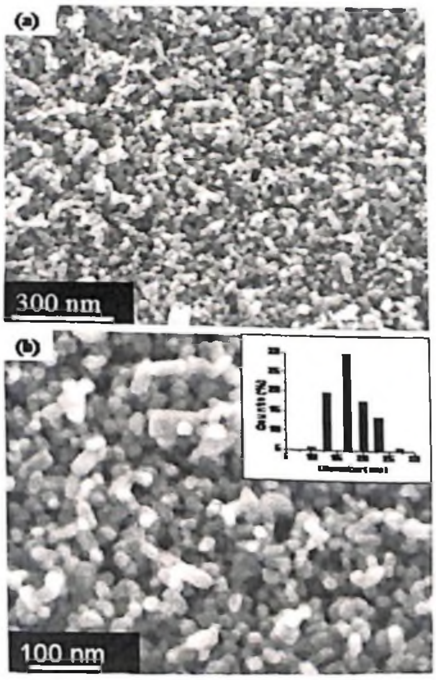

Fig. 2.3 Low (a) and high (b) magnification FESEM images of ZnO nanoparticles prepared at 330 °C by reaction with ethanol. Inset in (b) shows the particle size histogram.

metal powder with methanol under solvothermal conditions at 330 °C. The nanoparticles are not entirely spherical in shape and have diameters varying between 50 and 300 nm, with an average diameter of 150 nm as can be seen from the inset of Fig. 2.2 a. In Figures 2.3 a and b, we show the low and high magnification FESEM images of the ZnO nanoparticles prepared solvothermally at 330 °C by reaction with ethanol. The images reveal short rod-like ZnO nanoparticles with an average diameter of 17 nm and average length of 35 nm (see inset of Fig. 2.3b). Thus, the average particle size of the ZnO nanoparticles obtained from the reaction with ethanol is smaller than that obtained with methanol. In Fig. 2.4a, we show a TEM image of the ZnO nanoparticles prepared by using ethanol. The diameter of the ZnO nanoparticles ranges from 10-40 nm,

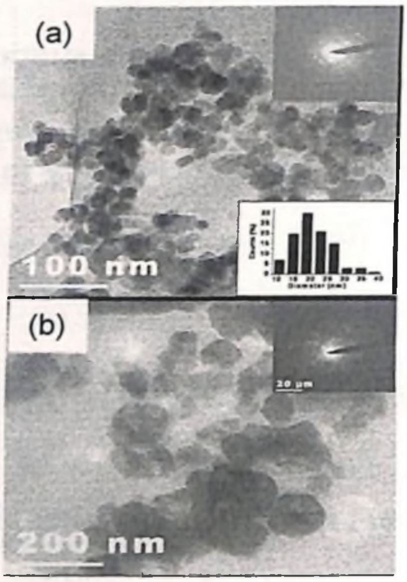

Fig. 2.4 TEM images of ZnO nanoparticles prepared at 330 °C by reaction with (a) ethanol and (b) t-butanol. Insets at the top right hand sides of (a) and (b) show the ED patterns. Inset in the bottom right hand side in (a) shows the particle size distribution, histogram.

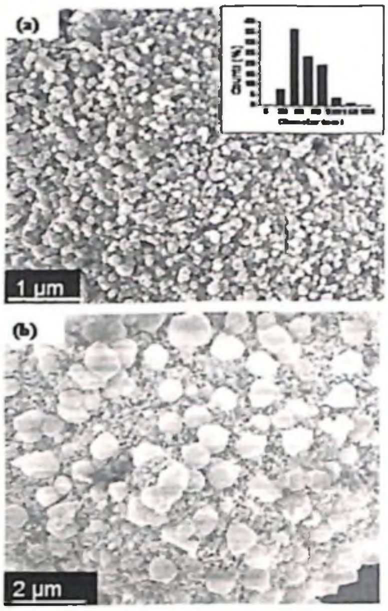

Fig. 2.5 High (a) and low (b) magnification FESEM images of ZnO nanoparticles prepared at 330 °C by reaction with t-butanol. Inset in (a) shows the particle size distribution, histogram.

with an average value of 17 nm as seen from the inset in Fig. 2.4a. The selected area electron diffraction pattern shown as an inset in Fig. 2.4a confirms the crystalline nature of the ZnO nanoparticles.

In Figures 2.5 a and b, we show the high and low magnification FESEM images of the ZnO nanoparticles obtained by the reaction of Zn powder with *t*-butanol at 330 °C. The nanoparticles are nearly spherical in shape with variable size in the 20-180 nm range. The average diameter of the particles is 50 nm. In some regions we notice that big nanoparticles (average diameter ~ 650 nm) are surrounded by smaller nanoparticles (average diameter ~ 50 nm) as shown in Fig. 2.5b. In Fig. 2.4b, we show a TEM image of the ZnO nanoparticles obtained with *t*-butanol. The diameter of the ZnO nanoparticles ranges from 40 to 100 nm. The selected area electron diffraction pattern shown in the inset of Fig. 2.4b confirms the crystalline nature of the ZnO nanoparticles. We have also observed the presence of short nanorods (average diameter ~ 125 nm with the length varying form 400 nm to 700 nm) occasionally in the TEM images.

(b) ZnO Nanorods

Addition of 1 ml of ethylenediamine to the reaction mixture of zinc metal powder and alcohol gives ZnO nanorods. In Figures 2.6 a and b, we show the FESEM images of the ZnO nanorods obtained by the addition of ethylenediamine to ethanol and *t*-butanol respectively. The nanorods obtained with ethanol have an average diameter of 250 nm and lengths up to several micrometers. We also observe the occurrence of smaller ZnO nanorods with an average diameter of 9 nm and average length of 150 nm (see inset of Fig. 2.6a). The nanorods obtained with *t*-butanol have diameters ranging from 25 to 120 nm with lengths going up to 1-2 µm. The effect of addition of ethylenediamine to the alcohols suggests the shape-directing effect of the amine in agreements with the literature [30,31] .

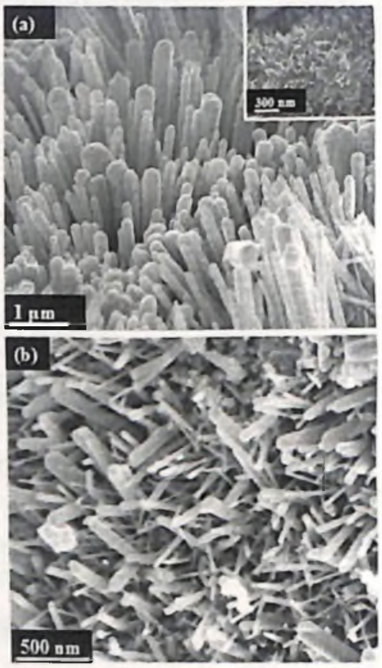

Fig. 2.6 FESEM images of ZnO nanorods prepared at 330 °C by the addition of 1 ml of ethylenediamine to the reaction mixture containing (a) ethanol and (b) t-butanol.

The XRD patterns of the ZnO nanoparticles and nanorods could be indexed to the hexagonal wurtzite structure (space group: $P6_3mc$; a = 0.3249 nm, c =0.5206 nm, JCPDS card no. 36-1451). The UV absorption spectrum of the ZnO nanoparticles gives a band around 375 nm as shown in Fig. 2.7a. The spectrum shows well-defined exciton absorption peaks characteristic of ZnO, with a significant blue shift compared to bulk ZnO [52]. The room-temperature PL spectrum of the ZnO nanoparticles (Fig. 2.7b) shows a UV emission at 380 nm and broad bands centered at 424 nm, 445 nm, 485 nm and 528nm. The UV emission corresponds to exciton recombination related near-band edge

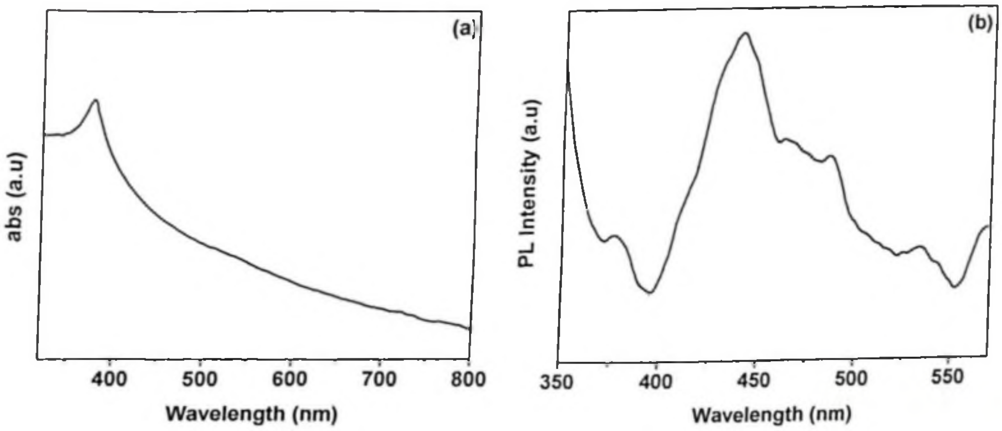

Fig. 2.7. (a) Typically UV-Vis spectrum of ZnO nanoparticles. (b) Photoluminescence spectrum of ZnO nanoparticles.

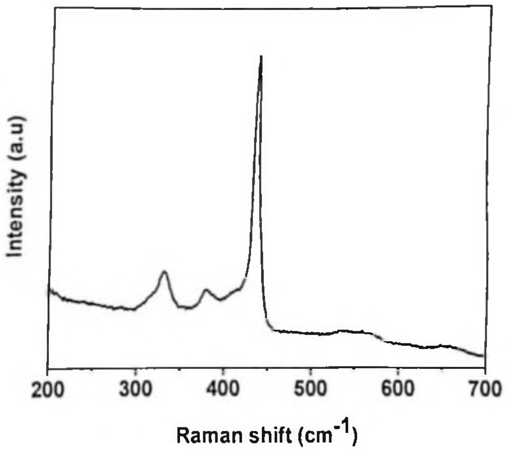

Fig. 2.8 Raman spectrum of ZnO nanoparticles.

emission [53] and the deep-level visible emission originates from the localized levels in the band gap [31]. The visible emission is considered to originate from the electron transition from a singly ionized oxygen vacancy to the photoexcited hole [54]. ZnO nanoparticles exhibit Raman bands at 331, 378, 436 cm^{-1} (Fig. 2.8). The bands at 436 and 378 cm^{-1} are attributed to E_2 (high) mode and A1 (TO) modes respectively and the band at 331 cm^{-1} could arise from a multiphonon process [53].

The following scheme describes the sequence of events in the reaction of alcohols (ROH, R=CH_3, C_2H_5 and t-C_4H_9) with zinc.

$$Zn(s) + ROH \longrightarrow Zn + ROH(a)$$

$$ROH(a) \longrightarrow RO(a) + H(a)$$

$$2RO(a) \longrightarrow 2O(a) + R_2(g)$$

$$O(a) + 2e^- \longrightarrow O^{2-}(s)$$

Here (s), (a) and (g) represents solid, adsorbed species and gas respectively. O(a) is adsorbed on Zn later forming ZnO.

(c) Nitrogen-doped ZnO nanorods

By adding a small amount of liquid ammonia to the reaction mixture of zinc(II)acetate, ethylenediamine, ethanol and carrying out the reaction at 200 °C at a slow heating rate of 1 °C/min, we obtained hemispherical agglomerates of N-doped ZnO rods as revealed by the SEM image in Fig. 2.9a. We also find randomly distributed nanorods with diameters in the range 300 nm to 2 μm and length around 20 μm as shown in Fig. 2.9b. The XRD pattern of the N-doped ZnO nanorods was close to that of the ZnO nanorods. The UV–Vis absorption spectrum (Fig. 2.10) showed a band at 352 nm, with increasing featureless absorption with increasing wavelength in the 400–1500 nm region. In this region, ZnO nanorods show decrease in absorption with increasing wavelength. The Raman spectrum of N-doped ZnO nanorods is significantly different from that of ZnO nanorods as can be seen from Fig. 2.11. We observe four additional bands at 275, 507, 579 and 642 cm^{-1}. These modes correspond to the silent modes of wurtzite-ZnO and arise from the breakdown of the translational crystal symmetry induced by defects and impurities [55].

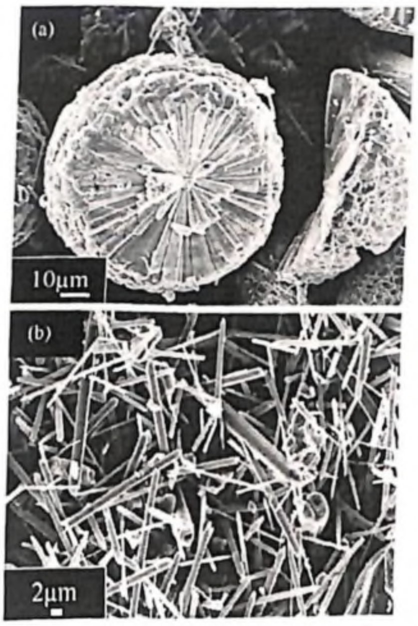

Fig. 2.9 (a and b) SEM images of N-doped ZnO nanorods.

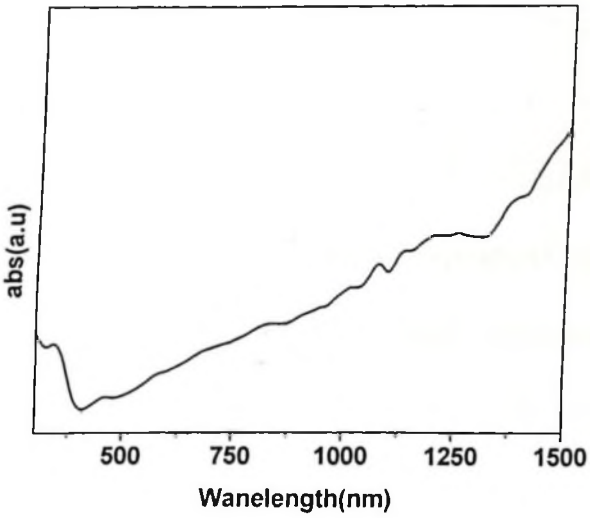

Fig. 2.10 UV-Vis absorption spectra of N-ZnO nanorods

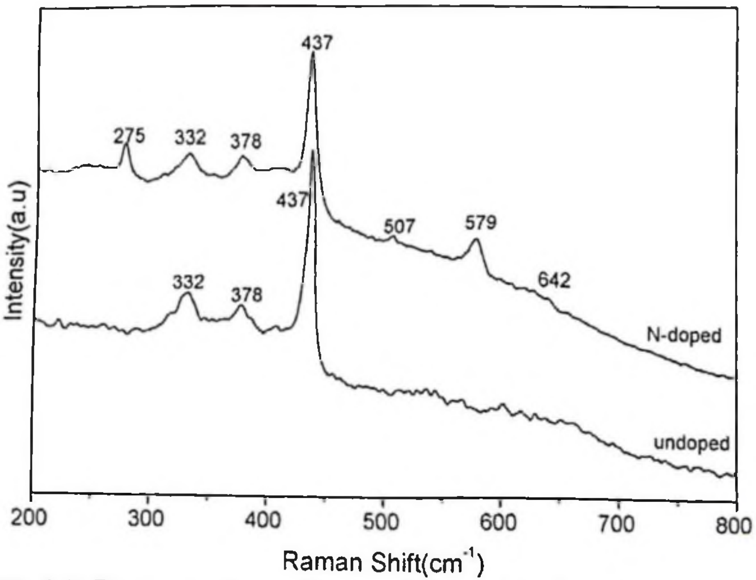

Fig. 2.11 Raman spectrum of pure and N-doped ZnO nanorods.

Photoluminescence spectra of ZnO and N-doped ZnO nanorods show significant differences as can be seen from Fig. 2.12. The spectrum of the ZnO nanorods (Fig. 2.12a) shows a strong UV emission at 384 nm and weaker bands in the 400–550 nm region. The bands are red-shifted in the PL spectrum of N-doped ZnO nanorods (Fig. 2.12b) and we observe bands centered at 407 nm, 432 nm, 456 nm in addition to a small band centered at 815 nm. The intensity of the 432 nm band is higher than that of 407 nm. On heating the sample at 950 °C for 10 h in oxygen, the intensity of the 407 nm band dominates (see inset of Fig. 2.12b). All spectroscopic features of N-doped ZnO nanorods are compared here with undoped ZnO nanorods, which are prepared at similar conditions with out adding ammonia to the reaction mixture.

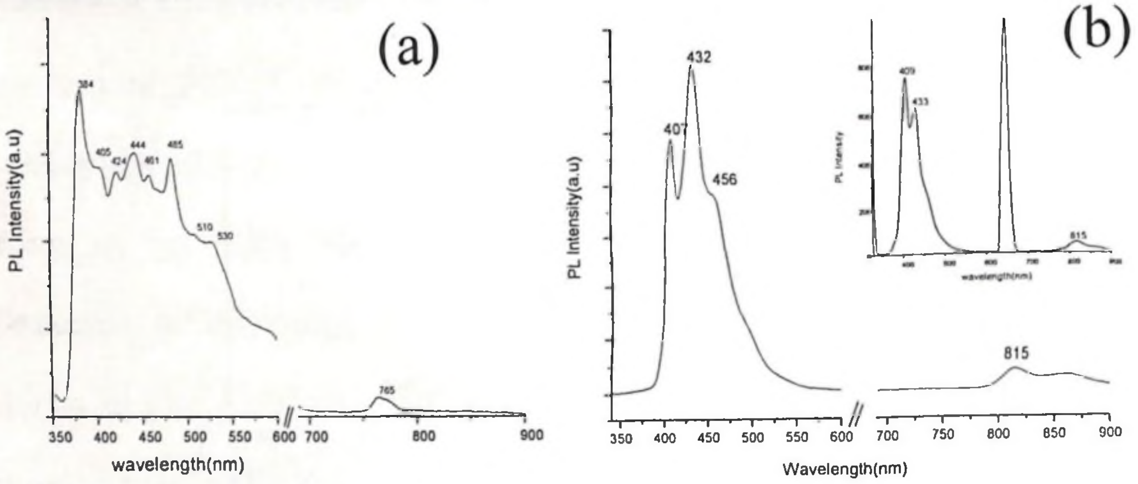

Fig. 2.12 Photoluminescence spectra of (a) ZnO nanorods and (b) N-doped ZnO nanorods. Inset in (b) N-doped ZnO nanorods after annealing at 950 °C in oxygen.

2.5 Conclusions

Solvothermal reaction of aliphatic alcohols such as methanol, ethanol and *t*-butanol with zinc powder provides a simple procedure to produce nanoparticles of ZnO. This is in accordance with the finding that the C-O bond of alcohols is readily cleaved by Zn metal [32, 33]. Addition of ethylenediamine to the reaction mixture helps to obtain ZnO nanorods. By taking a small amount of liquid NH_3 in the reaction mixture of zinc acetate, etylenediamine and ethanol, N-doped ZnO nanorods are obtained under solvothermal conditions. N-doped ZnO nanorods exhibit different spectroscopic properties from those of pure ZnO nanorods.

References

1. Z. L. Wang, *Mater. Today* **2004**, *7*, 26.
2. C. N. R. Rao and A. Govindaraj (2005) *"Nanotubes and Nanowires", The RSC Nanoscience & Nanotechnology series*, (Eds. H. Kroto, P. O'Brien, H. Craighead) Royal Society of Chemistry (London).
3. C. Klingshirn, *Chem. Phys. Chem.* **2007**, *8*, 782.
4. (a) H. Usui, Y. Shimizu, T. Sasaki, and N. Koshizaki, *J. Phys. Chem. B* **2005**, *109,* 120. (b) E. M. Wong and P. C. Searson, *Appl. Phys. Lett.* **1999**, *74,* 2939.
5. M. Ghosh, R. Seshadri and C. N. R. Rao *J. Nanosci. Nanotechnol.* **2004**, *4*, 136.

U. Koch, A. Fojtik, H. Weller and A. Henglein *Chem. Phys. Lett.* **1985**, *122*, 507.

7 M. M. Demir, R. Muñoz-Espí, I. Lieberwirth and G. Wegner, J. *Mater. Chem.* **2006**, *16*, 2940.

8 J. Buha, I. Djerdj, M. Niederberger, *Crystal Growth & Design* **2007**, *7*, 113.

9 M. Shim and P. Guyot-Sionnest, *J. Am. Chem. Soc.* **2001**, *123,* 11651.

10 M. Monge, M. L. Kahn, A. Maisonnat, B. Chaudret, *Angew.Chem. Int. Ed.* **2003,** *42*, 5321.

11 L. Spanhel and M. A. Anderson, *J. Am. Chem. Soc.* **1991**, *113,* 2826.

12 M. S. Tokumoto, S. H. Pulcinelli, C. V. Santilli and V. Briois, J. Phys. Chem. B, **2003**, *107*, 568.

13 B. J. Joo, S. G. Kwon, J. H. Yu, T. Hyeon, *Adv. Mater.* **2005**, *17*, 1873.

14 Z. R. Qiu, K. S. Wong, M. M. Wu, W. J. Lin, H. F. Xu, Appl. Phys.Lett. **2004**, *84*, 2739.

15 B. P. Zhang, N. T. Binh, Y. Segawa, Y. Kashiwaba, K. Haga, Appl. Phys. Lett. **2004**, *84*, 586.

16 S. F. Yu, C. Yuen, S. P. Lau, W. I. Park, G. C. Yi, Appl. Phys. Lett. **2004**, *84*, 3241.

17 Q. X. Zhao, M. Willander, R. E. Morjan, Q. H. Hu, E. E. B. Campbell, Appl. Phys. Lett. **2003**, *83*, 165.

18 C. J. Lee, T. J. Lee, S. C. Lyu, Y. Zhang, H. Ruh, H. J. Lee, Appl. Phys. Lett. **2002**, *81*, 3648.

19 J. J. Wu, S. C. Liu, Adv. Mater. **2002**, *14*, 215.

20 X. Liu, X. H. Wu, H. Cao, R. P. H. Chang, J. Appl. Phys. **2004**, *95*, 3141.

21 Y. Zhang, H. B. Jia, R. M. Wang, C. P. Chen, X. H. Luo, D. P. Yu, C. J. Lee, Appl. Phys. Lett. **2003**, *83*, 4631.

22 Y. C. Kong, D. P. Yu, B. Zhang, W. Fang, S. Q. Feng, Appl. Phys. Lett. **2001**, *78*, 407.

23 S. C. Lyu, Y. Zhang, C. J. Lee, H. Ruh, H. J. Lee, Chem. Mater. **2003**, *15*, 3294.

24 W. I. Park, D. H. Kim, S. W. Jung, G. C. Yi, Appl. Phys. Lett. **2002**, *80*, 4232.

25 Y. Li, G. W. Meng, L. D. Zhang, F. Phillipp, Appl. Phys. Lett. **2000**, *76*, 2011.

26 C. Liu, J. A. Zapien, Y. Yao, X. Meng, C. S. Lee, S. Fan, Y. Lifshitz, S. T. Lee, Adv. Mater. **2003**, *15*, 838.

27 H. Yu, Z. Zhang, M. Han, X. Hao, F. Zhu, *J. Am. Chem. Soc.* **2005**, *127*, 2378.

28 B. Cheng, W. S. Shi, J. M. Russell-Tanner, L. Zhang, E. T. Samulski, *Inorg. Chem.* **2006**, *45*, 1208.

29 C. Wang , E. Shen, E. Wang, L. Gao, Z. Kang, C. Tian, Y. Lan, C. Zhang , Mater. Lett. **2005**, *59*, 2867.

30 B. Liu, H . C. Zeng, J. Am. Chem. Soc. **2003**, *125*, 4430.

31 A. Dev, S. Kar, S. Chakrabarti, S. Chaudhuri, Nanotechnology **2006**, *17*, 1533.

32 K. R. Harikumar, C. P. Vinod, G. U. Kulkarni, C. N. R. Rao, *J. Phys. Chem. B* **1999**, *103*, 2445.

33 K. R. Harikumar and C. N. R. Rao, *Chem. Commun.* **1999**, 341.

34 H. Kato, M. Sano, K. Miyamoto, and T. Yao, J. Cryst. Growth **2002**, *237- 239*, 538.

35 W. Walukiewicz, Phys. Rev. B **1994**, *50*, 5221.

36 C. G. Van de Walle, D. B. Laks, G. F. Neumark, and S. T. Pantelides, Phys. Rev. B **1993**, *47*, 9425.

37 F. Schirmer and D. Zwingel, Solid State Commun. **1970**, *8*, 1559.

38 F. Schirmer, J. Phys. Chem. Solids **1968**, *29*, 1407.

39 A. Valentini, F. Quaranta, M. Rossi, and G. Battaglin, J. Vac. Sci. Technol. A **1991**, *9*, 286.

40 Y. Kanai, Jpn. J. Appl. Phys., Part 1 **1991**, *30*, 703.

41 Y. Kanai, Jpn. J. Appl. Phys., Part 1 **1991**, *30*, 2021.

42 C. H. Park, S. B. Zhang, and S.-H. Wei, Phys. Rev. B **2002**, *66*, 073202.

43 D. C. Reynolds, D. C. Look, B. Jogai, and T. C. Collins, Appl. Phys. Lett. **2001**, *79*, 3794.

44 C. G. Van de Walle, D. B. Laks, G. F. Neumark, and S. T. Pantelides, Phys. Rev. B **1993**, *47*, 9425.

45 D. B. Laks, C. G. Van de Walle, G. F. Neumark, and S. T. Pantelides, Phys. Rev. Lett. **1991**, *66*, 648.

46 A. Garcia and J. E. Northrup, Phys. Rev. Lett. **1995**, *74*, 1131.

47 D. C. Look, R. L. Jones, J. R. Sizelove, N. Y. Garces, N. C. Giles, and L. E. Halliburton, Phys. Status Solidi A **2004**, *195*, 171.

48 N. H. Nickel and F. Friedrich, J. F. Rommeluère and P. Galtier, Appl. Phys. Lett. **2005**, *87*, 211905-1.

49 Y. G. Wang, S. P. Lau, X. H. Zhang, H. W. Lee, H. H. Hng and B. K. Tay, J. Crystal Growth **2003**, *252*, 265.

50 C. C. Lin, H. P. Chen and S. Y. Chen, Chem. Phys. Lett. **2005**, *404*, 30.

51 C. Liao, H. F. Lin, S. W. Hung and C. T. Hu, J. Vac. Sci. Technol. B **2006**, *24*, 1322.

52 N. S. Pesika, K. J. Stebe and P. C. Searson, *J. Phys. Chem. B* **2003,** *107*, 10412.

53 X.Q. Meng, D.Z. Shen, J.Y. Zhang, D.X. Zhao, Y.M. Lu, L. Dong, Z.Z. Zhang, Y.C. Liu and X.W. Fan *Solid State Commun.* **2005**, *135*, 179.

54 K. Vanheusden, W. L. Warren, C. H. Seager, D. R. Tallant, J. A. Voigt, and B. E. Gnade *J. Appl. Phys.* **1996**, *79*, 7983.

55 F. J. Manjon, B. Mari, J. Serrano and A. H. Romero, J. Appl. Phys. **2005**, *97*, 053516.

Chapter 3

A Simple Method to Prepare ZnO and $Al(OH)_3$ Nanorods by the Reaction of the Metals with Liquid Water*

Summary

Reaction of liquid water with Zn and Al powders and foils have been investigated in the 25–75 °C range. The reaction of Zn metal powder with water in this temperature range yields ZnO nanorods. The diameter of the nanorods decreases slightly with the increase in the reaction temperature, accompanied by an increase in the relative intensity of UV emission band. Zn metal foils also yield ZnO nanorods on reaction with water in the 25–75 °C range. Reaction of Al metal powder or foil with water in the 25–75 °C range yields $Al(OH)_3$ nanorods. The formation of ZnO and $Al(OH)_3$ nanorods by the reaction of the metals with water is suggested to occur because of the decomposition of water by the metal giving hydrogen.

---

*Paper based on these studies has been published in J. Solid State Chem., 2007,180 (11), 3106-3110.

3.1 Introduction

Zinc oxide is an important solid state material of contemporary interest, possessing several properties such as piezoelectricity, field emission and lasing action with potential technological applications [1,2]. One-dimensional (1D) nanostructures of ZnO have been of particular interest due to their tunable electronic and optoelectronic properties [1–7]. The methods employed to produce ZnO nanorods include chemical vapor deposition [8,9], physical vapor deposition [10–12], metal-organic vapor phase epitaxy [13] and the use of anodic aluminum oxide templates [14,15]. A low-temperature chemical-liquid deposition method has been employed to grow oriented ZnO nanorods by continuously supplying Zn ions from a Zn foil to a ZnO-coated substrate in aqueous formaldehyde solution [16]. Reaction of a Zn^{2+} salt with ethyl alcohol in the presence of an amine gives 1D nanostructures of ZnO [17]. Solvothermal reaction of zinc acetate with NaOH in the presence of polyvinylpyrolidone in ethanol has been employed to obtain ZnO nanorods [18]. Hydrothermal reactions have been used for the preparation of the ZnO nanorods as well. Thus, heating zinc nitrate and NaOH in a mixture of ethylenediamine and water at 180 °C for 20 h gives rise to ZnO nanorods [19]. In the presence of ethylenediamine, the reaction of Zn metal foil with water under hydrothermal conditions (150–230 °C) is also reported to yield ZnO nanorods [20].

3.2 Scope of the present study

It has been found recently that the C–O bond of the aliphatic alcohols is readily cleaved on zinc metal surfaces, giving rise to ZnO nanoparticles [21], which has been described in previous chapter. It occurred to us that the reaction of Zn metal with liquid water may also produce ZnO nanostuctures, since the reaction would be associated with the evolution of hydrogen [22,23]. We have, therefore, investigated the reaction of Zn metal powder and Zn foils with water at room temperature as well as with water maintained at a temperature in the 25–75 °C range. Here, we have examined the interaction of zinc metal with liquid water at or close to room temperature with out any additives. The literature methods generally use amines and other additives or zinc compounds and employ higher temperatures. Encouraged by the results obtained by the reaction Zn metal with water, we have also examined the reaction of aluminum metal with water. The present study provides a very simple method of generating nanorods of ZnO and $Al(OH)_3$ by the reaction of liquid water with the metals.

3.3 Experimental and related aspects

(a) Synthesis of ZnO nanorods

In a typical synthesis of the ZnO nanorods from Zn metal powder (Ranbaxy, ≥10 μm diameter), 10 mg of Zn the powder was taken in a vial containing 10 ml of double distilled water (pH 6.5). The reaction mixture was kept at a desired temperature. At 25 °C (room temperature), the reaction mixture was kept for 72 h. Reaction of zinc foils with double distilled water carried out by immersion the foil in 10 ml of water and maintained the temperature at desired value at 25 °C for 72 h. At 50 and 75 °C, the reaction mixture was kept for 24 h. The $Zn+H_2O$ reaction was also carried out at 25 °C by adding ethylenediamine (1 ml) to 10 ml of water.

(b) Synthesis of $Al(OH)_3$ nanorods

In a typical synthesis, 10 mg of Al metal powder (Ranbaxy, ≥10 µm diameter), was taken in a vial containing 10 ml of double distilled water (pH 6.5). The reaction mixture was kept at a desired temperature at 25 °C (room temperature), the reaction mixture was kept for 120 h. Reaction of Al foils with double distilled water carried out by immersion of the foil in 10 ml of water and maintained the temperature at desired value at 25 °C for 120 h. At 50 and 75 °C, the reaction mixture was kept for 24 h.

Techniques used for characterization

X-ray diffraction (XRD): X-ray diffraction (XRD) patterns of the samples were recorded in the θ-2θ Bragg-Bretano geometry with a Siemens D5005 diffractometer using Cu Kα (λ=0.151418 nm) radiation.

Field emission scanning electron microscope (FESEM): FESEM images were recorded with a FEI NOVA NANOSEM 600.

UV-Vis absorption and Photoluminescence: UV-Vis absorption measurements were carried out at room temperature with a Perkin-Elmer model Lambda 900 UV/Vis/NIR spectrometer.

Photoluminescence (PL) measurements were carried out at room temperature with a Perkin-Elmer model LS50B luminescence spectrometer. The excitation wavelengths used depends on the samples studied. The samples were prepared by sonicating the product in CCl_4 to form dispersion.

Raman spectroscopy: Raman spectra were recorded with LabRAM HR high resolution Raman spectrometer (Horiba Jobin Yvon) using He-Ne Laser (λ=630 nm).

Infrared spectroscopy (IR): IR spectra were recorded on KBr pellet with Bruker IFS-66V.

Transmission electron microscopy (TEM): Transmission electron microscope (TEM) images were obtained with a JEOL JEM 3010, operating with an accelerating voltage of 300 kV. The samples were prepared by dispersing the product in CCl_4. A drop of the suspension was then put on a holey carbon coated Cu grid and allowed to evaporate slowly.

3.4 Results and discussion

(a) ZnO nanorods

In Figs. 3.1-3.3, we show FESEM images of ZnO nanorods obtained by the reaction of Zn metal powder with water at different temperatures. Of these, Figs. 3.1 a, b show FESEM images of the

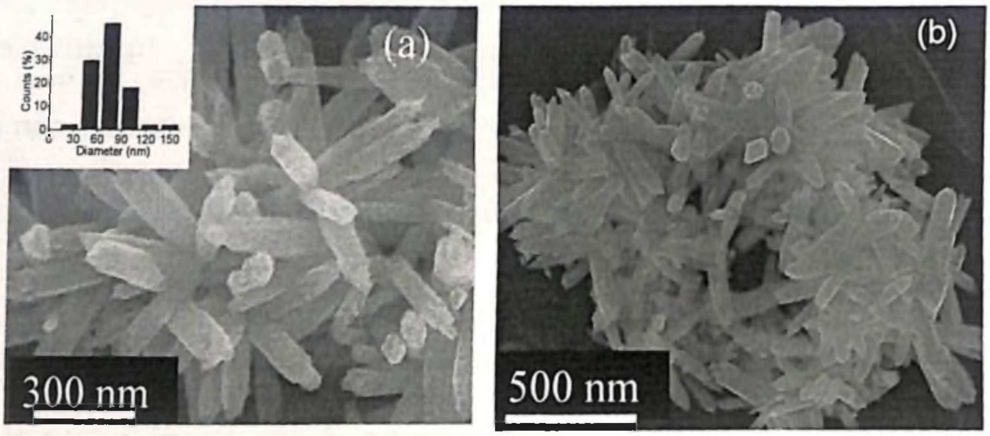

Fig. 3.1 high (a) and low (b) magnification FESEM images of ZnO nanorods prepared at 25 °C by the reaction of Zn metal with water. Inset in (a) shows a diameter distribution, histogram.

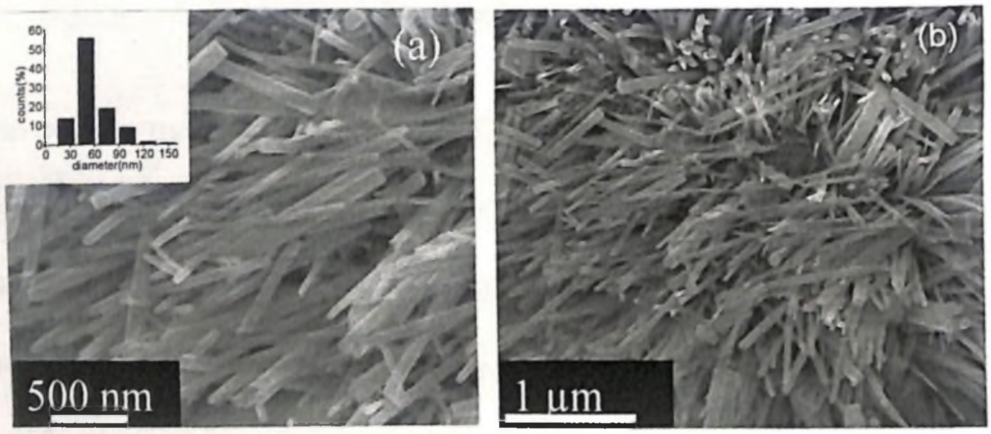

Fig. 3.2 high (a) and low (b) magnification FESEM images of ZnO nanorods prepared at 50 °C by the reaction of Zn metal with water. Inset in (a) shows a diameter distribution, histogram.

nanorods obtained after the reaction at 25 °C for 72 h. The nanorods have diameters varying between 40 and 150 nm, with an average diameter of around 75 nm, and an average length of 300 nm (see inset in Fig. 3.1a). FESEM images of the ZnO nanorods obtained after reaction at 50 °C for 24 h are shown in Fig. 3.2. These nanorods have diameters in the range 20–100 nm, with an average diameter of 50 nm and the length ranging from 1 to 3 μm (see inset in Fig. 3.2a). The nanorods prepared at 75 °C have diameters in the 20–140 nm range, with an average diameter

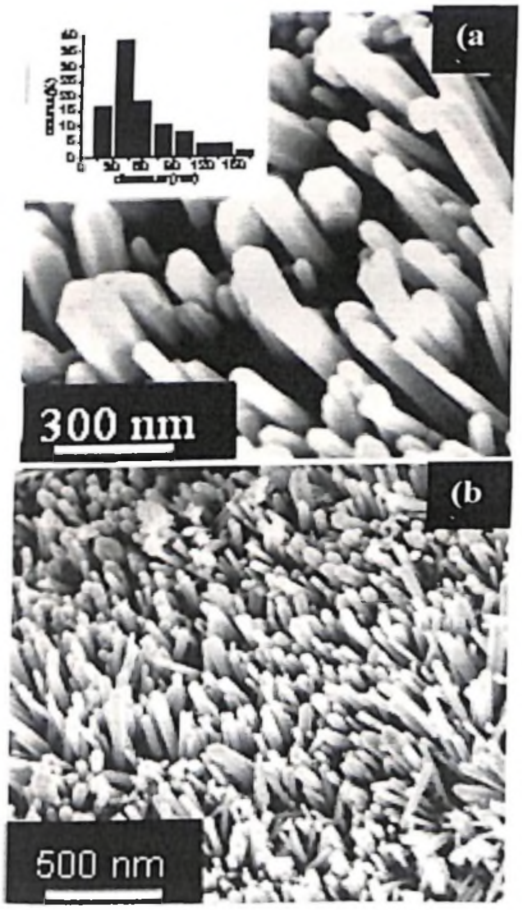

Fig. 3.3 high (a) and low (b) magnification FESEM images of ZnO nanorods prepared by 75 °C by reaction of Zn metal with water. Inset in (a) shows the diameter distribution, histogram

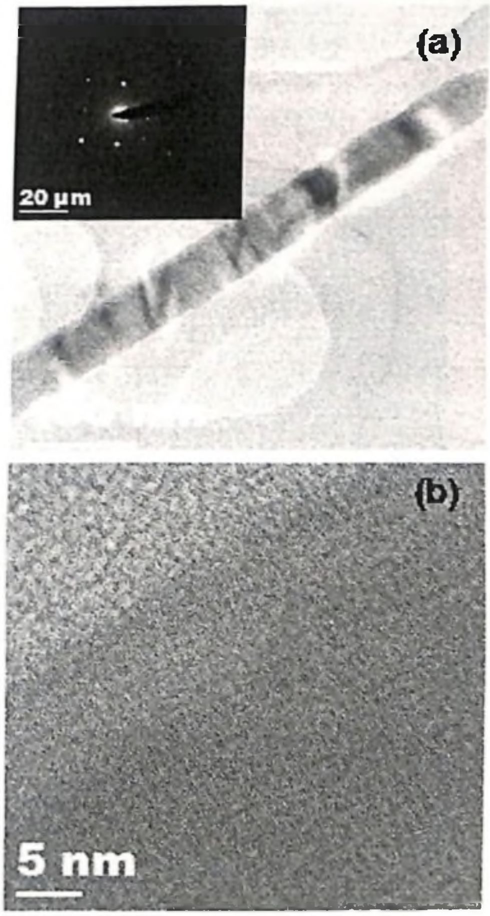

Fig. 3.4 TEM (a) and HREM (b) images of ZnO nanorods prepared at 50 °C by reaction of Zn metal with water. Inset in (a) shows the SAED pattern

of 40 nm and the length in the 1–3 μm range (Fig. 3.3). Inset in Fig. 3.3a shows the particle size distribution, histogram. In Fig. 3.4, we show TEM images of a ZnO nanorod (diameter~40 nm) prepared at 50 °C. The selected area electron diffraction (SAED) pattern shown as an inset in Fig. 3.4a and high resolution TEM image in Fig. 3.4b confirm the single crystalline nature of the nanorod. The XRD patterns of the ZnO nanorods (Fig. 3.5) obtained from the different preparations could be indexed on the hexagonal wurtzite structure (space group: $P6_3mc$; a = 0.3249 nm, c = 0.5206 nm, JCPDS card no. 36-1451). Our studies of the reaction of Zn powder with liquid water in the 25–75 °C range indicate that the average diameter of the ZnO nanorods decreases with the increase in temperature, accompanied by an increase in the aspect ratio. We have examined the effect of addition of ethylenediamine on the formation of ZnO nanorods by the reaction of water with Zn metal powder. By adding

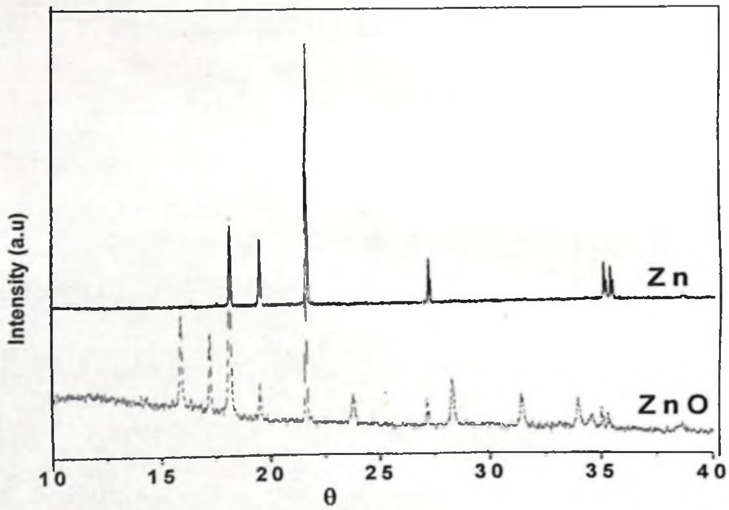

Fig. 3.5 XRD patterns of ZnO nanorods along with the starting metal sample

1 ml of ethylenediamine to 10 ml of water, we found that the reaction occurs faster. Thus, at 25 °C, ZnO nanorods were produced (Fig. 3.6) just after 36 h. The diameter of the nanorods was, however, a little larger.

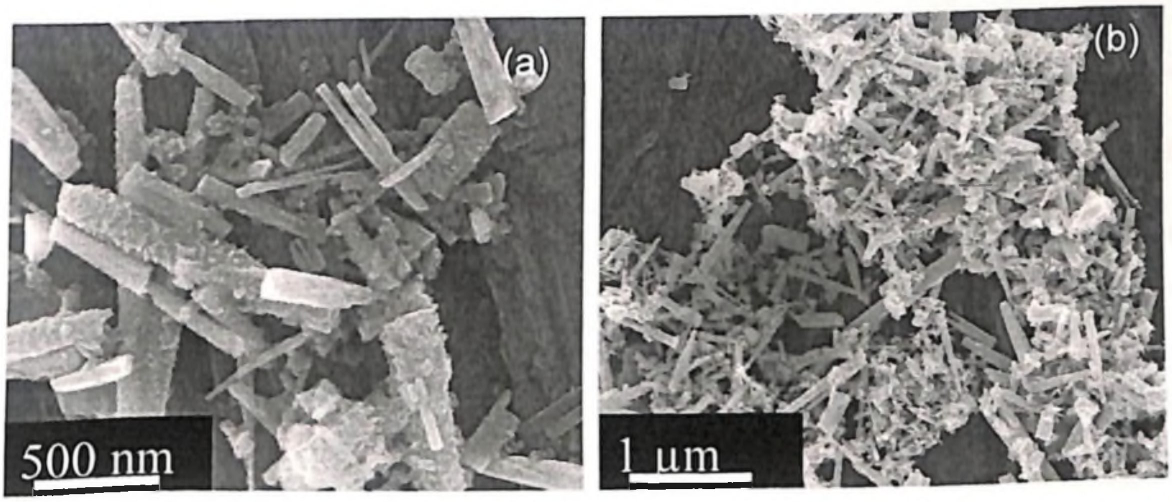

Fig. 3.6 high (a) and low (b) magnification FESEM images of ZnO nanorods prepared at 25 °C by the reaction of Zn metal with water by adding 1 ml ethylenediamine

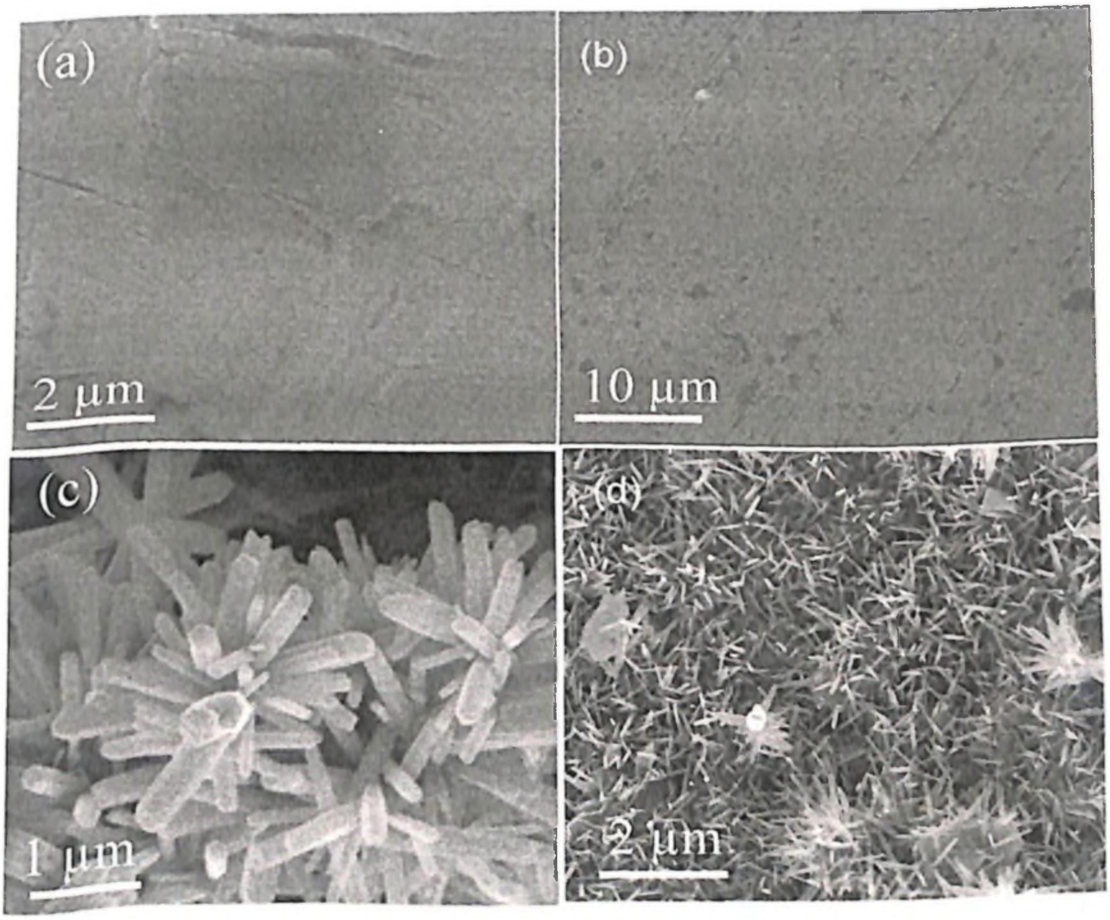

Fig. 3.7 FESEM images of Zn foil (a and b) and of ZnO nanorods (c and d) obtained at 50 °C by the reaction of water with the Zn foil.

In Fig. 3.7 a and b, we show the FESEM image of a Zn foil. In Fig. 3.7 c and d, we show a FESEM image of ZnO nanorods obtained by the reaction of the Zn foil with water at 50 °C. The diameter of the nanorods varies between 80 and 400 nm, with an average value of 150 nm. The average length of the nanorods is 1 µm. The XRD pattern of these nanorods was also characteristic of the wurtzite structure.

The UV-Vis absorption spectrum of the ZnO nanorods gives the characteristic band round 365 nm (see Fig. 3.8a) [24]. The room-temperature PL spectra of the ZnO nanorods (Fig. 3.8b) show a UV emission band at 380 nm due to the radiative recombination between the electrons in the conduction band and the holes in the valence band [20,25], and broad bands in the 420–530 nm range. The visible emission originates from the localized levels in the band gap [20]. The UV emission band is present prominently in the sample prepared at 75 °C, but is

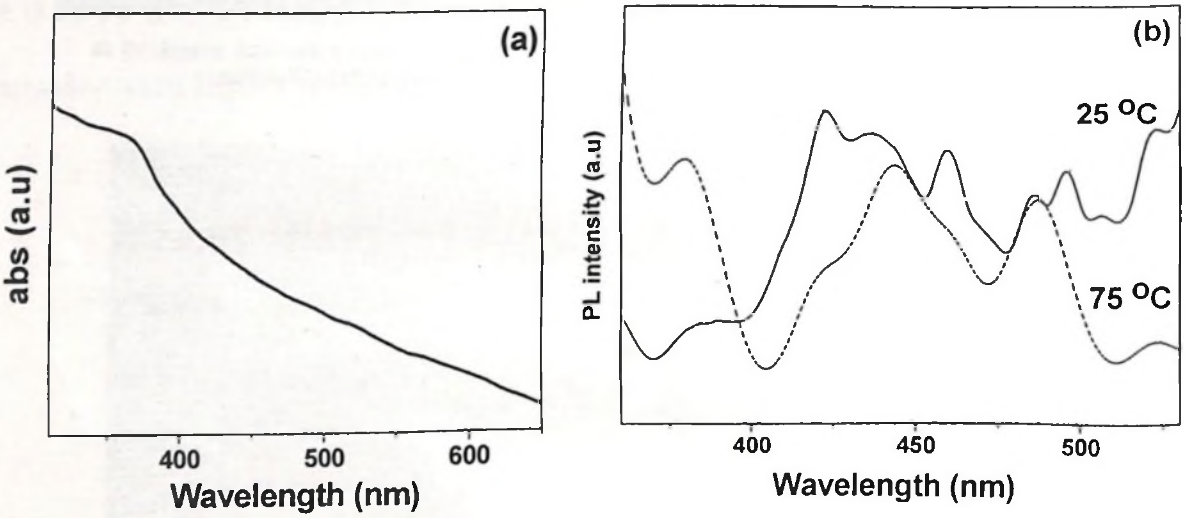

Fig. 3.8 (a) Typical UV-Vis spectrum of ZnO nnaorods (b) PL spectra of ZnO nanorods obtained at 25 °C and 75 °C

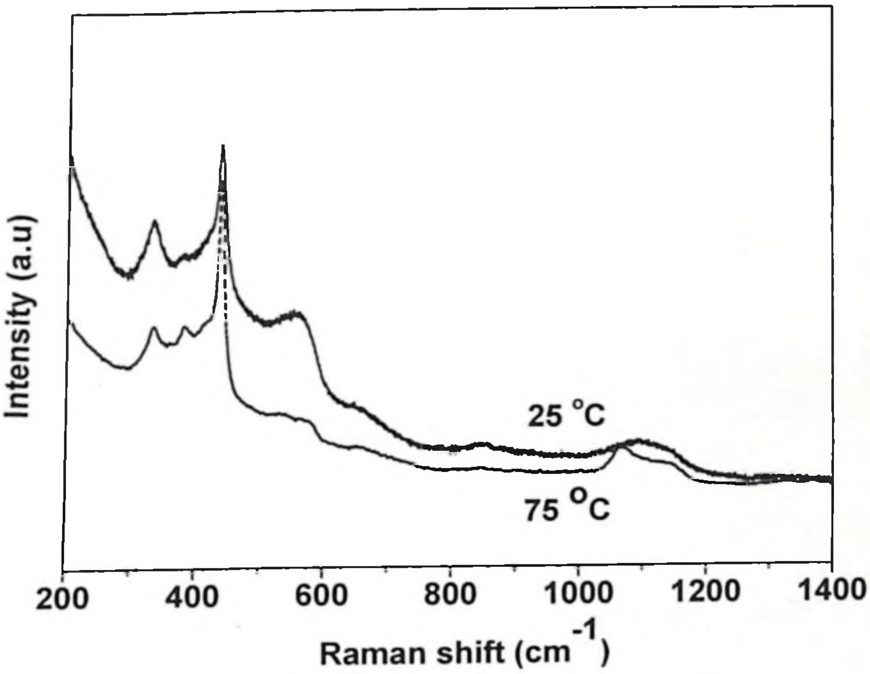

Fig. 3.9 Raman spectra of ZnO nanorods obtained at 25 °C and 75 °C

weak in the one prepared at 25 °C. The intensity of the UV emission band increases with the temperature of preparation of the nanorods, where as the intensity of the bands in the visible region decreases (Fig. 3.8b). This variation correlates well with that of the 580 cm^{-1} Raman band (Fig. 3.9) which arises from intrinsic lattice defects [26]. The intensity of the 580 cm^{-1} Raman band decreases with the increasing temperature of the reaction. The Raman bands at 433 and 378 cm^{-1} are attributed to E_2 mode and A_1 (TO) modes, respectively [25,27]. The band at 331 cm^{-1} could arise from a multiphonon process [27]. The mechanism of the formation of ZnO nanorods can be described as follows. Zinc metal on reaction with water slowly gives out hydrogen. The oxygen liberated reacts with Zn metal to give the oxide as given by the following reaction:

$$Zn(s) + H_2O(l) \longrightarrow ZnO(s) + H_2(g)$$

Here (s), (l) and (g) represent solid, liquid and gas, respectively. It may be noted that the evolution of hydrogen accompanying the reaction of Zn metal with water has been documented in the literature [22,23]. In the reaction of zinc metal with water, it is reported that ZnO is formed first and $Zn(OH)_2$ at a later stage [28,29]. The growth of ZnO nanorods probably occurs by making use of the oxide nuclei (Fig. 3.10) that may be present on the metal surface.

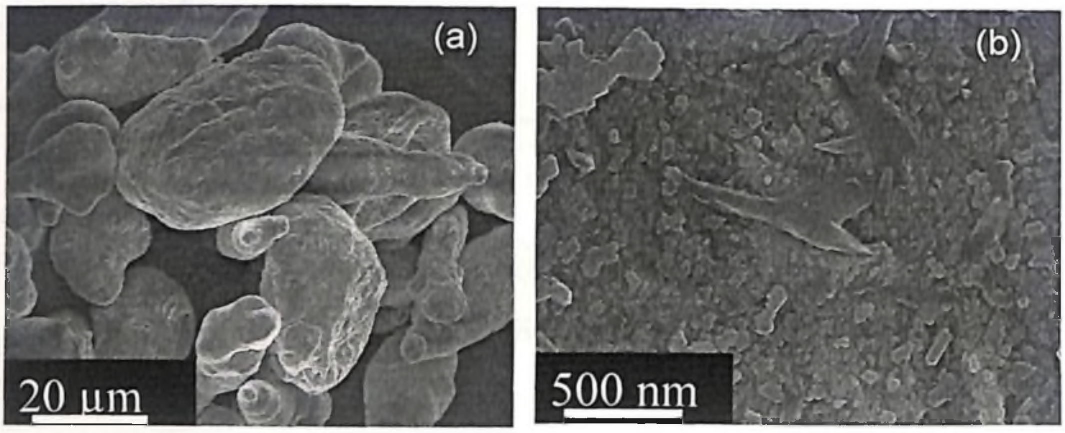

Fig. 3.10 low (a) and high (b) magnification FESEM images of Zn metal powder

(b) $Al(OH)_3$ nanorods

We have carried out the reaction of Al metal powder with water. Fig. 3.11a shows a FESEM image of the Al metal surface. Fig. 3.11b shows a FESEM image of the nanorods obtained by the reaction of Al powder with water at 75 °C. The nanorods are uniform in diameter varying between 7 and 14 nm, with an average diameter of 10 nm and an average length of 300 nm. Fig. 3.11 c shows a TEM image

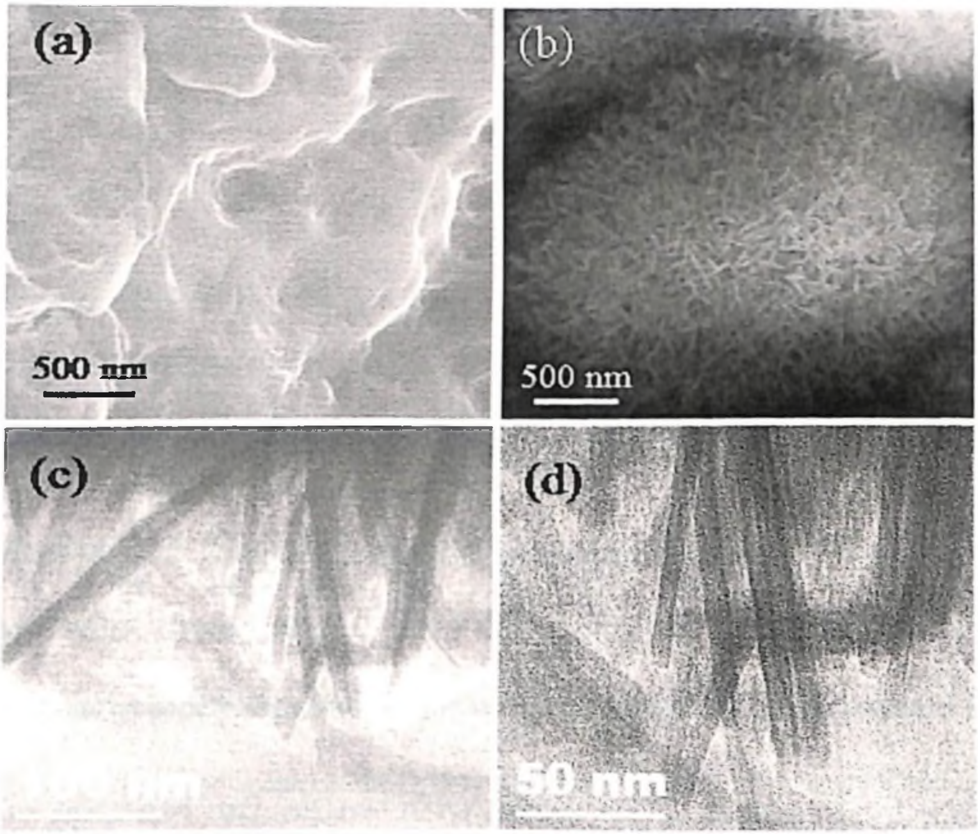

Fig. 3.11 a and b FESEM images of the Al metal surface and $Al(OH)_3$ nanorods obtained by the reaction of Al metal powder with water at 75 °C respectively. c and d are TEM images of the $Al(OH)_3$ nanorods obtained at 50 °C and 75 °C respectively.

of $Al(OH)_3$ nanorods obtained at 50 °C and d shows a TEM image of the $Al(OH)_3$ nanorods obtained at 75 °C. The diameters of the nanorods are in the 8–14 nm range with an average length of 250 nm. The XRD patterns of the nanorods (Fig. 3.12)

were characteristic of the bayerite phase of $Al(OH)_3$ ($a = 0.501$ nm, $c = 0.469$ nm, JCPDS data, card no. 12-0457).

The formation of $Al(OH)_3$ nanorods by the reaction of Al metal with water can be explained as follows. Al metal also gives hydrogen on reaction with water [22,23]:

$$2Al(s) + 3H_2O(l) \longrightarrow Al(OH)_3(s) + 3/2H_2(g)$$

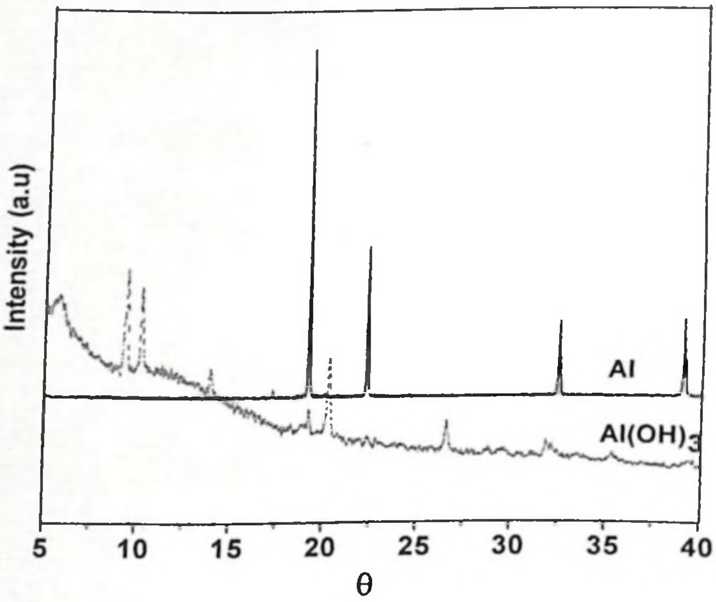

Fig. 3.12 XRD patterns of $Al(OH)_3$ nanorods along with the starting metal sample

Unlike the reaction of Zn metal with water, the reaction of Al metal with water gives rise to the hydroxide instead of the oxide. Formation of $Al(OH)_3$ by reaction of Al metal with water has been reported in the literature [30,31]. The formation of $Al(OH)_3$ is also promoted by the presence of Al_2O_3 [32].

We have confirmed the formation of $Al(OH)_3$ by IR spectroscopy (see Fig. 3.13) as well as Raman spectroscopy (see Fig. 3.14). In the fundamental hydroxyl stretching region, we are observed peaks in IR spectra (Fig. 3.13a) at 3648, 3618, 3540, 3453 and 3402 cm^{-1}. Bayerite mid-IR spectra (Fig. 3.13b) show high intense bands at 1020 cm^{-1} (hydroxyl deformation), 976, 768 cm^{-1} (hydroxyl translation), and 535 and medium intense bands at 717, 586, 560, 475 and 424 cm^{-1}.

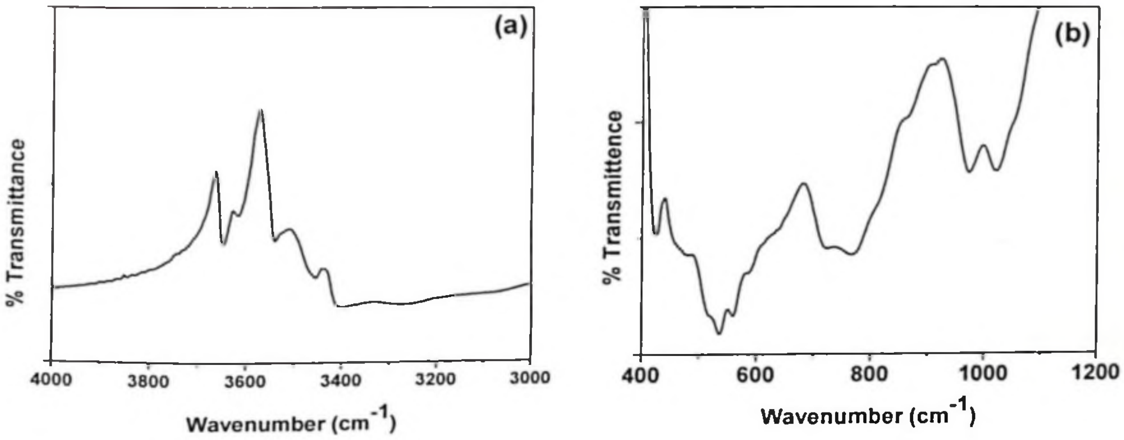

Fig. 3.13 near-IR (a) and mid-IR (b) spectra of $Al(OH)_3$ nanorods

Gibbsite and bayerite (polytypes of aluminum tryhydroxides) have the same structural sheet-like unit, which consists of a layer of aluminium ions sandwiched between two layers of hexagonally packed hydroxyl ions, in the plane defined by the *a* and *b* axes. The oxygens of one layer lie directly above the oxygens at the top of the layer below. The sheet-like units are stacked along the *c* axis [34-36]. The difference in structure between gibbsite and bayerite is that one can be generated from the other by a rotation about the *c* axis of one of the sheet-like units by 60° [36]. The Raman bands (see Fig. 3.14) agree with those reported in the literature [33,37]. Raman spectrum of the bayerite nanorods shows three major bands at 3653, 3541 and 3418 cm^{-1} and three shoulder bands at about 3624, 3450 and 3439 cm^{-1} (Fig. 3.14a) are similar with those found by Raoul Island in New Zealand [37]. Bayerite consists of the same hexagonally packed hydroxyl group as does gibbsite. The crystal structure of both minerals is monoclinic, *P*21/*n*. Differences in the

Raman spectra in the stretching vibration region reflect the Al—OH distance of 1.74–2.06 Å for bayerite compared with 1.73–2.14 Å for gibbsite, and the OH—OH distance of 2.92–3.24 Å for bayerite compared with 2.75–3.24 Å for gibbsite [33]. The shoulder peaks at 3450 and 3439 cm^{-1} may be attributed to surface hydroxyl groups in the bayerite structure. The bayerite spectrum in the low-wavenumber region (Fig. 3.14 b and c) is not as complex as the gibbsite spectrum and these two phases are therefore well distinguished, although bands at 1005, 976, 890, 433 and 322 cm^{-1} may overlap with the gibbsite bands at 1019,

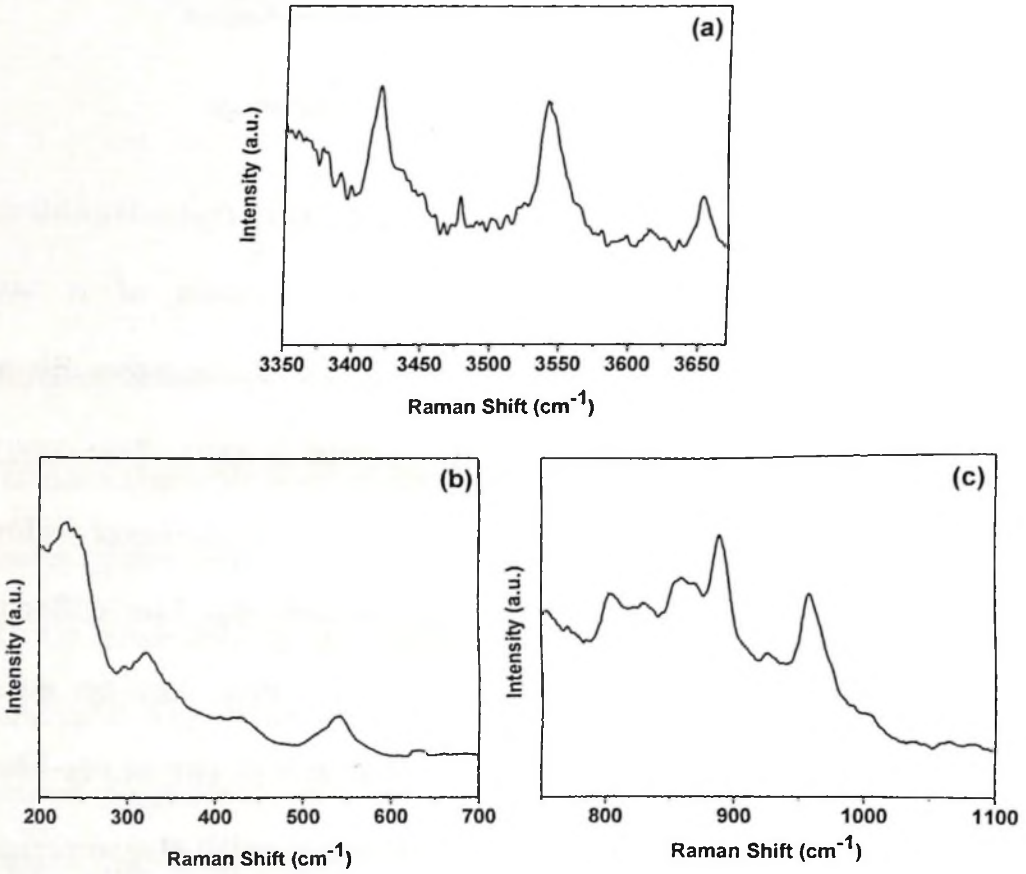

Fig. 3.14 Raman spectra of high-wavenumber region (a) and low-wavenumber region (b and c) of $Al(OH)_3$

980, 892, 444 and 321 cm^{-1}. However, other bands of bayerite are well resolved and are distinctly different from those of gibbsite. The bands with greatest intensity are at 542 and 296 cm^{-1} [33].

3.5 Conclusions

In conclusion, we have found a new and simple method for preparing ZnO nanorods by the reaction of the zinc powder or zinc foils with water at relatively low temperatures. Addition of ethylenediamine to water favors the formation of the ZnO nanorods. Thus, the reaction time is considerably reduced in the presence of ethylenediamine. Reaction of Al powder or Al foils with water gives rise to $Al(OH)_3$ nanorods. The formation of ZnO and $Al(OH)_3$ nanorods from the metals are both governed by the basic reaction between the metals and water giving hydrogen. The growth of the nanorods could be occurring at the small oxide nuclei that may be present on the metal surfaces.

References

1. Z. L. Wang *Mater. Today* **2004**, *7*, 26.
2. C. N. R. Rao and A. Govindaraj (**2005**) *"Nanotubes and Nanowires"*, *The RSC Nanoscience & Nanotechnology series*, (Eds. H. Kroto, P. O'Brien, H. Craighead) Royal Society of Chemistry (London).
3. Z. R. Qiu, K. S. Wong, M. M. Wu, W. J. Lin and H. F. Xu, *Appl. Phys. Lett.* **2004**, *84*, 2739.
4. B. P. Zhang, N. T. Binh, Y. Segawa, Y. Kashiwaba and K. Haga, *Appl. Phys. Lett.* 2004, *84*, 586.
5. S. F. Yu, C. Yuen, S. P. Lau, W. I. Park and G. C. Yi, *Appl. Phys. Lett.* **2004**, *84*, 3241.
6. Q. X. Zhao, M. Willander, R. E. Morjan, Q. H. Hu and E. E. B. Campbell, *Appl. Phys. Lett.* 83 (2003) 165-167.
7. C. J. Lee, T. J. Lee, S. C. Lyu, Y. Zhang, H. Ruh and H. J. Lee, *Appl. Phys. Lett.* 2002, *81*, 3648.
8. J. -J. Wu and S. -C. Liu, *Adv. Mater.***2002**, *14*, 215.
9. X. Liu, X. H. Wu, H. Cao and R. P. H. Chang, *J. Appl. Phys.* **2004**, *95*, 3141.
10. Y. Zhang, H. B. Jia, R. M. Wang, C. P. Chen, X. H. Luo, D. P. Yu and C. J. Lee, *Appl. Phys. Lett.* **2003**, *83*, 4631.
11. Y. C. Kong, D. P. Yu, B. Zhang, W. Fang and S. Q. Feng, *Appl. Phys. Lett.* **2001**, *78*, 407.

12. S. C. Lyu, Y. Zhang, C. J. Lee, H. Ruh and H. J. Lee, *Chem. Mater.* **2003**, *15*, 3294.

13. W. I. Park, D. H. Kim, S. W. Jung and G. C. Yi, *Appl. Phys. Lett.* **2002**, *80*, 4232.

14. Y. Li, G. W. Meng, L. D. Zhang and F. Phillipp, *Appl. Phys. Lett.* **2000**, *76*, 2011.

15. C. Liu, J. A. Zapien, Y. Yao, X. Meng, C. S. Lee, S. Fan, Y. Lifshitz and S. T. Lee, *Adv. Mater.* **2000**, *15*, 838.

16. H. Yu, Z. Zhang, M. Han, X. Hao, and F. Zhu, *J. Am. Chem. Soc.* **2005**, *127*, 2378.

17. B. Cheng, W. Shi, J. M. Russell-Tanner, L. Zhang and E. T. Samulski, *Inorg. Chem.* **2006**, *45*, 1208.

18. C. Wang , E. Shen, E. Wang, L. Gao, Z. Kang, C. Tian, Y. Lan and C. Zhang , *Mater. Lett.* **2005**, *59*, 2867.

19. B. Liu and H . C. Zeng, *J. Am. Chem. Soc.* **2003**, *125*, 4430.

20 A. Dev, S. Kar, S. Chakrabarti and S. Chaudhuri, *Nanotechnology* **2006**, *17*, 1533.

21. L. S. Panchakarla, A. Govindaraj and C. N. R. Rao, *J. Cluster Science* **2007**, *18*, 660.

22. L. Liepina, A. Tetere, *Doklady Akademii Nauk SSSR* **1953**, *90,* 413.

23. A. Zuttel, *Naturwissenschaften* **2004**, *91*, 157.

24. N. S. Pesika, K. J. Stebe and P. C. Searson, *J. Phys. Chem. B* **2003**, *107*, 10412.

25. J. Liang, J. Liu, Q. Xie, S. Bai, W. Yu and Y. Qian, *J. Phys. Chem. B* **2005**, *109*, 9463.

26. C. Bundesmann, N. Ashkenov, M. Schubert, D. Spemann, T. Butz, E. M. Kaidashev, M. Lorenz and M. Grundmann, *Appl. Phys. Lett.* **2003**, *83*, 1974.

27. T. C. Damen, S. P. S. Porto and B. Tell, *Phys. Rev.* **1966**, *142*, 570.

28. M. Kitano, T. Okabe and M. Shiojiri, *J. Cryst. Growth* **1995**, *152*, 73.

29. M. Kitano and M. Shiojiri, *J. Electrochem. Soc.* **1997**, *144*, 809.

30. A. R. Studart, M. D. M. Innocentini, I. R. Oliveira and V. C. Pandolfelli, *J. European Ceramic Soc.* **2005**, *25*, 3135.

31. A. Y. Godymchuk, V. V. An and A. P. Il'in, *Fizika i Khimiya Obrabotki Materialov* **2005**, *5*, 69.

32. E. S. Martin, M. L. Weaver, J. E. Marhanka, A. Pearson and M. Madono. U. S. patent 87-137159 19871223 (**1993**).

33. R. L. Frost, H. D. Ruan and J. T. Kloprogge, *J. Raman Spectroscopy* **2001**, *32*, 745.

34. R. L. Frost, J. T. Kloprogge, S. C. Russell, Szetu, J. *Appl. Spectrosc.* **1999**, 53, 423.

35. P. H. Hsu, T. F. Bates, *Mineral. Mag.* **1964**, *33*, 749.

36. J. L. Bersillow, D. W. Brown, F. Fiessinger, J. D. Hem, *J. Res. US Geol Surv.* **1978**, *6*, 325.

37. K. A. Rodgers, M. R. Gregory, R. P. Cooney, *Clay Miner.* **1989**, 24, 531.

Chapter 4

Carbon Nanostructures and Graphite-Coated Metal Nanostructures Obtained by the Pyrolysis of Ruthenocene and Ruthenocene-Ferrocene Mixtures*

Summary

Pyrolysis of ruthenocene carried out in an atmosphere of argon or hydrogen is found to give rise to spherical nanoparticles of carbon with diameters in the 10-200 nm range. Pyrolysis of ruthenocene as well as mixtures of ruthenocene and ethylene in hydrogen gives rise to spherical nanoparticles, which contain a high proportion of sp^3 carbon. Under certain conditions, pyrolysis of ruthenocene gives rise to graphite coated ruthenium nanoparticles as well as worm-like carbon structures. Pyrolysis of mixtures of ruthenocene and ferrocene gives rise to nanoparticles or nanorods of FeRu alloys inside carbon nanotubes.

---

* Paper based on this study has been published in *Bull. Mater. Sci.*, **2007**, *30* (1), 23-29.

4.1 Introduction

Pyrolysis of organometallic precursors has been employed to prepare novel carbon structures by several workers [1-5]. Thus, pyrolysis of metallocenes such as ferrocene, cobaltocene and nickelocene in the presence or absence of other hydrocarbons gives carbon nanotubes with out any external metal catalyst [6]. Such pyrolysis also gives rise to metal particles such as Co and Fe covered by graphite sheets or carbon coated metal nanoparticles [7]. The nature of the pyrolysis of hydrocarbons such as benzene in an inert atmosphere gives rise to fine uniform size spherical particles of carbon, which are established to be graphite type [8]. Even though several studies have been carried out on the preparation of ruthenium particles decorated on carbon structures [9-11], there has been no systematic study on the pyrolysis of ruthenocene, $Ru(C_5H_5)_2$, to generate carbon-supported metal structures. Like other metallocenes, ruthenocene also sublimes and by using an inert carrier gas one can transport and decompose this ruthenocene vapor at high temperatures.

4.2 Scope of the present study

We have carried out the pyrolysis of ruthenocene to study the nature of nanoparticles obtained from the decomposition of ruthenocene. Pyrolysis of ruthenocene with different carbon sources (hydrocarbons), different carrier gases and temperatures have been studied. We have also studied the incorporation of Ru and Fe inside the carbon nanotubes by pyrolysis of different molar ratios of ruthenocene and ferrocene.

4.3 Experimental and related aspects

The two procedures used for the pyrolysis of ruthenocene are as follows.

(a) Synthesis of carbon spheres

In Procedure 1, typically 100 mg of ruthenocene was taken in a stainless steel autoclave (Swagelok) of 20 ml capacity and then sealed in an argon atmosphere. The autoclave was then placed inside a horizontal tube furnace maintained at 1000 °C for 10 min (in an inert atmosphere) and then cooled to room temperature. After opening the autoclave the black pyrolyzed product was collected and analyzed. This procedure is similar to that reported by Shanmugam and Gedanken [12] for the preparation of carbon nanotubes by the pyrolysis of Ru(III) acetylacetonate.

(b) Synthesis of Ru containing carbon materials

In Procedure 2, Ru containing carbon materials were prepared by the pyrolysis of ruthenocene along with ethylene using a procedure similar to that for the synthesis of carbon nanotubes [6]. A known quantity of ruthenocene was placed in a quartz boat located at one end of a narrow quartz tube (10 mm inner diameter) which in turn was placed in a duel (two-stage) furnace system. The part of the quartz tube containing the ruthenocene was in the first furnace and ruthenocene was sublimed by raising the temperature to 400 °C at a heating rate of 50 °C/min. Argon (hydrogen in the case of synthesis of elongated particles) was used as a carrier gas for carrying the ruthenocene vapors into the second furnace. The role of ethylene was to provide an additional carbon source. Ethylene was admitted into the reaction tube just before the sublimation of ruthenocene. The flow rates of the gases were controlled using the UNIT mass flow controllers. Pyrolysis takes place inside the second furnace and its temperature was maintained constant for each reaction and was varied from 900 °C to 1300 °C (from one reaction to other). Pyrolysis yielded profuse quantities of carbon deposits at the centre and outlet of the second furnace. The samples were collected from the interior of the quartz reaction tube gives elongated carbon spheres, carbon coated metal particles and worm-shaped carbon structures. Similar experiments were carried out to prepare FeRu metal alloy nanorods inside the carbon nanotubes (CNTs). In this case, we used 1:1, 1:4 and 4:1 (molar ratios) of ruthenocene-ferrocene mixtures for the pyrolysis.

Techniques used for characterization

X-ray diffraction (XRD): X-ray diffraction (XRD) patterns of the samples were recorded in the θ-2θ Bragg-Bretano geometry with a Siemens D5005 diffractometer using Cu Kα (λ=0.151418 nm) radiation.

Scanning electron microscope (SEM): Scanning electron microscope images of the samples were recorded using a LEICA S440i scanning electron microscope.

Field emission scanning electron microscope (FESEM): FESEM images were recorded with a FEI NOVA NANOSEM 600.

Raman spectroscopy: Raman spectra were recorded with LabRAM HR high resolution Raman spectrometer (Horiba Jobin Yvon) using He-Ne Laser (λ=630 nm).

Transmission electron microscopy (TEM): Transmission electron microscope (TEM) images were obtained with a JEOL JEM 3010, operating with an accelerating voltage of 300 kV and JEOL JEM 3010 and FEI Tecnai S30 operating at 300 kV. The samples were prepared by dispersing the product in CCl_4. A drop of the suspension was then put on a holey carbon coated Cu grid and allowed to evaporate slowly.

Vibrating sample magnetometer (VSM): Magnetic measurements were carried out for different samples by using the vibrating sample magnetometer (VSM) in PPMS (Physical Property Measurement System).

4.4 Results and Discussion

SEM images of the carbon spheres obtained by the pyrolysis of ruthenocene in an Ar atmosphere at 1000 °C, using procedure 1, are shown in figure 4.1a and b. These unconnected spheres are graphitic,

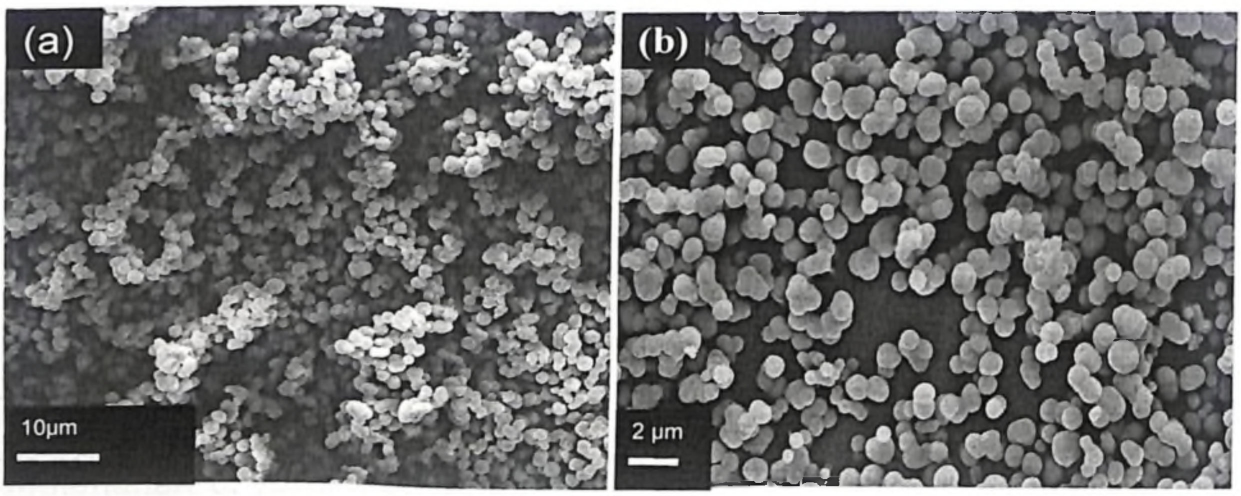

Fig. 4.1. low (a) and high (b) magnification SEM images of ruthenium supported carbon spheres prepared by pyrolysis of ruthenocene at 1000 °C in argon atmosphere using Procedure 1

with having diameters ranging from 500 nm to 1 µm. Carbon spheres of uniform size were also obtained by the pyrolysis of ruthenocene in the presence or absence of hydrocarbons using procedure 2. Figure 4.2a shows a SEM image of uniform-sized carbon spheres of ~ 300 nm diameter obtained in the presence of 200 sccm (sccm=standard cubic centimeter per minute) of argon carrier gas at 1300 °C. Reactions carried out using procedure 2 at different temperatures in the 1000°C - 1300°C range, under similar conditions yielded similar carbon spheres of uniform size. However, pyrolysis of the ruthenocene-ethylene mixture at 1350 °C (with hydrogen and ethylene flow rates of 150 and 50 sccm respectively) gives connected carbon spheres of around 70 nm diameter, as shown in the FESEM image of figure 4.2b. Interestingly, these carbon spheres are different from the spheres obtained in the absence of the

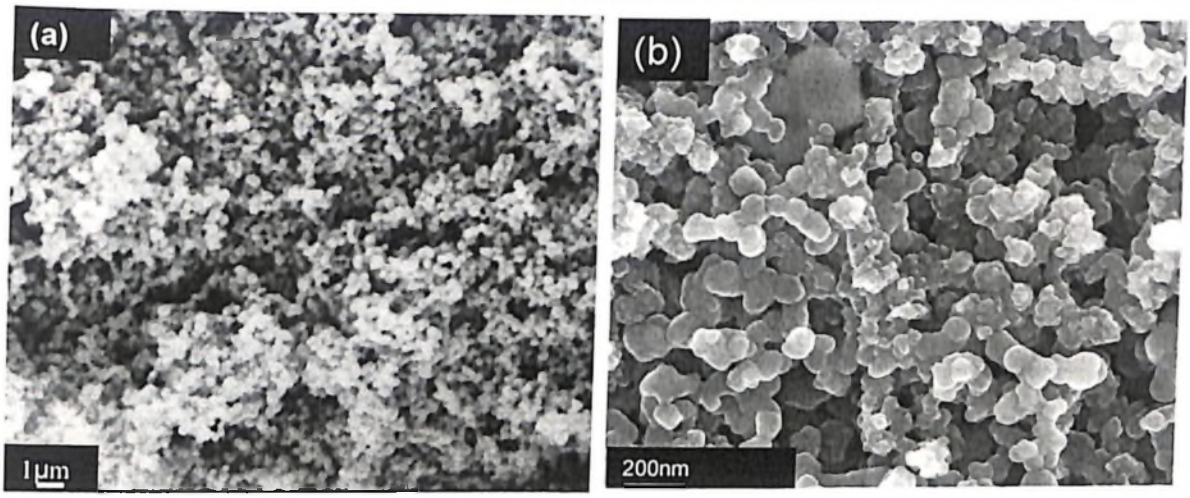

Fig. 4.2. (a) SEM images of ruthenium supported carbon spheres prepared by pyrolysis of ruthenocene at 1300 °C in the presence of argon 200 sccm by using Procedure 2, (b) FESEM images of rutheniumsupported carbon spheres prepared by pyrolysis of ruthenocene at 1350 °C in the presence of hydrogen and ethylene flow rates 150 and 50 sccm respectively, by using Procedure 2.

hydrocarbon (shown in Fig. 4.1 and Fig. 4.2a). The Raman spectrum of these carbon spheres is shown in figure 4.3a. We observe intense bands at 1340 and 1593 cm^{-1}, the former being due to sp^3 carbon as in diamond and the latter due to graphitic (sp^2) carbon. The relative intensities of these two bands indicate the dominance of sp^3 carbon over sp^2 carbon and the material looks almost pure glassy carbon or diamond-like carbon. Pyrolysis of ruthenocene with a mixture of argon and ethylene with flow rates of 150 and 50 sccm respectively at 1100 °C gives carbon spheres with diameters in the 500-800 nm range, as shown in figure 4.4a. The Raman spectrum of these spheres is shown in figure 4.3b which shows bands at 1330 and 1593 cm^{-1} of similar intensities, indicating the presence of equal amount of sp^2 and sp^3 carbon. In figure 4.4b we show a TEM image of amorphous carbon-coated ruthenium nanoparticles. EDAX analysis shows the presence of ruthenium. The inset in figure 4.4b shows a TEM image of a carbon-coated Ru particle.

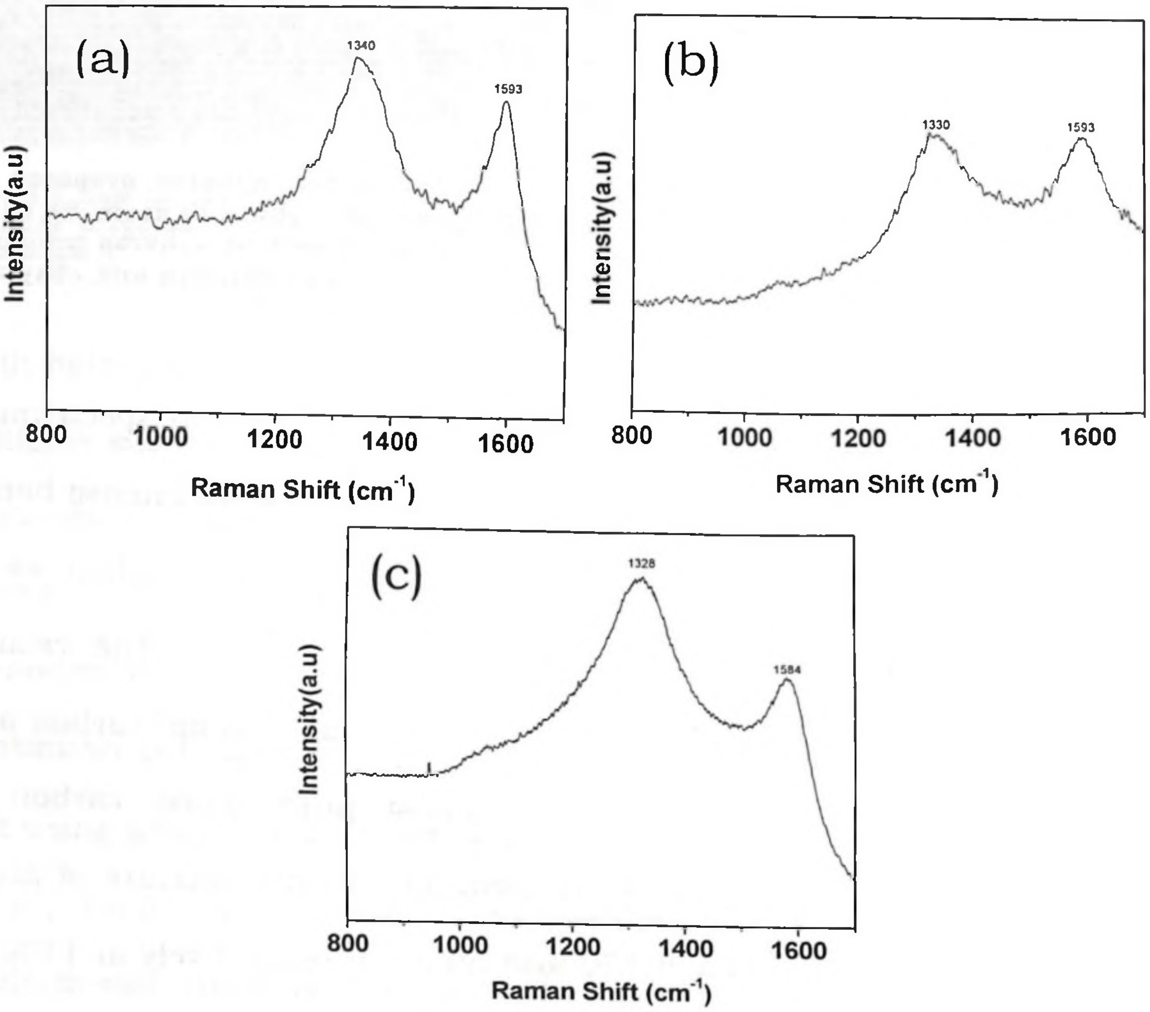

Fig. 4.3. Raman spectra of Ru-supported carbon spheres prepared under different conditions: (a) by pyrolysis of ruthenocene at 1350 °C in a mixture of hydrogen and ethylene gases with flow rates 150 and 50 sccm respectively, (b) by pyrolysis of ruthenocene in argon and ethylene mixturewith flow rates of 150 and 50 sccm respectively at 1100 °C and (c) pyrolysis ofruthenocene in argon (150 sccm) with a mixture of 50 sccm of ethylene bubbled through thiophene at 950 °C.

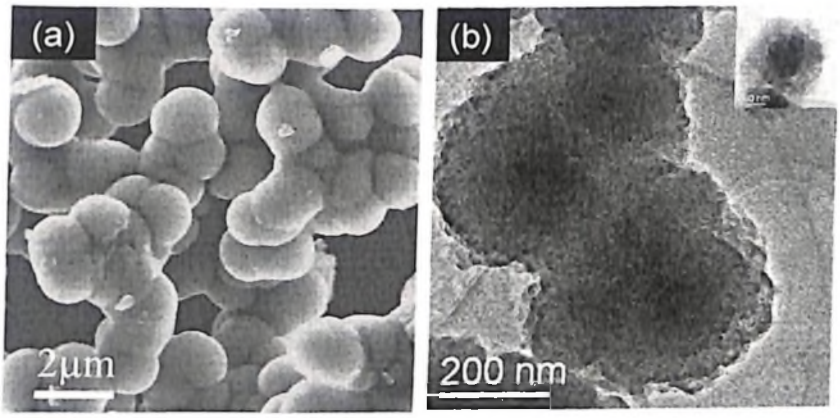

Fig. 4.4. (a) FESEM images of carbon spheres prepared by pyrolysis of ruthenocene at 1100 °C in the presence of argon and ethylene with flow rates 150, 50 sccm respectively, (b) shows a TEM image of the spheres, the inset showing a single sphere of carbon coated ruthenium.

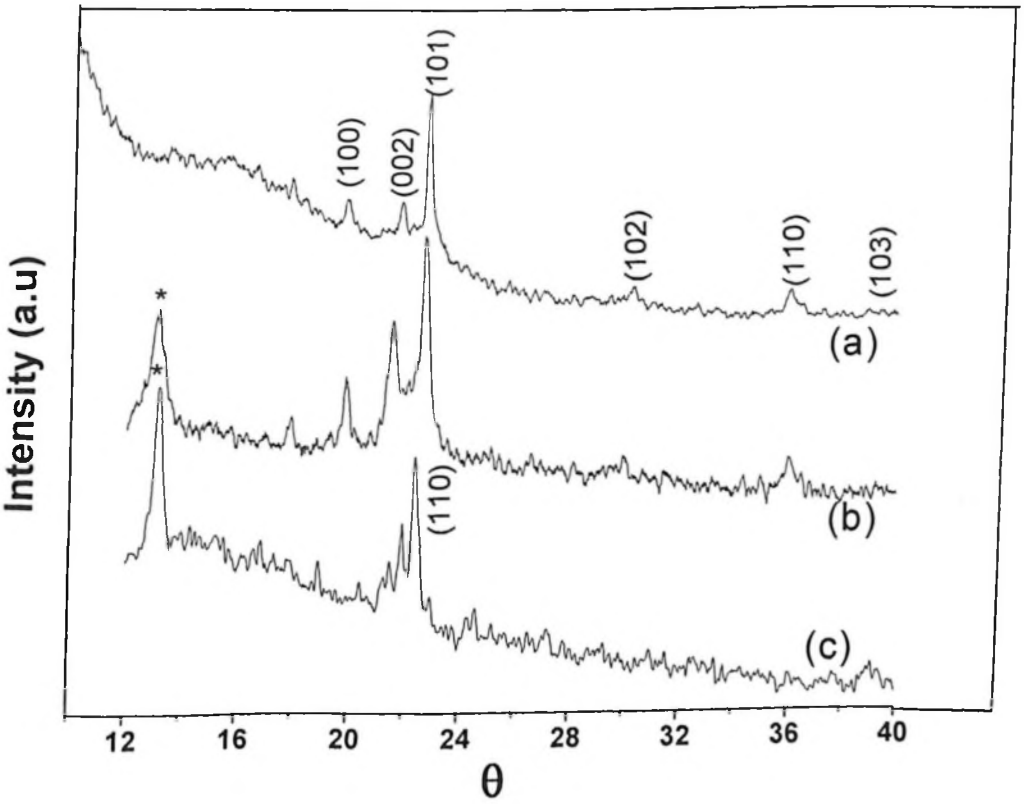

Fig. 4.5. XRD patterns of (a) ruthenium supported carbon spheres (b) FeRu (1:1) binary alloy nanowires inside carbon nanotubes and (c) iron nanowires encapsulated inside carbon nanotubes (asterisk corresponds to carbon nanotube peak).

The electron diffraction pattern as well as the XRD pattern (see figure 4.5a) of these nanospheres confirms the HCP structure of Ru (a= 2.698 Å and c= 4.272 Å, JCPDS file: 02-1258).

Worm-like carbon structures were obtained by the pyrolysis of ruthenocene at 950 °C in the presence of thiophene, argon and ethylene at flow rates of 150 sccm and 50 sccm respectively. In these experiments ethylene was bubbled through thiophene through out the reaction. SEM and TEM images of the worm-like carbon structures are shown in figure 4.6a and b respectively. The elongated structures have a diameter of around 1 μm. EDAX analysis shows the presence of Ru. The Raman spectrum of these carbon structures (figure 4.3c) shows that sp^3 carbon is in majority rather than sp^2 carbon.

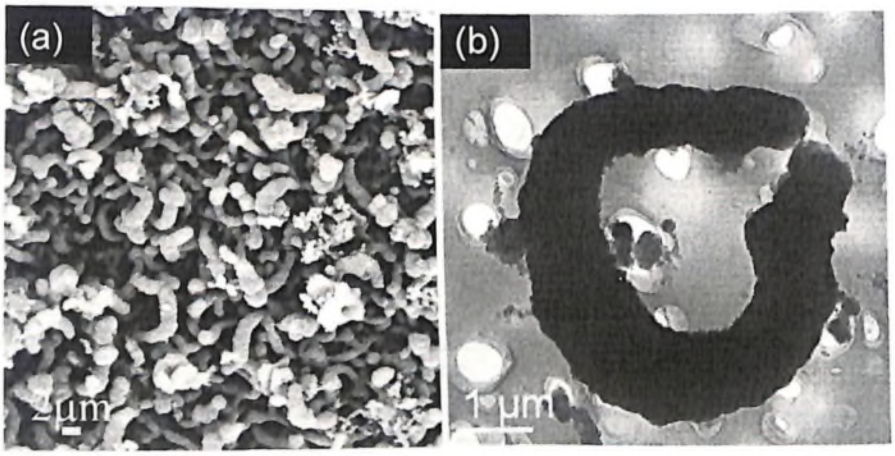

Fig. 4.6. (a) SEM image of carbon structures prepared by pyrolysis of ruthenocene with a mixture of argon (150 sccm) and 50 sccm of ethylene bubbled through thiophene at950 °C and (b) shows the TEM image of these structures

By using ferrocene instead of ruthenocene, under the conditions of procedure 2, we obtained carbon nanotubes rather than carbon spheres as in the case of ruthenocene [1,2]. This may be due to the higher stability, diffusion as well as the solubility of carbon in Fe with a lower eutectic temperature. The Fe-C phase diagram shows a maximum solubility of carbon in Fe to be around 7%. The eutectoid composition is Fe-0.83 wt%C and at this composition the high-temperature austenite phase will undergo the eutectoid reaction at 723 °C and at this temperature γ-Fe, α-Fe and carbon or (Fe_3C) may coexist [13]. Also, the Ru-C phase diagram is a simple eutectic with a eutectic temperature of 1940 °C and eutectic concentration of ~ 18 at% C and maximum solubility of C is ~0.37 wt% C. Since RuC is unstable with decreasing temperature carbon precipitates in the form of graphite on the basal planes. Although Ru does not form carbides at room temperature, soluble carbon (~0.04 wt.% C at room temperature) strongly effect hardness and resistivity, and impairs workability [14]. Thus, the Fe-C phase diagram seems to indicate the formation of Fe catalyzed growth of carbon nanotubes. Since ruthenium itself is not incorporated and forming carbon nanotubes, we thought it interesting to see the effect of addition of ruthenocene to ferrocene on the growth of carbon nanotubes. It was also of interest to see whether Ru particles decorate the carbon nanotube surface or get encapsulated inside the nanotubes. Interestingly, we found bimetallic FeRu nanostructures which get encapsulated inside the nanotubes as seen in the figures 4.7, 4.8 and 4.9. We were able to get FeRu alloy nanorods inside the carbon nanotubes as well as carbon-coated FeRu alloy nanoparticles by the pyrolysis of a mixture of ruthenocene and ferrocene mixtures of different molar ratios (1:1, 1:4, 4:1) in the presence of argon and ethylene (500 and 50 sccm respectively) at 900 °C. Due to relatively high temperature involved in the synthesis, we are expected to obtain the HCP structure for all the above compositions of FeRu alloy nanostructures [15]. The 1:4 FeRu alloy nanostructure have the lattice constants, a= 2.70 Å and c= 4.27 Å (JCPDS file: 40-1147)) and the 1:1 FeRu alloy nanostructure has the lattice constants, a= 2.60 A and c= 4.17 A. A systematic decrease in the d-spacing was also observed in all FeRu alloy nanostructures as

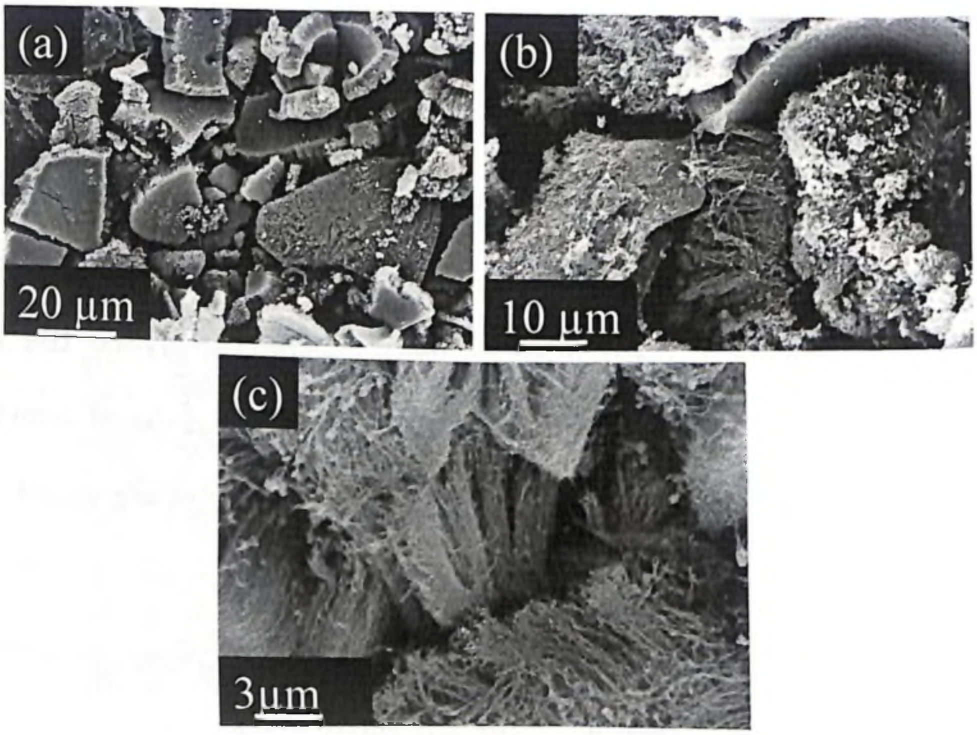

Fig. 4.7 SEM images of RuFe alloy nanorods inside the aligned carbon nanotubes (a) 1:1 (b) 1:4 (c) 4:1 (molar ratios) of ruthenocene-ferrocene mixtures for the pyrolysis.

compared to pure Ru, confirming the smaller Fe atoms are indeed incorporated in the larger Ru lattice.

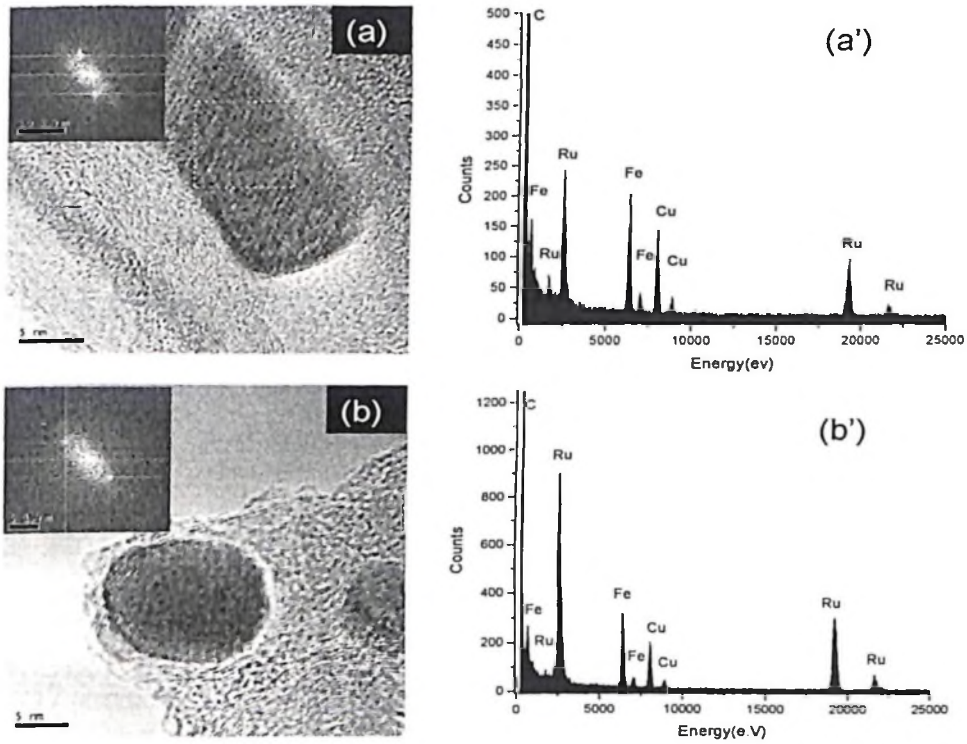

Fig. 4.8. The high magnification TEM images of FeRu alloy nanoparticles and nanorods (inside the carbon nanotubes) obtained by the pyrolysis of a mixture of ruthenocene and ferrocene (1:1) in the presence of Ar and ethylene (500 and 50 sccm respectively) at 900 °C (a) alloy nanorods inside the carbon nanotube (b) alloy nanoparticle. (a') and (b') show the corresponding EDAX patterns.

Figure 4.7 shows SEM images of the alloy nanorods inside the aligned carbon nanotubes starting with 1:1 (Fig. 4.7a), 1:4 (Fig. 4.7b) and 4:1 (Fig. 4.7c) molar ratios of ruthenocene-ferrocene mixtures for the pyrolysis. These nanotubes are grown aligned for several micrometers and lengths are in the order of several microns. Figure 4.8a shows a typical high resolution TEM image of the 1:1 alloy nanorod showing a d-spacing of 2.1 Å. Figure 4.8b shows a high resolution TEM image of 1:4

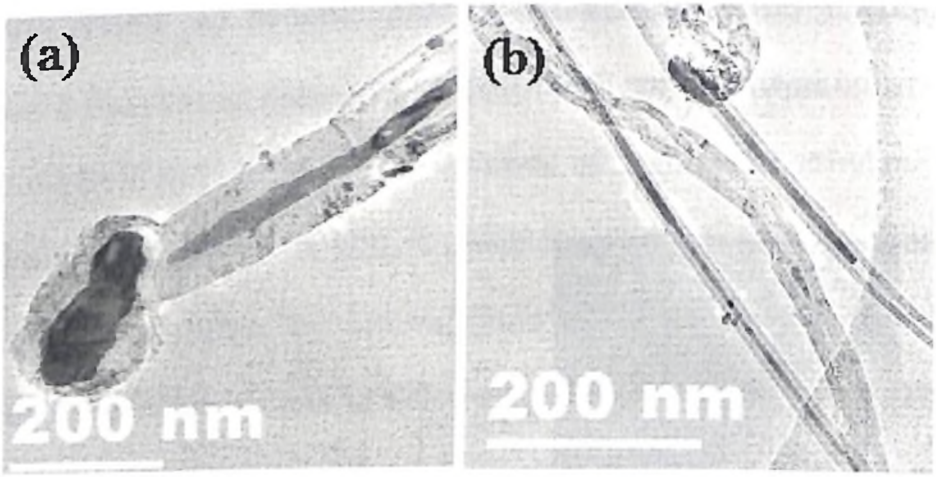

Fig. 4.9. (a-b) Low magnification TEM images of iron-ruthenium alloy nanorods inside carbon nanotubes

FeRu alloy nanoparticle showing a d-spacing of 2.4 Å, confirming the single-crystalline nature. From EDAX analysis (figure 4.8), the Ru:Fe ratio was found 1:1 in the case of nanorods formed inside the CNTs and 4:1 in the case of encapsulated nanoparticles. The electron diffraction patterns shown as insets in figures 4.8a and b corresponds to the alloys and indicate the nanostructures to be single crystalline. The carbon coating in the FeRu nanoparticles is graphitic as can be seen from the TEM image. Figures 4.9a and b show the low magnification TEM images of metal alloy (1:1) nanorods formed inside the CNTs.

Magnetic measurements were carried on the different carbon nanostructures prepared by the pyrolysis of ferrocene, ferrocene-ruthenocene mixtures and ruthenocene in the presence as well as in the absence of hydrocarbons. Magnetic measurements on aligned carbon nanotubes obtained from the pyrolysis of ferrocene-hydrocarbon mixtures have been reported earlier [16], wherein the M vs H curves showed a smooth S-shaped loop with saturation magnetization of ~24 emu/g, which is smaller than that of bulk iron [16]. In the present measurements a maximum field of ~1 T was applied from the start, swept through zero fields, and the direction of the field reversed to get M Vs H hysteresis loops. Figure 4.10 shows typical hysteresis (M Vs H) curves. It is observed that the saturation magnetization decreases from pure iron nanowire encapsulated in carbon nanotubes (prepared by ferrocene pyrolysis) to carbon coated/encapsulated binary FeRu (4:1, 1:4, 1:1) alloy nanostructures (prepared by ferrocene-ruthenocene pyrolysis) and to carbon-coated Ru particles (prepared by ruthenocene pyrolysis) respectively. The saturation magnetization (M_s) of 26, 7, 1.2, 10.7, 0.007 emu/g for the samples such as iron nanowires encapsulated inside carbon nanotubes, FeRu (4:1, 1:1, 1:4) binary alloy nanowires inside carbon nanotubes and carbon coated Ru nanoparticles respectively, while the corresponding coercivity (H_c) of 507, 205, 157, 194, and 20 Oe. In the case of carbon coated Ru nanoparticles, we have observed very low magnetization. Bulk Ru is nonmagnetic where as in nanosize domains it shows ferromagnetism. Recently universal ferromagnetism has been found in nanoparticles [17]. In nanosize particles, surface magnetism dominates at low fields and shows hysteresis. At high fields, diamagnetism dominates. It is also known that

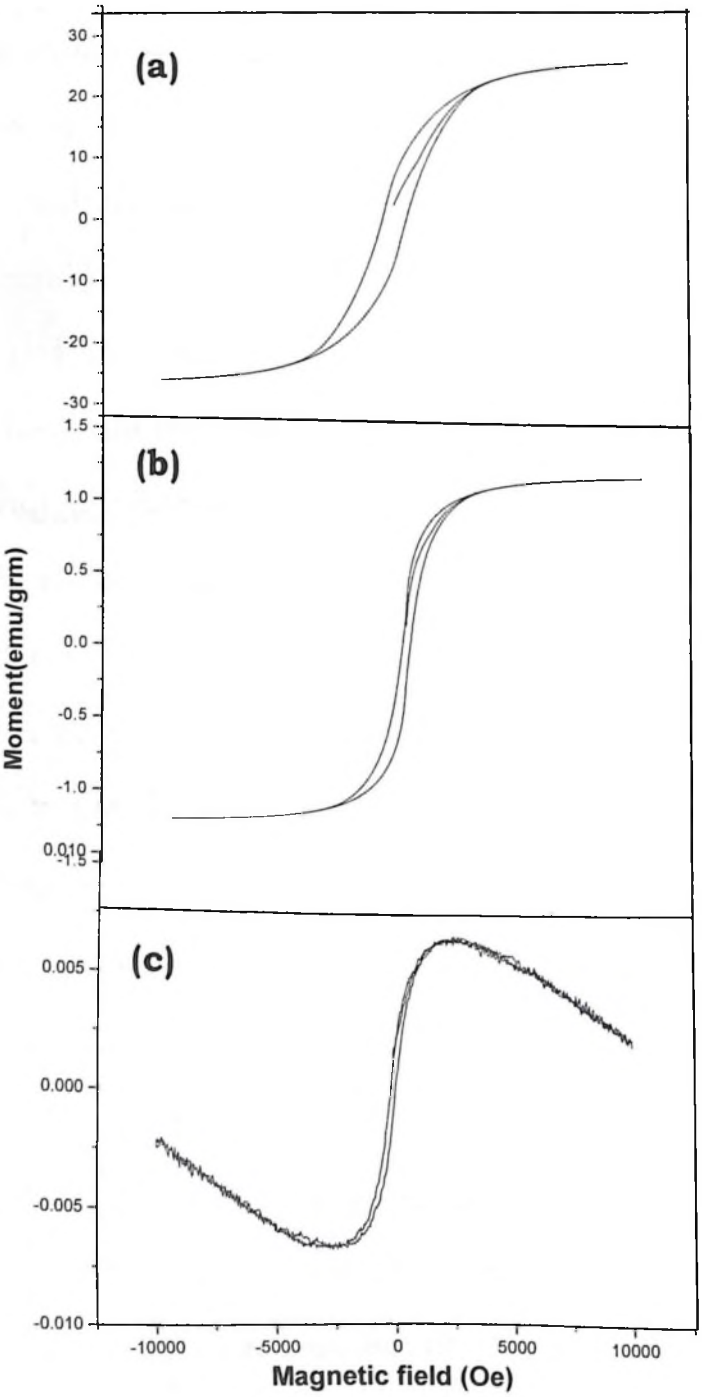

Fig. 4.10. Hysteresis loops (M vs H curves) recorded on samples: (a) iron nanowires encapsulated inside carbon nanotubes (b) FeRu (1:1) binary alloy nanowires inside carbon nanotubes and (c) carbon coated Ru nanoparticles

magnetic elements such as Fe, Co and Ni in nanoscale show enhanced moments due to the reduced coordination of atoms and localization of electrons as compared to the case of bulk materials [18]. The spin and orbital contribution to surface magnetism in the 3d elements have been reported [19]. Several groups have studied magnetism of 4d elements nanoclusters and thin films [20-26]. Hence most of the studies points that magnetism in nanoregime is a surface phenomena.

4.5 Conclusions

Unlike the pyrolysis of ferrocene, cobaltocene and nickelocene where carbon nanotubes are readily obtained, pyrolysis of ruthenocene mainly gives rise to carbon nanospheres. Under certain conditions carbon coated Ru nanoparticles were also obtained. Mixtures of ruthenocene with ferrocene also give rise to FeRu metal nanoparticles and also nanorods covered by carbon, the later being encapsulated inside carbon nanotubes. The pyrolysis method gives rise to useful means to produce nanoparticles of Ru and FeRu alloys. It may be noted that carbon spheres themselves can be obtained by the pyrolysis of hydrocarbon [8]. In view of this it appears as though during the pyrolysis of ruthenocene, cyclopentadienyl radicals undergo decomposition just as in the case of decomposition of pure benzene giving rise to pure carbon structures, with the ruthenium particles forming separate nanoparticles. In the case of Fe, Co and Ni they appear to be better catalysts than Ru to form nanotubes

References

1. C. N. R. Rao, B. C. Satishkumar, A. Govindaraj and M. Nath *ChemPhysChem.* **2001**, *2*, 78.
2. A. Govindaraj and C. N. R. Rao *Pure Appl. Chem.* **2002**, *74*, 1571.
3. R. Andrews, D. Jacques, A. M. Rao, F. Derbyshire, D. Qian, X. Fan, E. C. Dickey and J. Chen, *Chem. Phys. Lett.* **1999,** *303*, 467.
4. S. Huang, L. Dai and A. W. H. Mau, J. Phys. Chem. B **1999**, *103*, 4223.
5. S. Huang, A. W. H. Mau, T. W. Turney, P. A. White and L. Dai, *J. Phys. Chem. B*_**2000**, *104*, 2193.
6. C. N. R. Rao, A. Govindaraj, R. Sen and B. C. Satishkumar, *Mat. Res. Innovat.* **1998**, *2*, 128.
7. R. Sen, A. Govindaraj and C. N. R. Rao, *Chem Phys. Lett.* **1997**, *267*, 276.
8. A. Govindaraj, R. Sen, B. V. N. Raju and C. N. R. Rao, *Phil. Mag. Lett.* **1997**, *76*, 363.
9. J. Garcia, H. T. Gomes, Ph. Serp, Ph. Kalck, J. L. Figueiredo and J. L. Faria, *Carbon* **2006**, *44*, 2384.
10. J. Qiu, H. Zhang, X. Wang, H. Han, C. Liang, C. Li, *Reaction Kinetics and Catalysis Lett.* **2006**, *88*, 269.
11. M –C. Tsai, T –K. Yeh, C –H. Tsai, *Electrochem. Commum.* **2006**, *8*, 1445
12. S. Shanmugam and A. Gedanken, *J. Phys. Chem. B* **2006**, *110*,

2037.

13. H. Kim and W. Sigmund, *Carbon* **2005,** *43*, 1743.
14. E. M. Savitskii, V. P. Polyakova, N. B. Gorina, *Vyrashchivanie Monokrist. Tugoplavkikh Redk.* **1973** *Metal,* Conference Proceedings written in Russian 90
15. H –J. Moon, W. Kim, S. J. Oh, J. Park, J- G. Park, E –J. Cho, J. I. Lee and H –C. Ri, *J. Kor. Phys. Soc.* **2000**, *36*, 49.
16. B. C. Satishkumar, A. Govindaraj, P. V. Vanitha, A. K. Raychaudhuri, C. N. R. Rao, *Chem. Phys. Lett.* **2002,** *362*, 301.
17. A. Sundaresan, R. Bhargavi, N. Rangarajan, U. Siddesh and C. N. R. Rao, *Phy. Rev. B* **2006,** *74,* 161306(R).
18. I. M. L. Billas, A. Chatelain and W. A. de Heer, *Science* **1994**, *265,* 1682.
19. O. Eriksson, A. M. Boring, R. C. Albers, G. W. Fernando, B. R. Cooper, *Phy. Rev. B* **1992**, *45*, 2868.
20. W. C. Wang, Y. Kong, X. He and B. X. Liu, *App. Phy. Lett.* **2006**, *89*, 262511.
21. A. J. Cox, J. G. Louderback, S. E. Apsel, L. A. Bloomfield, *Phy. Rev.* **1994**, *49*, 12295.
22. V. L. Moruzzi and P. M. Marcus, *Phy. Rev. B* **1990**, *42*, 10322.
23. B. Piveteau, M –C, Desjonqueres, Andrzej, M. Oles and Daniel Spanjaard, *Phy. Rev. B* **1996**, *53*, 9251.
24. A. E. García, V. González-Robles and R. Baquero, *Phy. Rev. B*

1999, *59*, 9392.

25. I. Cabria, B. Nonas, R. Zeller and P. H. Dederichs, *Phy. Rev. B* **2002**, *65*, 054414.

26. Y. C. Bae, H. Osanai, V. Kumar and Y. Kawazoe, *Phy. Rev. B* **2004**, *70*, 195413.

Chapter 5

Nitrogen- and Boron-Doped Double-walled Carbon nanotubes*

Summary

This chapter of the thesis deals with the synthesis and spectroscopic characterization of doped (nitrogen and boron) and undoped double-walled carbon nanotubes (DWNTs), prepared by using combustion catalyst.

Double-walled carbon nanotubes (DWNTs) doped with nitrogen and boron have been prepared by the decomposition of a CH_4+Ar mixture along with pyridine (or NH_3) and diborane, respectively, over a $Mo_{0.1}Fe_{0.9}Mg_{13}O$ catalyst, prepared by the combustion route. The doped DWNTs bave been characterized by transmission electron microscopy (TEM), X-ray photoelectron spectroscopy, electron energy loss spectroscopy, and Raman spectroscopy. The dopant concentration is around 1 atom % for both boron and nitrogen. The radial breathing modes

---

*Paper based on these studies has been published in ACS Nano (2008) in the Raman spectra have been employed along with TEM to obtain the inner and outer diameters of the DWNTs. The diameter ranges for the undoped, N-doped (pyridine), N-doped (NH_3), and B-doped DWNTs are 0.73–2.20, 0.74–2.30, 0.73–2.32, and 0.74–2.36 nm, respectively, the boron-doped DWNTs giving rise to a high proportion of the large diameter DWNTs. Besides affecting the G-band in the Raman spectra, N- and B-doping affect the proportion of semiconducting nanotubes.

5.1 Introduction

(a) Double-walled carbon nanotubes

Double-walled carbon nanotubes (DWNTs), first observed in 1996, constitute a unique family of carbon nanotubes (CNTs) [1,2]. DWNTs occupy a position between the single-walled carbon nanotubes (SWNTs) and the multiwalled carbon nanotubes (MWNTs), as they consist of two concentric cylinders of rolled graphene. DWNTs possess useful electrical and mechanical properties with potential applications. Thus, DWNTs and SWNTs have similar threshold voltages in field electron emission, but the DWNTs exhibit longer lifetimes [3]. Unlike SWNTs, which get modified structurally and electronically upon functionalization, chemical functionalization of DWNTs surfaces would lead to novel carbon nanotube materials where the inner tubes are intact. The stability of DWNTs is controlled by the spacing of the inner and outer layers but not by the chirality of the tubes [4]; therefore, one obtains a mixture of DWNTs with varying diameters and chirality indices of the inner and outer tubes. DWNTs have been prepared by several techniques, such as arc discharge [5] and chemical vapor deposition (CVD) using a mixture of ferrocene with a hydrocarbon or alcohol (typical hydrocarbons are methane, alcohol, n-hexane, and benzene) [6–10]. DWNTs have also been prepared by a sulfur-assisted CVD method using methane as the carbon source [11,12].

(b) Doped carbon nanotubes

Applications of CNTs based on their electrical properties strongly depend on the diameter and helicity as well as parity [2,13]. Doping of CNTs by boron and nitrogen renders them p-type and n-type, respectively. MWNTs and SWNTs doped with nitrogen [14–17] and boron [18,19] have been reported. Boron-doped carbon nanotubes appear to exhibit enhanced electron field emission due to the presence of the boron atom at the nanotube edges [20,21]. N-doped CNTs show n-type behavior regardless of tube chirality [22].

5.2 Scope of the present study

We were interested in the synthesis and characterization of boron- and nitrogen-doped DWNTs in view of their potential applications. We have focused on the low doping regime (~1 atom %), where the fundamental band structure is expected to be unchanged relative to the all-carbon model. To our knowledge, except for a report on the preparation of nitrogen-doped DWNTs by using a mixture of methane, ammonia, and argon over an iron-molybdenum catalyst [23], there has been no detailed study of these materials. We have prepared nitrogen-doped DWNTs by the thermal decomposition of a CH_4 + NH_3 + Ar mixture as well as a CH_4 + pyridine + Ar mixture over a $Mo_{0.1}Fe_{0.9}Mg_{13}O$ catalyst, prepared by a new procedure. It may be noted that pyridine has been found to be a good nitrogen source to prepare N-doped MWNTs [16]. We have prepared boron-doped DWNTs by the thermal decomposition of a $CH_4 + B_2H_6 + Ar$ mixture over the $Mo_{0.1}Fe_{0.9}Mg_{13}O$ catalyst at 950 °C. The various DWNTs have been characterized with respect to composition and structure. In particular, the effect of B- and N-doping on the dimensions of the nanotubes has been examined by Raman spectroscopy.

5.3 Experimental and related aspects

(a) Preparation of catalyst ($Mo_{0.1}Fe_{0.9}Mg_{13}O$)

The oxide precursors required to prepare the catalyst for the synthesis of DWNTs were prepared by the combustion route [30,31]. The required amount of $(NH_4)_6Mo_7O_{24}\cdot 4H_2O$ was added to an aqueous solution containing ferric nitrate ($Fe(NO_3)_3\cdot 9H_2O$) and magnesium nitrate ($Mg(NO_3)_2\cdot 6H_2O$) in a Pyrex dish, keeping the molar ratio of Mo:Fe:MgO at 0.1:0.9:13. To this mixture was added an appropriate amount of urea (three times the stoichiometric ratio), which acts as the fuel in the combustion process. The mixture was dissolved by using a minimum amount of distilled water and kept in an oven at 70 °C for 12 h. The Pyrex dish containing the solution was placed in a furnace preheated at 550 °C. The thick orange-red solution immediately started boiling and underwent dehydration. The resulting thick paste frothed and blazed with a white flame, with the production of a light material which then swelled to the capacity of the Pyrex dish. The total combustion process was over in 10 min. The combustion product was baked at 550 °C for 3 h and ground to a fine powder. Preparation of the catalyst by conventional methods, such as wet impregnation or co-precipitation, yields inhomogeneous catalyst particles, whereas the combustion route employed here gives homogeneous catalyst particles.

(b) Synthesis of double-walled carbon nanotubes

Synthesis of DWNTs was carried out in a quartz tube reactor. For each synthesis, 200 mg of the supported Fe-Mo catalyst (Fe-Mo/MgO) was placed in a quartz boat by spreading it uniformly. The quartz boat was inserted into the center of the quartz tube (25 mm dia. and 1 m long) mounted inside an electrical tube furnace. Subsequently, the furnace was heated to 950 °C in an argon atmosphere at a heating rate of 3 °C/min. A mixture of methane and Ar gas was introduced into the reactor. The flow rates of methane and Ar were maintained at 50 and 150 sccm (standard cubic centimeters per minute), respectively. After 20 min, the reactor was cooled to room temperature in an Ar atmosphere. The resulting black dense mat contained a homogeneous dispersion of carbon nanotubes around the oxide grains. This crude material was carefully collected from the boat and subjected to purification.

(c) Synthesis of nitrogen-doped double-walled carbon nanotubes

For obtaining nitrogen-doped DWNTs, the procedure was similar to that used for undoped DWNTs, expect that ammonia or pyridine vapor was taken in mixture with CH_4 [16]. For doping nitrogen by using ammonia, the supported Fe-Mo catalyst (200 mg) was placed in a quartz boat at the center of the quartz reactor tube. The quartz tube was heated to 950 °C in an Ar atmosphere. Subsequently, CH_4 (50 sccm), NH_3 (5 sccm), and Ar (150 sccm) were mixed and introduced at the inlet of the reactor tube. After 20 min, the reactor was cooled to room temperature in an Ar atmosphere. For N-doping using pyridine, the supported Fe-Mo catalyst (200 mg) was placed in a quartz boat at the center of the quartz reactor tube. The quartz tube was heated to 950 °C in an Ar atmosphere. Subsequently, 40 sccm of CH_4 was passed through a bubbler containing pyridine, which carries the pyridine vapor to the furnace. These vapors were mixed with 150 sccm of Ar and passed over the MgO-supported catalyst, maintained at 950 °C for 20 min.

(d) Synthesis of boron-doped double-walled carbon nanotubes

For the synthesis of boron-doped DWNTs, diborane (B_2H_6) was used as the boron source, the rest of the procedure being similar to that for undoped DWNTs. B_2H_6 vapor was generated by the addition of BF_3-diethyl etherate to sodium borohydride in tetraglyme [18]. 50 sccm of CH_4 was mixed and passed along with B_2H_6 vapors. These vapors were further mixed along with 150 sccm of Ar and passed over the MgO-supported catalyst powder, maintained at 950 °C for 20 min.

(e) Purification of undoped as well as doped double-walled carbon nanotubes

In order to dissolve the metal nanoparticles in the DWNTs, the as-prepared nanotubes were treated with concentrated HCl at 60 °C for 24

h. The product was washed with distilled water, dried, dispersed in ethanol under sonication, and filtered using Millipore (0.2 μm) filter paper. The filtered product was dried in an oven at 100 °C for 2 h and heated to 850 °C in a furnace at a rate of 3 °C per minute in flowing hydrogen at 100 sccm and held at that temperature for 6 h to remove the amorphous carbon present on the nanotube walls [32]. The resulting sample was again stirred in concentrated HCl at 60 °C for 3 h and heated in a furnace at 850 °C for 6 h in flowing hydrogen (100 sccm). The same procedure was employed to purify doped DWNTs, except that dilute HCl was used instead of concentrated HCl.

Techniques used for characterization

We have characterized the undoped and doped DWNTs by various techniques.

Scanning electron microscope (SEM): Scanning electron microscope images of the samples were recorded using a LEICA S440i scanning electron microscope.

Field emission scanning electron microscope (FESEM): FESEM images were recorded with a FEI NOVA NANOSEM 600.

UV-Vis absorption and Photoluminescence: UV-Vis absorption measurements were carried out at room temperature with a Perkin-Elmer model Lambda 900 UV/Vis/NIR spectrometer.

Raman spectroscopy: Raman spectra were recorded with LabRAM HR high resolution Raman spectrometer (Horiba Jobin Yvon) using He-Ne Laser (λ=630 nm).

Transmission electron microscopy (TEM): Transmission electron microscope (TEM) images were obtained with a JEOL JEM 3010, operating with an accelerating voltage of 300 kV. The samples were prepared by dispersing the product in CCl_4. A drop of the suspension was then put on a holey carbon coated Cu grid and allowed to evaporate slowly.

EELS: EELS were recorded with a transmission electron microscope (FEI, TECNAI F30) equipped with an energy filter for EELS operating at 300 kV.

Thermogravimetric analysis (TGA): Thermogravimetric analysis was carried out using a Mettler Toledo TGA 850 instrument.

X-ray photoelectron spectroscopy (XPS): X-ray photoelectron spectroscopy was recorded using a VG scientific ESCA Laboratory V spectrometer.

5.4 Results and Discussion

While the decomposition of the CH_4 + Ar over the $Mo_{0.1}Fe_{0.9}Mg_{13}O$ catalyst at 950 °C yielded undoped DWNTs, decomposition of the CH_4 + NH_3 + Ar and CH_4 + pyridine + Ar mixtures gave nitrogen-doped DWNTs. Decomposition of the CH_4 + BH_3 + Ar mixture over the catalyst at 950 °C

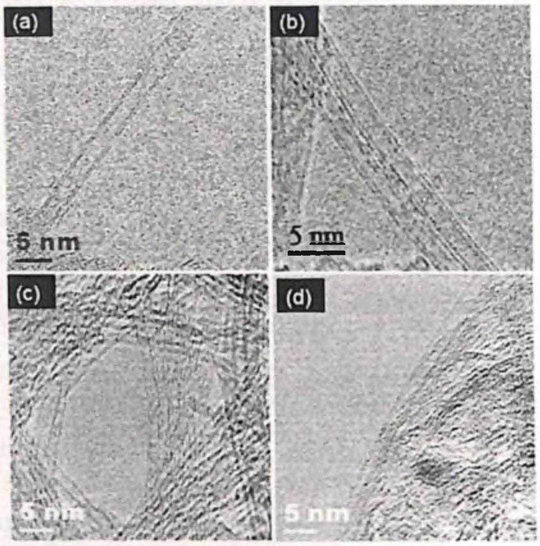

Fig 5.1. HREM images of undoped DWNTs

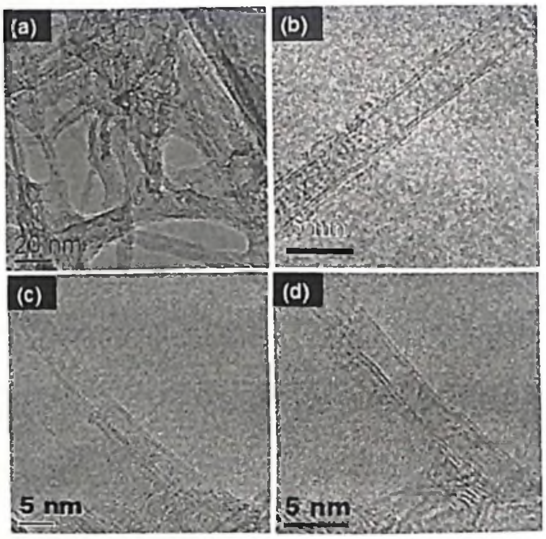

Fig 5.2. TEM (a) and HREM (b-d) images of N-doped DWNTs using ammonia as the nitrogen source.

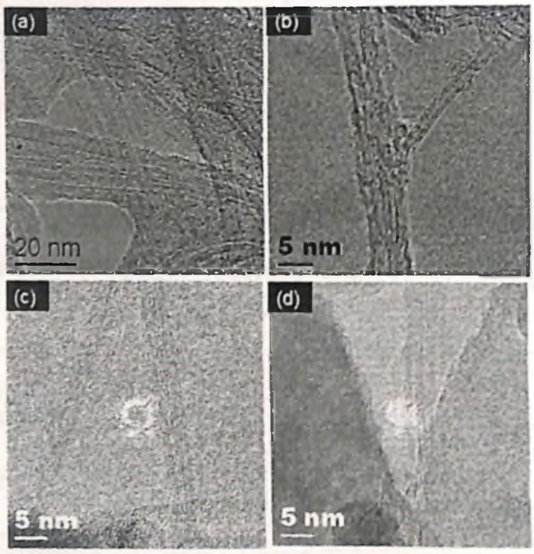

Fig 5.3. TEM (a) and HREM (b-d) images of N-doped DWNTs using pyridine as the nitrogen source

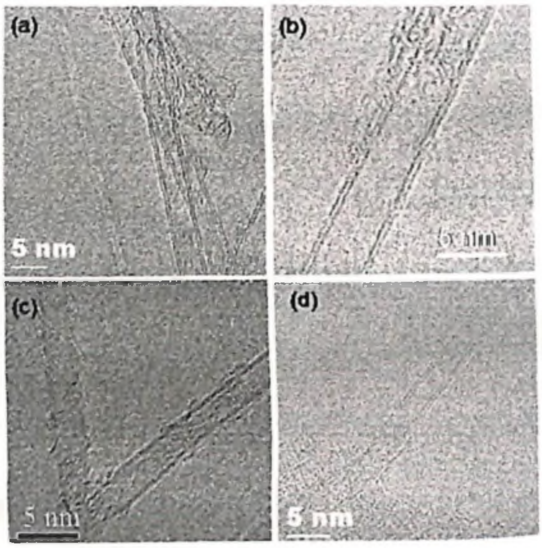

Fig 5.4. HREM images of B-doped DWNTs.

yielded boron-doped DWNTs. The N- and B-doped DWNTs could not be produced at temperatures lower than 950 °C. The combustion method employed for the preparation of the catalyst seems to help in producing DWNTs exclusively with only a very small or negligible proportion of SWNTs.

We have used both transmission electron microscopy (TEM) and Raman spectroscopy to characterize the different DWNTs samples. TEM allows direct imaging of the DWNTs and gives indications for the presence of other species along with the DWNTs. In the TEM images, we seldom encountered SWNTs or MWNTs. Besides providing information on the nature and dimensions of DWNTs, Raman spectroscopy helps to characterize the purity and quality of the DWNTs. Electron energy loss spectroscopy (EELS), carried out in a high-resolution electron microscope, and X-ray photoelectron spectroscopy have been employed to determine the elemental composition of the DWNTs.

Undoped DWNTs obtained by us generally had outer tube diameters of 2.2-2.8 nm and inner tube diameters of 1.4-2.1 nm, as shown by the high-resolution TEM (HREM) images in Figure 5.1. In Figure 5.2 and 5.3, we show typical HREM images of purified nitrogen-doped DWNTs synthesized by using NH_3 and pyridine as the nitrogen source, respectively. In Figure 5.4, we show HREM images of the boron-doped DWNTs. The HREM images indicate that the purified samples of the DWNTs have well-resolved walls and that most of the amorphous carbon was eliminated from the surface during the purification process. HREM images reveal that the outer tube diameters of the N-doped DWNTs prepared by using NH_3 as the nitrogen source are in the 1.7–3.2 nm range and the inner tube diameters are in the 1–2.4 nm range. The interlayer spacing is around 0.38 nm. In the case of N-doped DWNTs prepared by using pyridine as the nitrogen source, the outer tube diameters are generally in the 1.6–2.6 nm range, while the inner tube diameters are in the 0.9–1.8 nm range. The interlayer spacing ranges from 0.34 to 0.41 nm. From the HREM studies, we surmise that the diameters of the N-doped DWNTs obtained by using pyridine are smaller than those obtained with NH_3. Thus, the diameters of the N-doped DWNTs appear to depend on the nitrogen source and the reaction conditions employed.

HRTEM images of the boron-doped DWNTs show that they possess larger diameters than the undoped DWNTs as well as the N-doped DWNTs (Figure 5.4). The outer tube diameters of the B-doped DWNTs range from 2.5 to 4.7 nm, and the inner tube diameters are in the 1.8 –3.9 nm range. The interlayer spacing ranges from 0.35 to 0.41 nm. Figure 5.4b shows the HREM image of a large diameter B-doped DWNT with an outer diameter of 4.7 nm and an inner diameter of 3.9 nm.

It has been reported in the literature that boron and nitrogen are incorporated to SWNTs to a smaller extent than in MWNTs [14–19]. We have estimated the compositions of the N- and B-doped DWNTs prepared by us by employing X-ray photoelectron spectroscopy. A core-level X-ray photoelectron spectrumf the N-doped DWNTs obtained by using NH_3 as the N-source is shown in Figure 5.5a. The C 1s signal is at 284.3 eV, while the N 1s signal is centered at 399.6 eV, indicating of nitrogen substitution in the graphene sheet. It is possible that there is a small amount of amorphous carbon, as suggested by the asymmetry of the C 1s signal, although most of it gets removed on treatment with hydrogen (see Experimental Section). The asymmetric shape of the N 1s peak indicates the existence of at least two components and could be deconvoluted into two peaks at 398 and 401.3 eV. The 398 eV feature is characteristic of pyridinic nitrogen (sp^2 hybridization), while the peak centered at 401.3 eV is due to nitrogen present in graphene sheets [15].

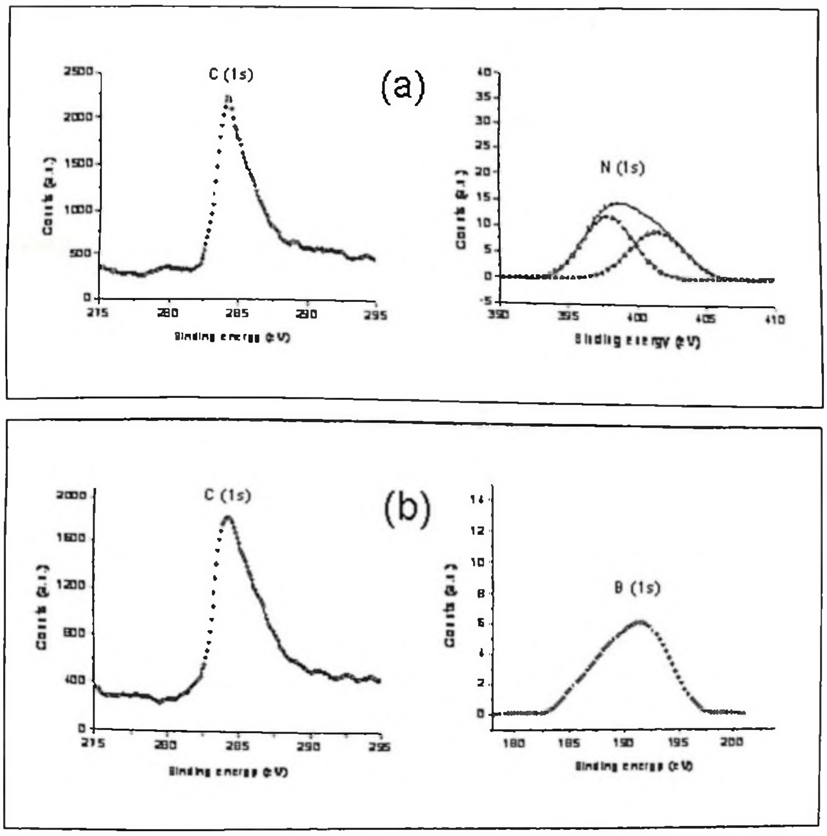

Fig. 5.5. (a) C 1s and N 1s XPS signals of N-doped DWNT prepared using ammonia. (b) C 1s and B 1s signals of B-doped DWNTs.

The areas of the two bands bear a ratio of 1:1. On the basis of the total N 1s and C 1s intensities, the nitrogen-to-carbon ratio in the nanotubes samples was calculated by taking the photoionization cross sections of the 1s levels into account. The average composition was thus found to correspond to 1.3 atom % nitrogen. This value is lower than that reported in the literature for DWNTs (~2.9 atom%) [13] and MWNTs (3–10 atom %) [16]. The N 1s spectrum of N-doped DWNTs obtained by using pyridine as the nitrogen source shows mainly the band at 398 eV, the intensity of the 401.3 eV band being very small. Thus, there is an intrinsic difference in the nature of N-substitution between the N-doped DWNTs prepared by using NH_3 and pyridine.

Figure 5.5b shows the core-level spectra of the B-doped DWNTs. The B 1s feature is at 191.4 eV, and the C 1s signal is at 284.3 eV. The shift of the B 1s signal toward higher binding energy compared to that of pure boron (188 eV) indicates that boron is in the sp^2 carbon network. The slight asymmetry of the B 1s signal would, however, suggest the presence of another possible mode of substitution. The boron content works out to be 1 atom %. Around 3 atom % B-doped MWNTs have been reported [18]. EELS measurements in a high resolution electron microscope confirmed the presence of nitrogen as well as boron in the respective doped DWNTs. The %B and %N were found to be small (~1 atom %), consistent with the XPS data.

The resonance Raman spectrum of DWNTs shows three main features: the G band, the D band, and bands due to the radial breathing modes (RBMs). The tangential stretch G-band modes are in the 1550–

1600 cm^{-1} range. The disorder-induced D-band is observed between 1200 and 1450 cm^{-1}. The D-band is activated in the first-order scattering process by the presence of in-plane substitutional heteroatoms, vacancies, grain boundaries, or other defects and by finite size effects, all of which lower the crystalline symmetry of the quasi infinite lattice [24]. RBM frequencies provide information about the nanotube diameter in the case of SWNTS and DWNTs. We have recorded the Raman spectra of the undoped as well as the N- and B-doped DWNTs by using 632.8 nm excitation using a He-Ne laser. The spectra were collected in a backscattering geometry at room temperature. Figure 5.6a shows the G-bands of the pure as well as doped DWNTs. The G-band of the N-doped DWNTs (Py) appears at a lower frequency (1574 cm^{-1}) compared to that of undoped DWNTs (1575 cm^{-1}), whereas the G-band of the B-doped DWNTs appears at a higher frequency (1579 cm^{-1}). The G-band of the N-doped DWNTs (NH_3) also appears at a lower frequency (1571 cm^{-1}). Thus, the shifts of the G-band are opposite for n- and p-doping of the DWNTs. Such shifts of the G-band have been reported for B- and N-doped SWNTs by Yang *et al.* [25] and McGuire *et al.* [26]. The small-intensity shoulder around 1540 cm^{-1} seen in the spectra of undoped DWNTs shows a decrease in intensity in the N-doped DWNTs and is negligible in the case of B-doped DWNTs. This band is related to the metallic nature of the nanotubes [27] and its near absence in N- and B-doped DWNTs suggests

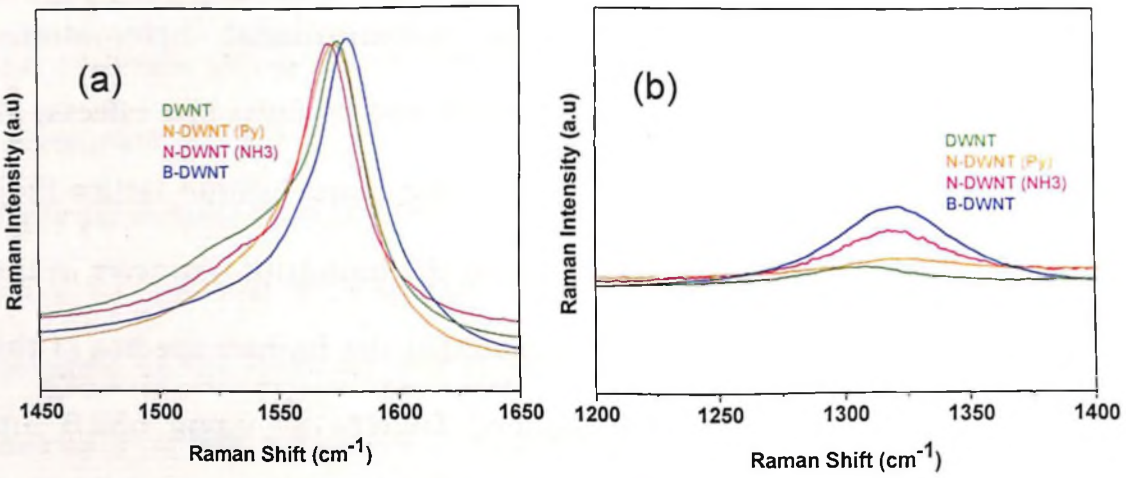

Fig .5.6 The G-bands (a) and D-bands (b) in the Raman spectra of undoped and doped DWNTs

a greater prevalence of semiconducting nanotubes. Figure 5.6b shows that the intensity of the D-band is high in the case of the B-doped DWNTs and low in the case of the N-doped DWNTs. The I(D)/I(G) ratios are 0.04, 0.06, and 0.16 for undoped, N-doped (py), and B-doped DWNTs respectively.

We observe several RBM bands in the DWNTs (Figure 5.7), resulting from various sizes of the nanotubes, just as in earlier reports [28]. By using the relation $\omega=248/d$, where ω is the RBM frequency in cm^{-1} and d is the nanotube diameter in nm, we have obtained the diameters of the DWNTs [28]. The RBM frequencies and the corresponding diameters are tabulated in Table 1 for undoped as well as N- and B-doped DWNTs, along with (n,m) indices for the intense features. From the table, we see that the diameter distribution of the nanotubes is markedly affected by N- and B-doping. The undoped DWNTs show the highest intensity RBM bands centered at 213 and 189 cm^{-1}, corresponding to diameters of 1.16 and 1.31 nm, respectively. The slightly lower intensity or medium-intensity RBM bands are at 158, 143, and 132 cm^{-1}, corresponding respectively to diameters of 1.57, 1.73, and

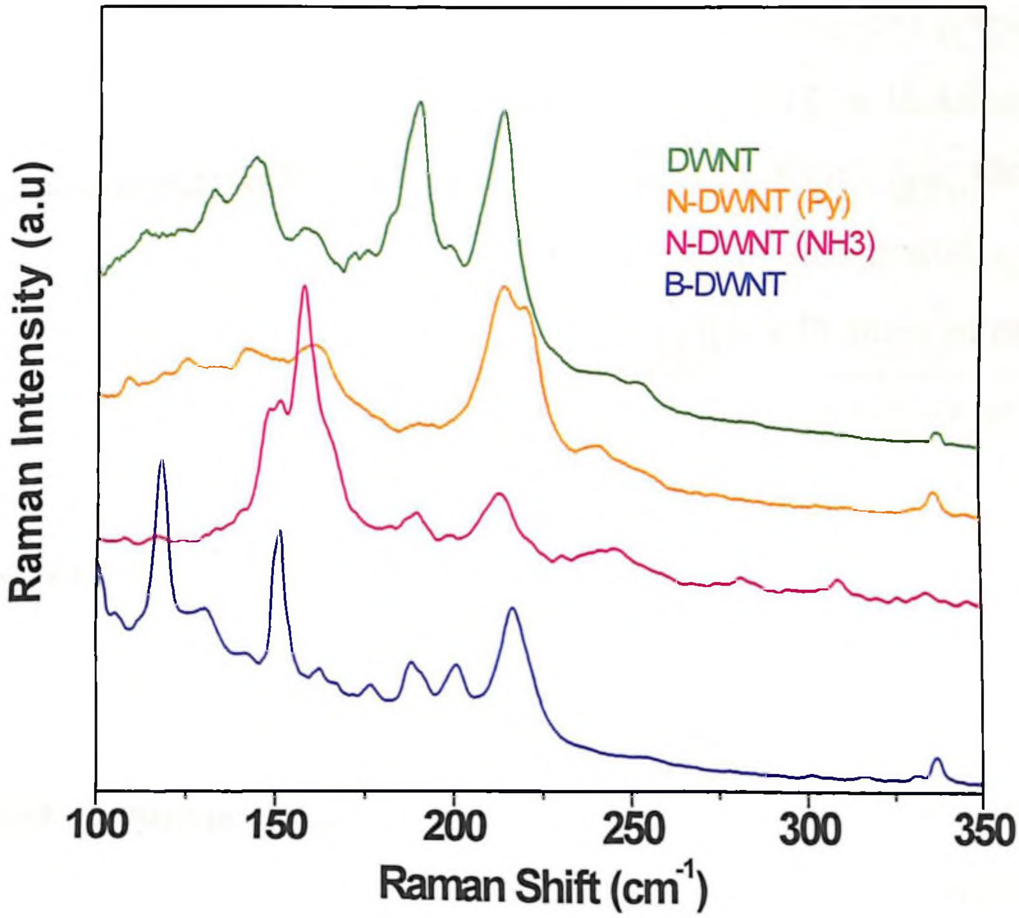

Fig. 5.7 RBM bands of undoped and doped DWNTs

1.88 nm. The N-doped DWNTs (Py) show the highest intensity RBM bands centered at 220 and 214 cm^{-1}, corresponding to diameters of 1.13 and 1.16 nm, respectively. The slightly lower intensity bands centered at

160 and 142 cm^{-1} correspond to 1.55 and 1.75 nm diameters, respectively. The diameters of the N-doped DWNTs (Py) are somewhat smaller compared to those of the undoped DWNTs. This is, however, not the case with N-doped DWNTs prepared using NH_3 as the nitrogen source. The DWNTs (NH_3) show the highest intensity RBM band at 158 cm^{-1}, corresponding to a diameter of 1.57 nm. The slightly lower intensity bands centered at 213, 152, and 147 cm^{-1} correspond to diameters of 1.16, 1.63, and 1.69 nm, respectively. Since the nature of N-substitution as well as the nature of the defects is different in the N-doped DWNTs prepared by using NH_3 and pyridine.

The B-doped DWNTs exhibit a high proportion of large-diameter DWNTs compared to the undoped or N-doped DWNTs. The most intense RBM bands of the B-doped DWNTs are at 217, 151, and 118 cm^{-1}, corresponding to diameters of 1.14, 1.64, and 2.1 nm, respectively. The slightly lower intensity bands centered at 201, 189, and 130 cm^{-1} correspond to diameters of 1.23, 1.31, and 1.91 nm, respectively. Due to a cutoff filter, the peaks below 100 cm^{-1} were not detected.

The diameters of the various DWNTs calculated from the RBM modes are comparable with those obtained from the TEM images, but the larger diameter nanotubes seen in the TEM images are not registered in the Raman spectra since the RBM modes below 100 cm^{-1} could not be recorded by us. We can identify DWNT pairs by taking the difference between the inner and outer diameters to be around 0.7 nm. The frequencies (cm^{-1}) of such pairs of the RBM bands in the case of undoped DWNTs are (252,143), (213,132), and (189,113).

Table-1

RBM frequencies of undoped and N- and B-doped doped DWNTs

DWNTs $^{(a)}$	N-DWNTs (Py) $^{(b)}$	N-DWNTs (NH_3) $^{(c)}$	B-DWNTs $^{(d)}$
RBM, cm^{-1} (dia, nm)	RBM, cm^{-1} (dia, nm)	RBM, cm^{-1} (dia, nm)	RBM, cm^{-1} (dia, nm)
338(0.73)	337(0.74)	334(0.73)	336(0.74)
252(0.98)	241(1.03)	308(0.81)	*217(1.14)
*213(1.16)	*220(1.13)	281(0.88)	**201(1.23)
199(1.25)	*214(1.16)	247(1.0)	**189(1.31)
*189(1.31)	191(1.30)	**213(1.16)	177(1.40)
175(1.42)	**160(1.55)	199(1.25)	163(1.52)
171(1.45)	**142(1.75)	191(1.30)	*151(1.64)
**158(1.57)	134 (1.85)	*158(1.57)	**130(1.91)
**143(1.73)	125(1.98)	**152(1.63)	*118(2.10)
**132(1.88)	118(2.10)	**147(1.69)	105(2.36)
113(2.20)	108(2.30)	134 (1.85)	
		107(2.32)	

* highest intensity ** medium intensity

The possible (n, m) values for the intense bands are as follows

(a) 213 [(7, 10)], 189 [(3, 15); (6, 13)], 158 [(14, 9); (19, 2)], 143 [(17 ,8)], 132 [(18, 9); (21, 5)]

(b) 220 [(4, 12)], 214 [(7, 10)], 160 [(18, 3); (6, 16)], 142 [(20, 4); (7, 18)].

(c) 213 [(7, 10)], 158 [(7, 10)], 152 [(13, 11); (12, 12)], 147 [(21, 1); (6, 18)].

(d) 217 [(1, 14)], 201 [(3, 14); (7, 11)], 189 [(3, 15)], 151 [(18, 5); (15, 9)], 130 [(16, 12)], 118 [(5, 24); (15, 16)].

The metallic (m) and semiconducting (s) natures of these pairs are respectively (s,m), (m,m) or (m,s), and (m,s) or (s,s). In the N-doped

DWNTs (py), the pairs are (241,142), (214,125), (220,134), and (160,108), and they are (s,s), (m,s), (s,s), and (m,m) or (m,s), respectively.

For N-doped DWNTs (NH_3), the pairs are (281,158), (247,147), (213,134), and (152,107), and these pairs are respectively (s,s), (s,s) or (s,m), (m,s), and (m,m) or (m,s) or (s,m) or (s,s). In the B-doped DWNTs, the pairs are (217,130), (177,118), (189,118), and (151,105), and these pairs are (s,s), (m,s) or (s,s), (m,s), and (m,m) or (m,s) or (s,m) or (s,s), respectively. Taking the semiconducting and metallic nature of all the RBM bands, the ratio of semiconductor to metallic nanotubes in the case of undoped DWNTs works out to be 2:1, while it is 2:1, 2.2:1, and 2:1, respectively, in the case of N-doped DWNTs (py), N-doped DWNTs (NH_3), and B-doped DWNTs. Thus, the RBM modes predict a greater proportion of semiconducting nanotubes in the doped DWNTs as well.

The electronic absorption spectra of undoped as well as doped DWNTs (Figure 5.8) show bands in the 900–1200 nm region due overlapping $E_{22}{}^{s}$ (s = semiconductor) features of the outer tubes and $E_{11}{}^{s}$ of inner tubes [29]. The absorption bands in the 1600–2400 nm regions are due to $E_{11}{}^{s}$ of the outer tubes. The absorption bands due to $E_{11}{}^{m}$ (m = metal) of the outer tubes are found in the 400–600 nm region. The metallic feature seems to be prominent in the undoped DWNTs. Accordingly, the 1540 cm^{-1} G^{+}-band in the Raman spectrum is less prominent in the doped nanotubes.

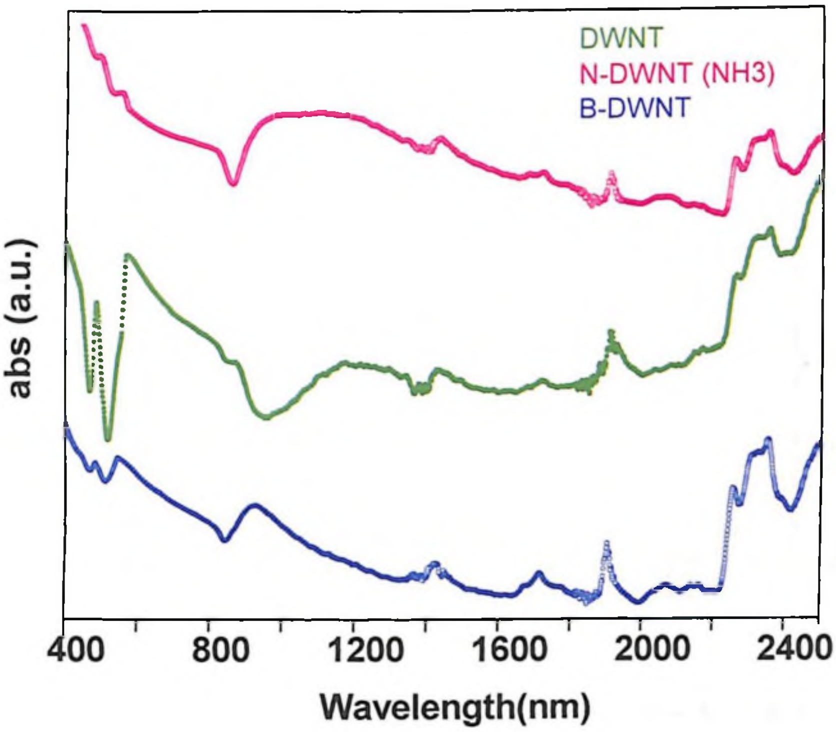

Fig. 5.8 Electronic absorption spectra of undoped and doped DWNTs

The smaller diameter carbon nanotubes are known to be less stable than their larger diameter counterparts and tend to oxidize at lower temperatures. Amorphous carbon and carbon nanotubes with defects undergo combustion at lower temperatures. In Figure 5.9, we show the thermogravimetric analysis (TGA) curves of undoped as well as N- and B-doped DWNTs. The decomposition temperatures of all these doped DWNTs are comparable to but slightly lower that the decomposition temperature of pure DWNTs. Derivative TGA curves also shows the same trend. The slight increase in mass at high temperature may be due to the small metallic impurity.

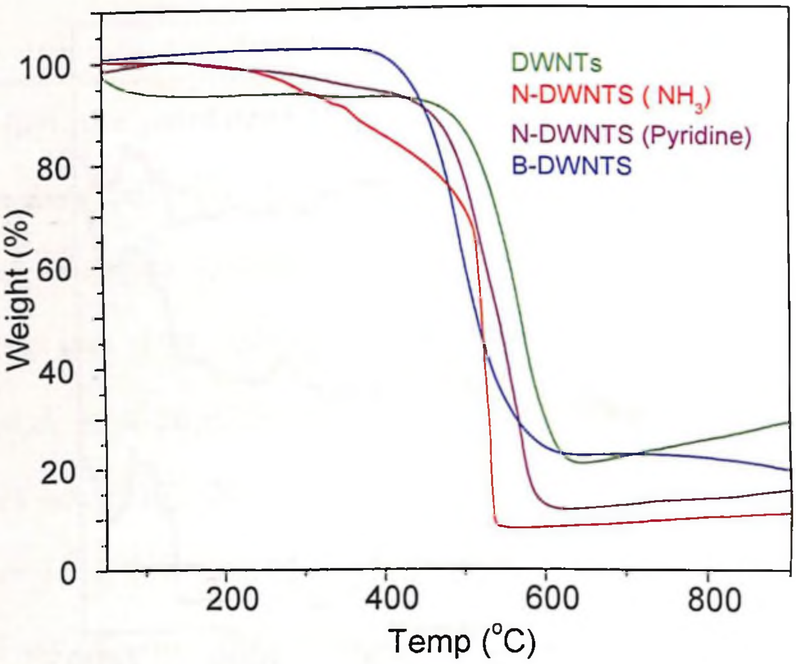

Fig. 5.9 TGA curves of undoped and doped DWNTs

3.5 Conclusions

In conclusion, the $Mo_{0.1}Fe_{0.9}Mg_{13}O$ catalyst prepared by the combustion route preferentially yields DWNTs, the proportion of SWNTs being very small or negligible. The use of this catalyst has enabled the synthesis of 1 atom % N- and B-doped DWNTs. The diameters of the nanotubes obtained from the Raman RBM modes and transmission electron microscopy are comparable. The N-doped nanotubes show the G-band in the Raman spectrum at a lower frequency than the undoped ones, while the B-doped nanotubes show an increase in the frequency. The proportion of the metallic nanotubes appears to decrease on N- or B-doping, but the average diameter is substantially larger in the B-doped DWNTs.

References

1. H . Dai, A. Rinzler, P. Nikolaev, A. Thess, D. Colbert and R. Smalley, *Chem. Phys. Lett.* **1996**, *260*, 471.
2. C. N. R. Rao and A. Govindaraj, “Nanotubes and Nanowires”, The *RSC Nanoscience & Nanotechnology series*, Eds.; Sir Harry Kroto, Paul O’Brien, Harold Craighead, **2005**.
3. H. Kurachi, S. Uemura, J. Yotani, T. Nagasako, H. Yamada, T. Ezaki, T. Maesoba, R. Loutfy, A. Moravsky, T. Nakazawa, Y. Saito, Proc. 21st IDRC in conjunction with 8th IDW, **2001**, 1237
4. R. Saito, R. Matsuo, T. Kimura, G. Dresselhaus and M. S. Dresselhaus, *Chem.Phys. Lett.* **2001**, *348*, 187.
5. T. Sugai, H. Yoshida, T. Shimada, T. Okazaki, and H. Shinohara, *Nano Lett.* **2003**, *3*, 769.
6. Y. D. Lee, H. J. Lee, J. H. Han, J. E. Yoo, Yun-Hi Lee, J. K. Kim, S. Nahm, and B-K Ju, *J. Phys. Chem. B* **2006**, *110*, 5310.
7. B. C. Liu, S. C. Lyu, T. J. Lee, S. K. Choi, S. J. Eum, C. W. Yang, C. Y. Park, C. J. Lee, *Chem. Phys. Lett.* **2003**, *373*, 475.
8. S. C. Lyu, T. J. Lee, C. W. Yang and C. J. Lee, J. *Chem. Comm.* **2003**, 1404.
9. S. C. Lyu, B. C. Liu, S. H. Lee, C. Y. Park, H. K. Kang, C-W Yang, and C. J. Lee, *J. Phys. Chem.B* **2004**, *108*, 2192.
10. S. C. Lyu, B. C. Liu, C. J. Lee, H. K. Kang C-W Yang and C. Y. Park, *Chem. Mater.* **2003**, *15*, 3951.

11. J. Wei, L. Ci, B. Jiang, Y. Li, X. Zhang, H. Zhu, C. Xua and D. Wua, *J. Mater. Chem.* **2003**, *13*, 1340.

12. W. Ren and H-M Cheng, *J. Phys. Chem. B* **2005**, *109*, 7169.

13. A. Hassanien, M. Tokumoto, Y. Kumazawa, H. Kataura, Y. Maniwa, S. Suzuki, and Y. Achida, Y. *Appl. Phys. Lett.* **1998**, *73*, 3839.

14. R. Sen, B. C. Satishkumar, A. Govindaraj, K. R. Harikumar, M. K. Renganathan, C. N. R. Rao, *J. Mater. Chem.* **1997**, *7*, 2335.

15. R. Sen, B. C. Satishkumar, A. Govindaraj, K. R. Harikumar, G. Raina, J. -P. Zhang, A. K. Cheetham and C. N. R. Rao, *Chem. Phys. Lett.* **1998**, *287*, 671.

16. M. Nath, B. C. Satishkumar, A. Govindaraj, C. P. Vinod and C. N. R. Rao, *Chem. Phys. Lett.* **2000**, *322*, 333.

17. F. Villalpando-Paez, A. Zamudio, A.L. Elias, H. Son, E.B. Barros, S.G. Chou, Y.A. Kim, H. Muramatsu, T. Hayashi, J. Kong, H. Terrones, G. Dresselhaus, M. Endo, M. Terrones, M.S. Dresselhaus, *Chem. Phys. Lett.* **2006**, *424*, 345.

18. B. C. Satishkumar, A. Govindaraj, K. R. Harikumar, J. -P Zhang, A. K. Cheetham and C. N. R. Rao, *Chem. Phys. Lett.* **1999**, *300*, 473.

19. K. McGuire, N. Gothard, P. L. Gai, M. S. Dresselhaus, G. Sumanasekera, A. M. Rao, *Carbon* **2005**, *43*, 219.

20. J.-C. Charlier, M. Terrones, M. Baxendale, V. Meunier, T. Zacharia, N. L. Rupesinghe, W. K. Hsu, N. Grobert, H. Terrones, and G. A. J. Amaratunga, *Nano Lett.* **2002**, *2*, 1191.

21. R.B. Sharma, D.J. Late, D.S. Joag, A. Govindaraj and C.N.R. Rao, C.N.R. *Chem. Phys. Lett.* **2006**, *428*, 102.

22. R. Czerw, M. Terrones, J.-C. Charlier, X. Blase, B. Foley, R. Kamalakaran, N. Grobert, H. Terrones, D. Tekleab, P. M. Ajayan, W. Blau, M. Rühle, and D. L. Carroll, *Nano Lett.* **2001**, *1*, 457.

23. S. Y. Kim, J. Lee, C. W. Na, J. Park, K. Seo, B. Kim, *Chem. Phys. Lett.* **2005**, *413*, 300.

24. M. S. Dresselhaus and P. C. Eklund, *Advances in Physics* **2000**, *49*, 705.

25. Q. H. Yang, P. X. Hou, M. Unno, S. Yamauchi, R. Saito and T. Kyotani, *Nano Lett.* **2005**, *5*, 2465.

26. K. McGuire, N. Gothard, P. L. Gai, M. S. Dresselhaus, G. Sumanasekera, A. M. Rao, *Carbon* **2005**, *43*, 219.

27. A. Das, A. K. Sood, A. Govindaraj, A. M. Saitta, M. Lazzeri, F. Mauri, C. N. R. Rao, *Phys. Rev. Lett.* **2007,** *99*, 136803.

28. F. Li, S. G. Chou, W. Ren, J. A. Gardecki, A. K. Swan, M. S. Unlu, B. B. Goldbeg, H-M. Cheng, M. S. Dresselhaus, M. S. *J. Mater. Res.* **2003**, *18*, 1251.

29. N. Kishi, S. Kikuchi, P. Ramesh, T. Sugai, Y. Watanabe, and H. Shinohara, *J. Phys. Chem. B* **2006**, *110*, 24816.

30. K. C. Patil, *Bull. Mater. Sci.* **1993**, *16*, 533.

31. E. Flahaut, A. Peigney, W. S. Bacsa, R. R. Bacsa and C. Laurent, *J. Mater. Chem.* **2004**, *14*, 646.

32. S. R. C. Vivekchand, A. Govindaraj, Md. Motin Seikh, C. N. R. Rao, *J. Phys. Chem. B* **2004**, *108*, 6935.